Microstructure Evolution and Hydrogen Embrittlement Behaviors in High-Strength TRIP-Aided Bainitic Ferrite Steel

博 士 学 位 論 文

Doctoral Thesis

論文題目

Thesis Title

Microstructure Evolution and Hydrogen Embrittlement Behaviors in High-Strength TRIP-Aided Bainitic Ferrite Steel

東北大学大学院工学研究科

Graduate School of Engineering,

TOHOKU UNIVERSITY

専攻/Department： Quantum Science and Energy Engineering

学籍番号/ ID No： C0TD1804

氏名/Name： ZHOU YUTAO

TOHOKU UNIVERSITY
Graduate School of Engineering

Microstructure Evolution and Hydrogen Embrittlement Behaviors in High-Strength TRIP-Aided Bainitic Ferrite Steel
（高強度TRIP型ベイニティックフェライト鋼の微細組織形成と水素脆化挙動）

A dissertation submitted for the degree of Doctor of Philosophy (Engineering)

Department of Quantum Science and Energy Engineering

by

Yutao ZHOU

January 6, 2023

Microstructure Evolution and Hydrogen Embrittlement Behaviors in High-Strength TRIP-Aided Bainitic Ferrite Steel

Yutao Zhou

Abstract

Striving for developing alloys with high strength and sufficient uniform ductility has been an imperative challenge in structural applications. The concept of a carbide-free bainite matrix has been developed for low-carbon low-alloy transformation-induced plasticity (TRIP)-aided steels to obtain better mechanical properties than those of the first generation of advance high strength steels (AHSSs) and potentially lower costs than that of the twinning-induced plasticity steels. Specifically, the TRIP-aided steel can show ultimate tensile strength (UTS) of over 1 GPa and total elongation (TEl) of about 25%. However, one of the challenges is hydrogen embrittlement (HE) susceptibility that increases with increasing strength. Therefore, microstructure design approaches need to be identified for decreasing the crack initiation probability and enhancing HE resistance. The objective of this thesis focuses on the microstructure evolution and HE behaviors in TRIP-aided bainitic ferrite (TBF) steel.

In this study, the effects of austempering time on the microstructure, mechanical properties, and fracture mechanisms of Fe-0.4C-1.5Si-1.5Mn TBF steel were investigated using tensile tests and microstructure examination. When the austempering time increased until 3600 s, the volume fraction of retained austenite and its carbon concentration initially increased and then decreased. The increase in carbon concentration during austempering may be attributed to the formation of fine bainitic ferrite, representing the matrix and in turn the formation of retained austenite with a film-type morphology. When the austempering time was increased from 0 to 1000 s, the TBF steel showed excellent mechanical properties such as high yield strength (YS) and UTS, and uniform elongation and TEl. Meanwhile, void density increased significantly in the initial stages and then slightly decreased. In contrast, the trend observed for mean crack length was opposite to that of void density leading to the change in the fracture mode of the TBF steels from intergranular to quasi-cleavage and ductile fractures. It could be inferred that the improvement in mechanical properties, especially the good ductility, at the optimal austempering time result from the suppression of crack propagation and occurrence of crack blunting owing to the effective deformation-induced transformation of retained austenite.

Secondly, TBF steels performed at austempering temperature at 400 ℃ for 1000 s were investigated at the deformation temperature range of -100 to 100 ℃ in the presence of hydrogen. In the hydrogen-uncharged condition, the martensitic transformation was accelerated with a decrease in the deformation temperature, resulting in a decrease in the YS and an increase in the UTS owing to an increase in the work-hardening rates. The UEl at 21 ℃ was the maximum and decreased with a decrease in the deformation temperature. The decrease in the UEl at low deformation temperature was attributed to the increase in work hardening rates, which accelerated reaching the critical stress for brittle cracking. This implies the occurrence of brittle premature fracture before necking. The UEl decreased, and the brittle-like quasi-cleavage fracture occurred in the hydrogen-charged specimens deformed at low temperatures. The transformation ratios were high at the low deformation temperature in the hydrogen-charged and hydrogen-uncharged specimens. These might be caused by the formation of transformed martensite that comprised supersaturated hydrogen and hydrogen-assisted failure without macroscopic plasticity localization, *i.e.*, necking. The significant decrease in the UEl of the hydrogen-charged specimen tensile-tested at 100 ℃ was not significant whereas the UEl decreased at 21 ℃ although mixed quasi-cleavage/ductile fracture features were observed and serrated flow was exhibited in the stress-strain curves at both 21 and 100 ℃, which indicated dynamic strain aging. The decrease in the UEl tensile tested at 21 ℃, might have been caused by the Portevin-Le Chatelier (PLC) banding-related localized plasticity, which results in significant necking and associated stress triaxiality evolution. The excellent hydrogen embrittlement resistance of the hydrogen-charged specimen deformed at 100 ℃ might be attributed to the suppression of deformation-induced martensitic transformation, which reduces the number density of the hydrogen-related crack initiation site and decreases flow stress.

In addition, we evaluated the quantitative hydrogen and deformation temperature effects on associated micro-damage evolution in TBF steels. The average crack length of hydrogen-uncharged specimens slightly increased with the local strain, and a decrease in deformation temperature from 100 to -100 °C increased the average crack length due to the increase in flow stress and deterioration of bainitic ferrite arrestability, which is accompanied by a change in the fracture mode from ductile fractures to the mixture of brittle-like and ductile features and quasi-cleavage failure. Hydrogen charging increased the probability of micro-damage initiation and deteriorated micro-damage arrestability, which decreased elongation. Meanwhile, the introduction of hydrogen increased the number density of micro-damage and deteriorated the resistance to the hydrogen-induced cracks initiation and deteriorated micro-damage arrestability, which decreased elongation. The probability of micro-damage initiations was sensitive to deformation temperature, which was closely related to the promotion of deformation-induced martensitic transformation.

Contents

Chapter 1: Introduction

1 Introduction

1.1 Background

Growing demands for achieving excellent mechanical properties, environmental sustainability and low production costs for structural applications are the driving force for the development of new materials [1–4]. Therefore, materials scientists and engineers invest a lot of efforts in designing and developing next generation steel grades with optimum mechanical properties for existing and novel technological challenges [5–8]. In particular, advanced high-strength steels (AHSSs) with a combination of high strength and ductility have extensively drawn attention as high performance structural parts for automotive, energy fields and other applications [9–11]. Note that AHSSs is generally considered to have tensile strength of over 700 MPa [12]. For example, AHSSs has been extensively used in the automotive industry to reduce the weight of body-in-white and fuel economy as well as to improve vehicle safety, as shown in Figure. 1-1 [13–15]. In addition, some structural components in pressurized water reactor use AHSSs instead of carbon steel for reliability and safety (Figure. 1-2) [16]. Therefore, it is important to understand the microstructure and associated mechanical behavior of AHSSs in a specific service environment.

AHSSs have been divided into three main categories, and their general strength-ductility balance is shown in Figure. 1-3 [12]. Dual-phase (DP) and conventional transformation-induced plasticity (TRIP) steels, generally regarded as first-generation AHSSs, offer a widespread property range [17–20]. Although these steels can meet the needs of steel grades of different strength levels, the first-generation AHSSs is characterized by a sharp decrease in ductility as the strength increases. Meanwhile, the low product of strength and elongation cannot meet the development requirements for strength and ductility. In this context, twinning-induced plasticity (TWIP) steel with high manganese (>12%) as second-generation AHSSs have been developed within the last decades, which is characterized by an excellent combination of strength and ductility compared with first-generation AHSSs [21–24]. TWIP steel exhibited high strength of about 1 GPa with elongations of about 50% [25–27]. However, there is a serious challenge in terms of mass production of TWIP steel. Namely, adding a large amount of alloying element such as Mn not only significantly increased the production cost, but also increased the difficulty of the production process including continuous casting and rolling [28, 29]. For this reason, the Mn content in these types of steel needs to be reduced. Then, third-generation AHSSs such as medium Mn steel (MMS) (3~12% Mn) and quenching

and partitioning (Q&P) steel were designed to address the limitations between the first and second generation AHSSs and the gap between mechanical property of the two previous ones [30–36]. Meanwhile, as a new family of third-generation AHSSs, Sugimoto *et al*. [37] proposed a use of low-carbon low-alloy (0.1~0.4% C, <2%Mn) TRIP-aided steels mainly consisting of a bainitic ferrite lath matrix with a high dislocation density and retained austenite, which are referred to as TRIP-aided bainitic ferrite (TBF) steels (Figure. 1-4). The TBF steels show tensile strengths of over 1 GPa and elongation greater than 20% [37, 38]. Moreover, good cost performance of TBF steels is another advantage, which is achieved by using compositionally lean alloys and simplification of thermomechanical treatments. TBF steels simultaneously satisfies governmental regulations, economic constraints, and consumer requirement (Figure. 1-5).

In addition, although these strategies have achieved relatively ideal strength-ductility trade-off, one of the problems in all these steels is that high strength is accompanied by hydrogen embrittlement (HE) [39–42]. Furthermore, each microstructural component in multiphase TRIP-aided steels exhibited variable hydrogen trapping ability and different diffusivity and solubility of hydrogen, making it difficult to evaluate the hydrogen-related behavior of TRIP-aided steels [43, 44]. In addition, TRIP-aided steels used as automobile structural parts were inevitably exposed to different temperatures and hydrogen environments during production and service [45, 46]. Hence, fundamental studies on HE are essential to understand mechanical properties and improve the resistance of HE of TRIP-aided steels.

Based on the above background, the purposes of this work are to investigate different processes route on the newly designed TBF steel, and to systematically study the transformation of retained austenite and their role on fracture behavior. Moreover, this work also aims to research on HE sensitivity systematically for theoretical guidance and reference for the development and application of a new generation of TBF steels.

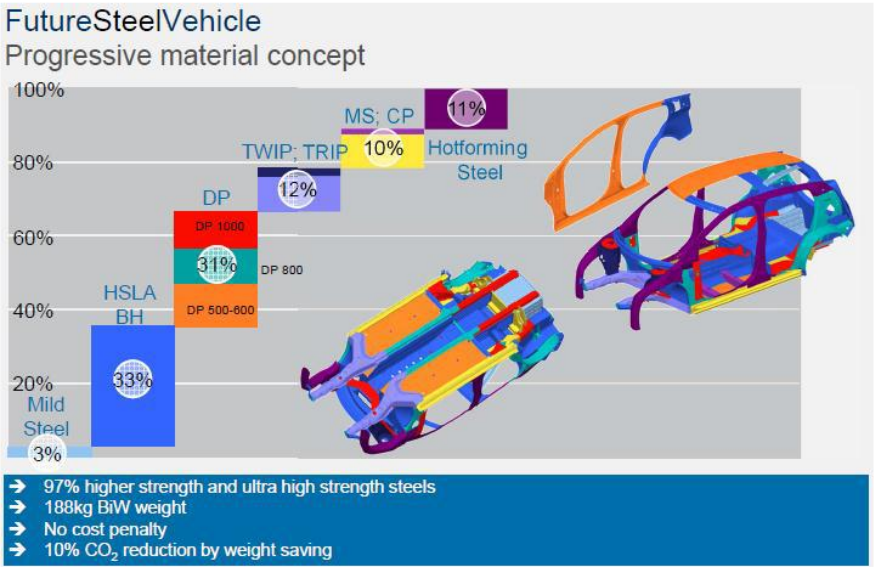

Figure. 1-1 Light vehicle metallic material trends Europe [13].

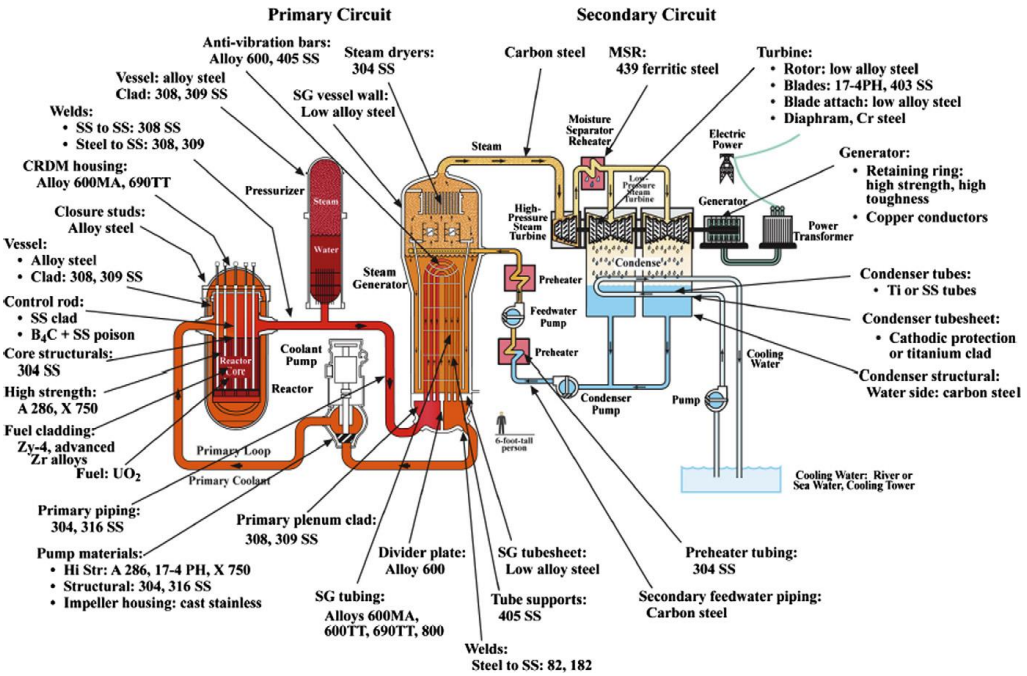

Figure. 1-2 Schematic of the primary and secondary circuits of a pressurized water reactor and materials of construction [16].

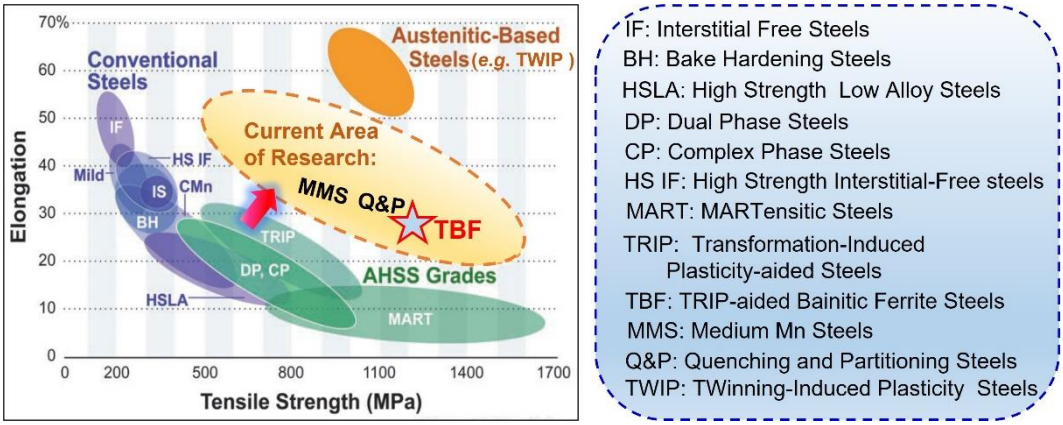

Figure. 1-3 Tensile strength versus total elongation of various AHSSs grades [12].

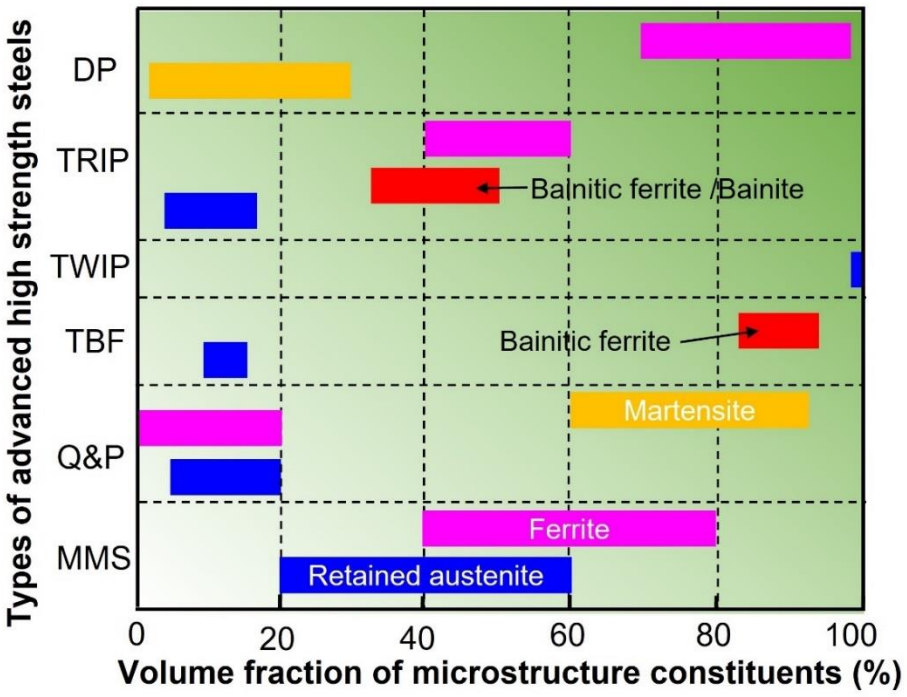

Figure. 1-4 Volume fraction of microstructure constituents of various AHSSs grades.

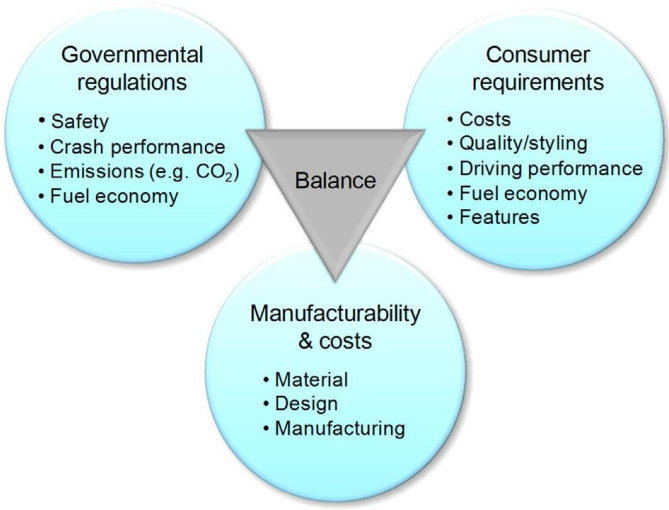

Figure. 1-5 Drivers and constraints for the car manufacturers [17].

1.2 Transformation-induced plasticity-aided steel

The group of TRIP-aided steels is named after the inherent dominant TRansformation Induced Plasticity effect in those steels. Zackay *et al*. [47] firstly reported that the austenite in Fe-0.3C-9Cr-8Ni-2Mn-2Si-4Mo steel transformed into martensite and TRIP effect was found. Since then, TRIP-aided steels have aroused great interest in industry and academia and have been developed rapidly [48–51]. TRIP-aided steels are usually produced via a thermomechanical process of intercritical annealing followed by rapid cooling to a bainitic transformation regime, and then cooled to room temperature [52–54]. Generally, the microstructure of conventional TRIP-aided steel consisted of ferrite, bainite /bainitic ferrite and some retained austenite showing TRIP effect [55, 56]. The TRIP effect refers to the phenomenon whereby soft retained austenite transforms into hard martensite via external stress [57]. This transformation substantially raises the work-hardening rate and delays the necking, resulting in the tensile strength from 600 to 780 MPa and an elongation of 15% – 35% [58]. Therefore, TRIP-aided steels are widely used in automobile bumpers or B-pillar reinforcement (Figure. 1-6) [59, 60]. To reduce the thickness of safety-related components of novel vehicle platforms even further, TRIP-aided steels with a strength of over 780 MPa are henceforth of prime importance.

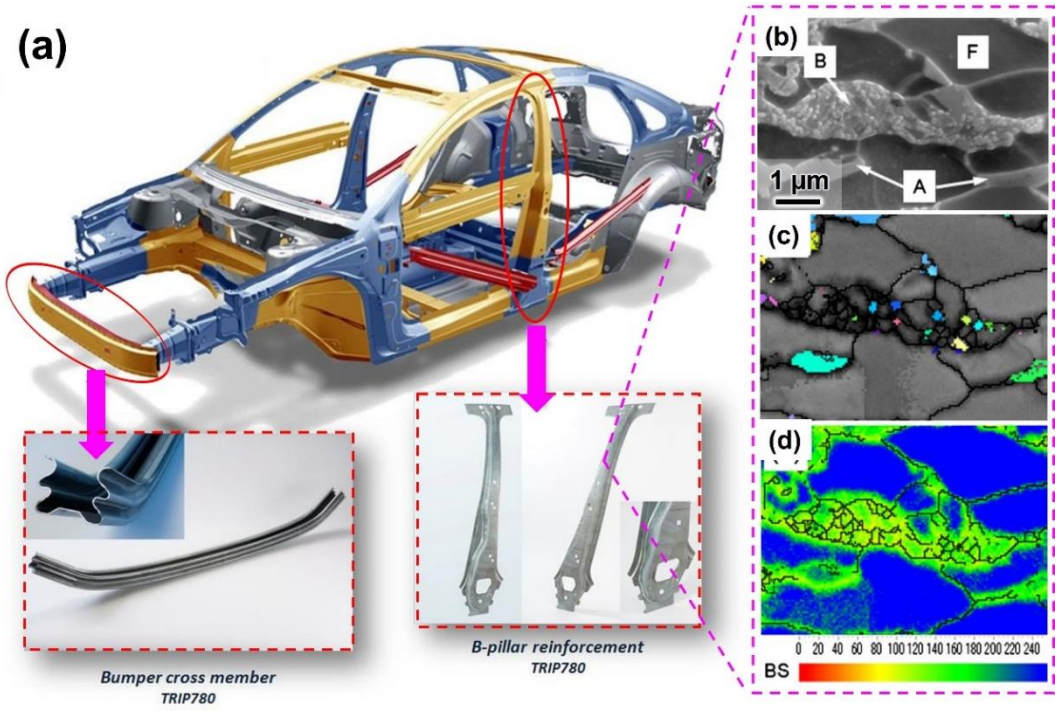

Figure. 1-6 (a) TRIP-aided steels in automotive industry, (b) scanning electron microscopy (SEM) image, (c) inverse pole figure (IPF) map, and (d) band slope (BS) map of the microstructure. B, F, and A represent bainite, ferrite, and retained austenite, respectively [59, 60].

1.2.1 Alloying strategy

Alloy design plays a significant role in the development of TRIP-aided steels, which affected the process routes and resulted in the formation of different types of microstructures at room temperature, and then significantly affects the final properties. A schematic composition diagram summarizing the main reasons for the alloying concept is shown in Figure. 1-7 [61, 62]. In recent years, the selection of lean alloying addition and the determination of the minimum concentration are used to produce multiphase microstructures in TRIP-aided steel [61].

C is an important element in TRIP-aided steels, which affects phase transformations and the final microstructure [63, 64]. C also strongly stabilizes austenite which suppresses the formation of thermal and mechanical martensite [65, 66]. Moreover, it is well known that C has a strong solid solution hardening [67]. However, excessive carbon content deteriorates the weldability of the steel sheet [62]. Therefore, it is crucial to control the carbon content of TRIP-aided steels within the proper range.

Mn is the most featured element in TRIP-aided steels. The most important role of Mn is to stabilize austenite and retain it at ambient temperature [68, 69]. Adding 1% Mn in austenite would result in around 30~40 ℃ decrease for the martensite transformation

start temperature (M_s) [70]. However, high Mn contents (~2.5%) are not favorable as they lead to banding in the microstructure and excessively stabilized retained austenite in conventional TRIP-aided steels [71].

Si inhibits the formation of cementite during austempering treatment, which is attributed to the fact that Si solubility in carbides is very low, thus Si significantly reduces the driving force for precipitation [72, 73]. However, Si also deteriorates the galvanizability of TRIP-aided steels owing to the formation of a stable oxide film adherent to the steel substrate, resulting in poor coatability [74, 75].

Al has a similar effect compared with Si in terms of enlarging the two-phase region range, and suppressing the formation of cementite [76, 77]. Moreover, substituting Si by Al can improve the galvanizability without significantly sacrificing mechanical properties in TRIP-aided steels [62].

In addition, micro-alloying elements such as Nb, Ti, and V were added, which can refine microstructure, form carbide or carbo-nitride precipitates, and achieve a strength level of over 1 GPa [78–82]. Meanwhile, Cr and Ni were found effective in stabilizing the austenite, leading to the improvement in both strength and ductility [83, 84]. However, the formation of carbide or carbo-nitride precipitates consumed some carbon atoms and decreased the carbon concentration partitioned into austenite, resulting in reducing the stability of retained austenite. On the other hand, the addition of micro-alloying elements increased production costs.

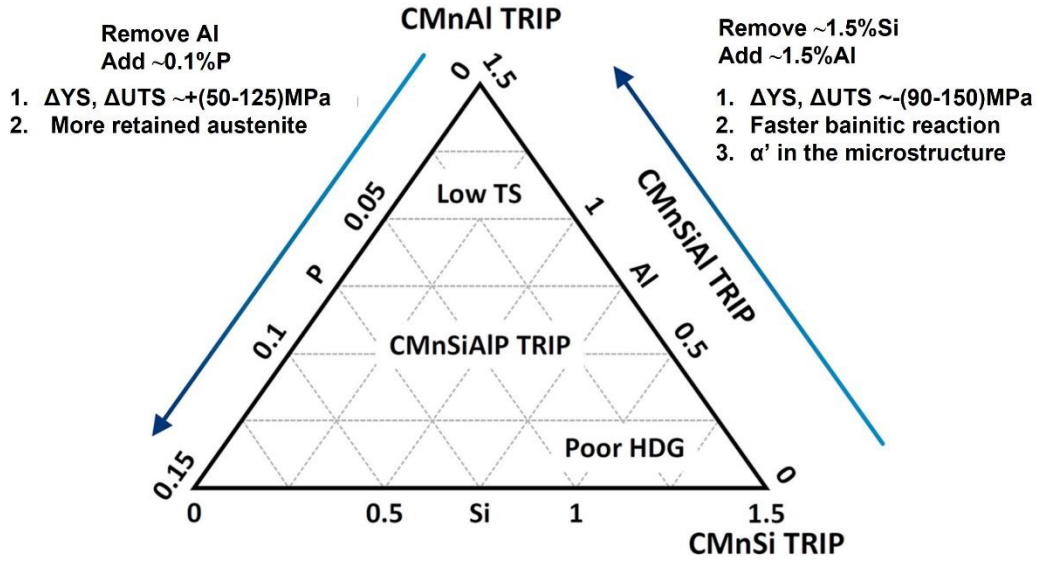

Figure. 1-7 Schematic of chemical composition diagram for low alloy TRIP-aided steels [61, 62].

1.2.2 Heat treatment processing

In addition to the design of alloy composition, the process parameters are also controlled the mechanical properties of TRIP-aided steels. The control of the TRIP-aided steels production process is mainly carried out to obtain the retained austenite and different microstructure constituents [85, 86]. The heat treatment conventionally used for TRIP-aided steels consists of intercritical annealing followed by an isothermal bainitic transformation, and a process often referred to as austempering treatment, as shown in Figure. 1-8 [14, 87, 88]. According to different production processes, TRIP-aided steel can be divided into hot-rolled TRIP-aided steel and cold-rolled TRIP-aided steel. The cast slab is hot-rolled in the austenite, followed by heat preservation in the two-phase region of austenite and ferrite, and finally coiled in the bainite phase transformation regime to obtain hot-rolled steel, while the cold-rolled TRIP-aided steels are obtained by intercritical annealing of the cold-rolled sheet in the two-phase region, followed by isothermal holding in the bainite region for a period of time, as shown schematically in Figure. 1-8(b) [14]. Some investigations suggested that the austempering temperature is range from 360 to 450 ℃ [89, 90]. In addition, there is an increasing focus on the variant of the austempering treatment and novel heat treatment approach to obtain the desired mechanical properties and to produce the variant of TRIP-aided steels [91–93]. For instance, Huang *et al*. [91] reported that the combination of cyclic pre-quenching and two-stage heat treatment significantly enhanced mechanical properties and refined the microstructure in a low-alloyed TRIP-aided steel, which notably enhances their ductility. Therefore, understanding the processing methods and properties of these steels is of utmost importance in the context of TRIP effect.

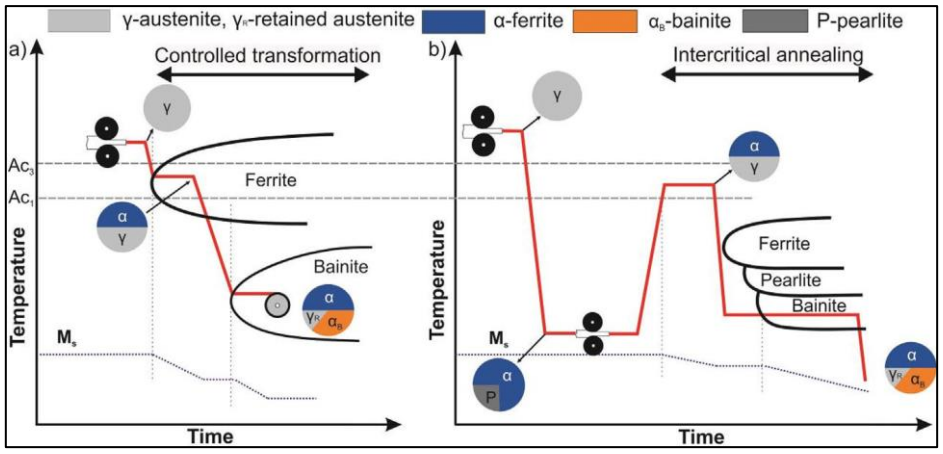

Figure. 1-8 Processing routines to produce (a) the hot rolled TRIP-aided steel strips with controlled cooling after hot rolling and coiling in the bainitic transformation region and (b) the cold rolled TRIP-aided steel strips with intercritical annealing after cold rolling [14].

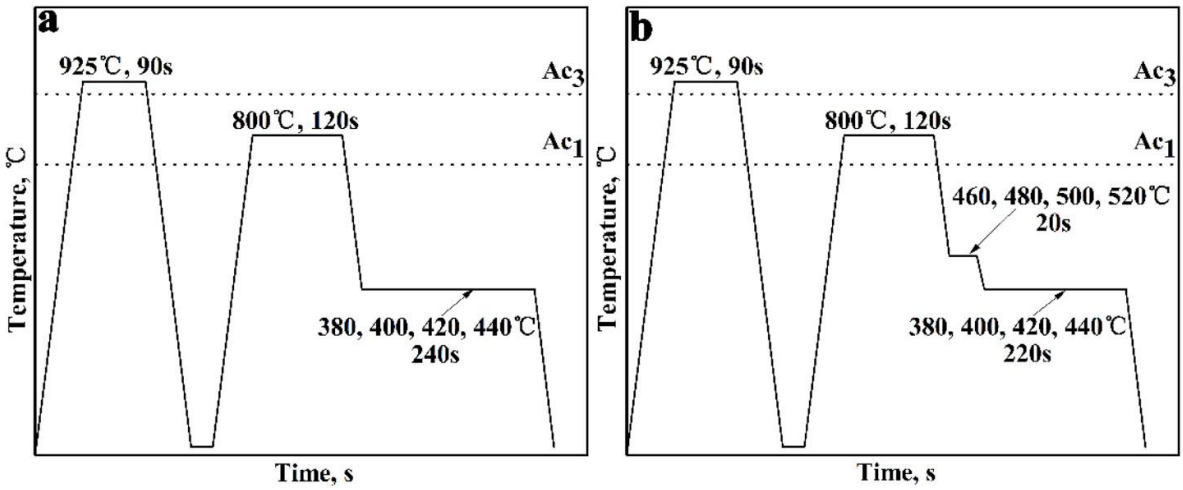

Figure. 1-9. Schematic of heat treatments of (a) one-step bainite treatment and (b) two-step bainite treatment [93].

1.2.3 Deformation micromechanics of retained austenite

The TRIP effect of retained austenite is the key factor to determine the mechanical properties of TRIP-aided steels [94, 95]. The TRIP effect is mainly controlled by the content of retained austenite and their stability [96–98].

Figure. 1-10 shows schematically the TRIP effect in TRIP-aided steels. The retained austenite transforms to deformation-induced martensite during deformation, resulting in an increase of work hardening rate. There are three types of temperature ranges with respect to the transformation mechanisms of retained austenite according to the difference of retained austenite stabilities, as shown in Figure. 1-11 [62]: (1) M_s–M_s^σ range: Stress-induced martensite transformation of retained austenite occurred at pre-existing nucleation sites, resulting in yielding of retained austenite. The stress needed for the martensitic transformation increased with increasing the temperature, which is attributed to the decrease of transformation driving force. When the temperature is M_s^σ temperature, the stress needed for the martensitic transformation equals the yield strength (YS) of the retained austenite (Figure. 1-11(a)). (2) M_s^σ–M_d range: The retained austenite is strained because the stress for martensite formation is higher than the yield strength of retained austenite, resulting in strain-induced transformation. Moreover, the martensite nucleation sites are intersection of slip. (3) $T > M_d$ range: No martensitic transformation occurred due to the high stacking fault energy and low driving force for martensite formation. Therefore, deformation is driven by dislocation glide in this range.

The main factors determining the stability of retained austenite are as follows:

(1) Chemical composition [99–101].

C content determines the chemical driving force for the transformation of retained austenite to martensite and increasing the C content can significantly reduce the M_s temperature of austenite, and then improve the stability of retained austenite. The average carbon content of the retained austenite in TRIP-aided steels should be above 0.95% because the low C content in retained austenite caused an early transformation of retained austenite to martensite. However, high C content in retained austenite makes the retained austenite too stable during deformation, leading to the occurrence of no deformation-induced martensitic transformation. In addition, Mn and Ni have similar effects to C. Therefore, it is necessary to control stability of retained austenite to optimize ductility of TRIP-aided steels.

(2) Size and morphology of retained austenite [102, 103]

The size and morphology of retained austenite grains are also important factors affecting its stability. Generally, the morphology of retained austenite in TRIP-aided steels exhibited two types: filmy and blocky. It has been suggested that larger retained austenite is unstable and transforms easily into deformation-induced martensite at small strains. Meanwhile, it has been shown that the coarse blocks of retained austenite located in the ferrite or at the ferrite/bainite interface transform to martensite at an early stage of plastic deformation, while the filmy retained austenite presents between the bainitic ferrite laths is more stable.

(3) Distribution of retained austenite [104, 105]

The effect of neighbouring phases on the retained austenite stability was investigated in previous study [104], The retained austenite was located in the vicinity of hard phases (*i.e.*, bainite or martensite), which showed high stability due to the stress shielding effect by the surrounding hard phase. Moreover, the retained austenite in vicinity of neighbouring phases effect the stress partitioning between them.

(4) Deformation conditions [106, 107]

Deformation conditions, *e.g.*, strain rate, and deformation temperature, play a significant role in the deformation-induced transformation of retained austenite during plastic deformation. It has been found that the transformation of retained austenite is sensitive to the stress state. However, there has been little research on the effect of deformation temperature on the stability of retained austenite in TRIP-aided steels.

In addition, several models have been presented to describe the kinetics of the deformation-induced martensitic transformation. The equations, which have been proposed to calculate the volume fraction of strain-induced martensite, are listed in Table 1-1 [69]. They were used in the present contribution to describe the transformation of the retained austenite in TRIP-aided steels. Nevertheless, efforts to understand the

transformation kinetics and their relation to flow properties in high-strength TRIP-aided steels have been hampered by a lack of experimental information from the region of initial inhomogeneous flow.

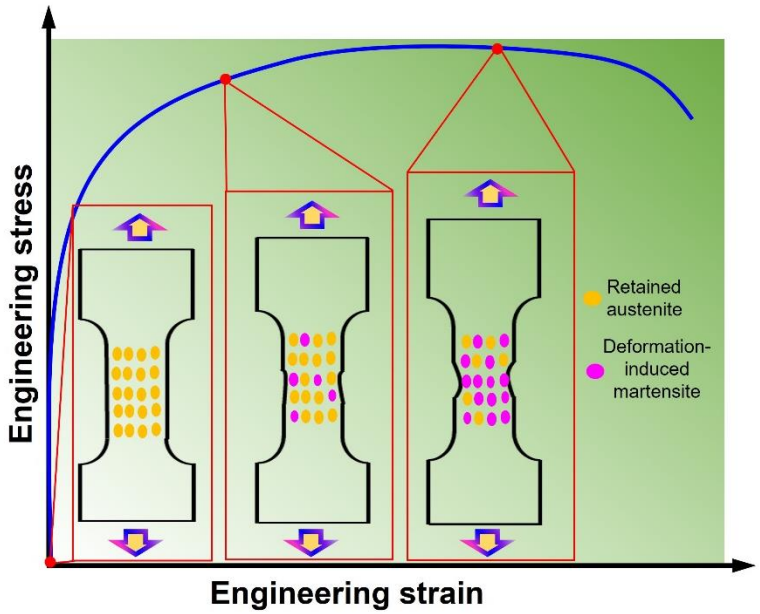

Figure. 1-10 Schematic illustration of TRIP effect during deformation in TRIP-aided steels.

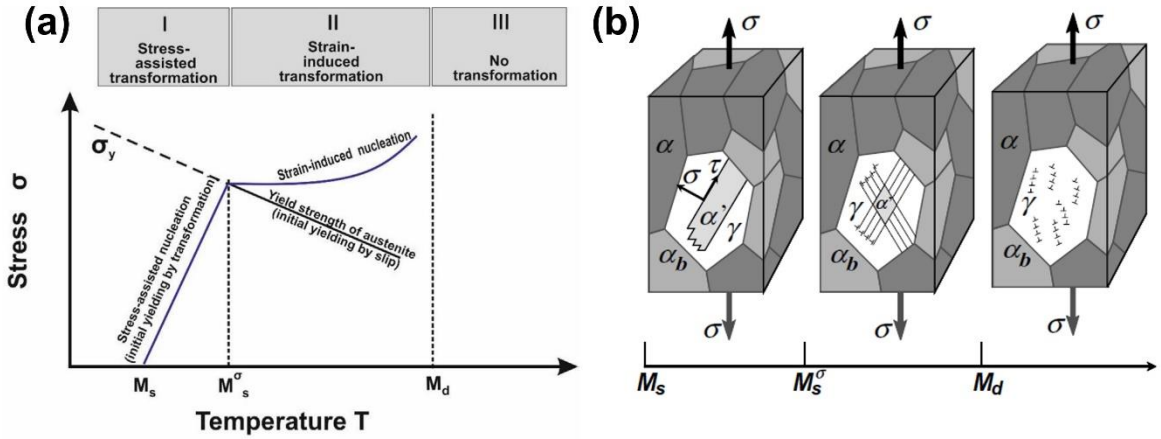

Figure. 1-11 (a) Critical stress for deformation -induced martensite formation at various temperature, and (b) schematic illustrating the dominant deformation mechanisms in different temperature ranges in the retained austenite in TRIP-aided steels [62].

Table 1-1. Models for the deformation-induced martensitic transformation kinetics [69]

Name	Equation
Ludwigson et al	$V_{\alpha'}=\frac{V_\gamma^0}{1+\frac{1}{e^k\varepsilon^p}}$
Burke et al	$V_{\alpha'}=\frac{V_\gamma^0}{1+\frac{p}{k_p\varepsilon^p V_\gamma^0}}$
Sugimoto et al	$V_{\alpha'}=V_\gamma^0(1-\exp(-k_s\varepsilon))$
Pychmintsev et al	$V_{\alpha'}=V_\gamma^0(1-\exp(-(k_s\beta_h P_h)\varepsilon))$
Olson et al	$V_{\alpha'}=V_\gamma^0(1-\exp[-\beta(1-\exp(-\alpha\varepsilon))^n])$
Gerberich et al	$V_{\alpha'}=V_\gamma^0 A\varepsilon^{1/2}$
Guimarães et al	$V_{\alpha'}=V_\gamma^0(1-\exp(-(k_G\varepsilon^z))$

$V_{\alpha'}$ is the volume fraction of deformation-induced martensite, V_γ^0 is the initial volume fraction of retained austenite, A, k_G, and z are constants, k, k_p, and k_s are constants related to the austenite stability, p is the autocatalytic strain exponent, P_h is the hydrostatic pressure during tensile tests, β_h is the hydrostatic pressure sensitivity, and α, β, and n are temperature-dependent constants.

1.3 Hydrogen embrittlement

Johnson first observed the effect of hydrogen on the ductility of iron in 1875 by temporarily dipping iron in acids for a few minutes [108]. Since then, extensive studies have been found that the phenomenon is not only restricted to iron and steels but also occurs in many materials such as Ni-based alloys, Al alloys and high entropy alloys [109–112]. The researchers define HE as a phenomenon in which hydrogen degrades the mechanical properties of metals leading to a significant reduction in ductility and fracture toughness [113]. The current understanding of HE is that hydrogen from the environment dissolves into steel, migrates as atomic hydrogen towards internal stress centers such as crack tips, and ultimately facilitates cracks, leading to failure [114]. In fact, HE is a complex process depending on the material, stress, and environment, as shown in Figure. 1-12 [115]. Meanwhile, various methods such as constant load test, U-bend test, and slow strain rate tensile (SSRT) test have applied to evaluate HE susceptibility, which reveal the transition of the fracture mode from ductile to brittle fractures such as intergranular or quasi-cleavage fractures [116–118]. Correspondingly, the multi-scale analysis methods to HE study are presented in Figure. 1-13 [119, 120]. Moreover, the nature mechanisms of HE and hydrogen charging methods control of different hydrogen-induced damage in

steels were investigated in detail [121, 122]. Unfortunately, although these studies have demonstrated that very small amount of hydrogen can cause material failure or unexpected catastrophic fracture for more than a century, premature failure of metal components due to HE continues to plague industry and academia.

In recent years, AHSSs have drawn attention as high performance structural parts for automotive, and other applications. However, HE is still a major concern for their application [123, 124]. Furthermore, another effect of hydrogen on TWIP steel is the so-called hydrogen-induced delayed fracture, during which the hydrogen-delayed cracks under constant load, which can be less than the load corresponding to the yield stress of TWIP steel [125]. In addition, AHSSs were generally composed of multiphase microstructure such as ferrite and metastable retained austenite. However, each microstructural constituents show different traps of hydrogen, a particular interaction with hydrogen and hydrogen-induced cracks (Figure. 1-14) [126]. For example, the diffusivity and solubility of hydrogen significantly differs between ferrite and austenite due to their crystal structures, *i.e.*, body centered cubic (BCC) and face centered cubic (FCC), respectively [127]. Furthermore, martensite shows a hydrogen diffusivity lying in between ferrite and austenite [128]. Since the ductility of TRIP-aided steels is partially based on the deformation-induced transformation of retained austenite into martensite, their interaction with hydrogen is of key importance. Hence, it is very important to estimate HE susceptibility and to understand the fracture mechanism of AHSSs.

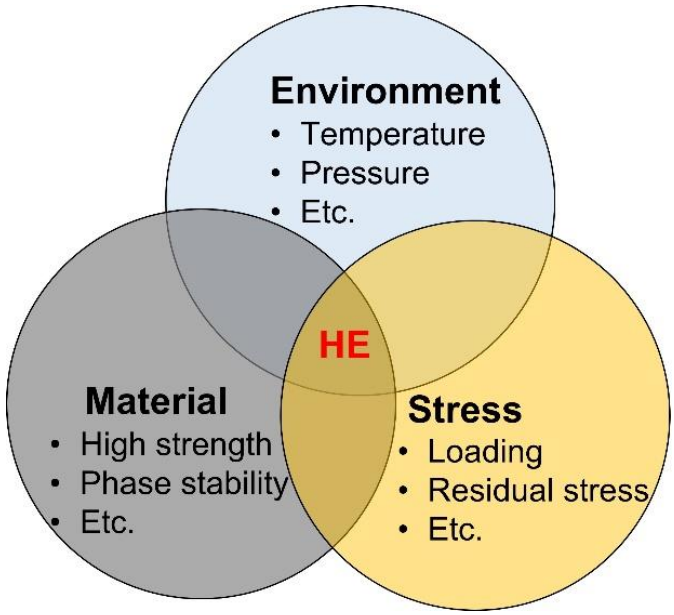

Figure. 1-12 Schematic illustrations of factors of HE.

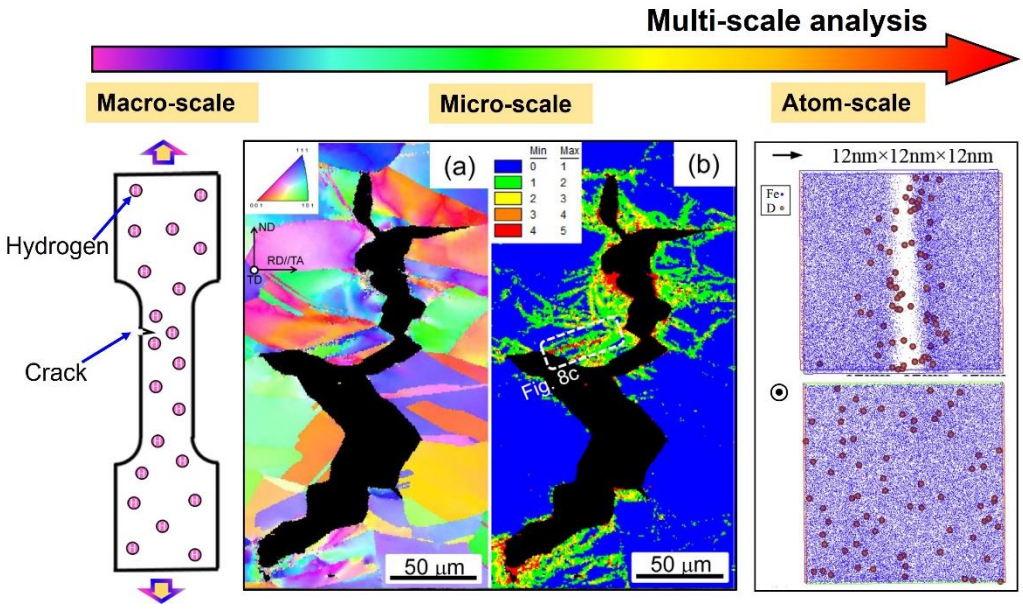

Figure. 1-13 Multi-scale analysis of HE [119, 120].

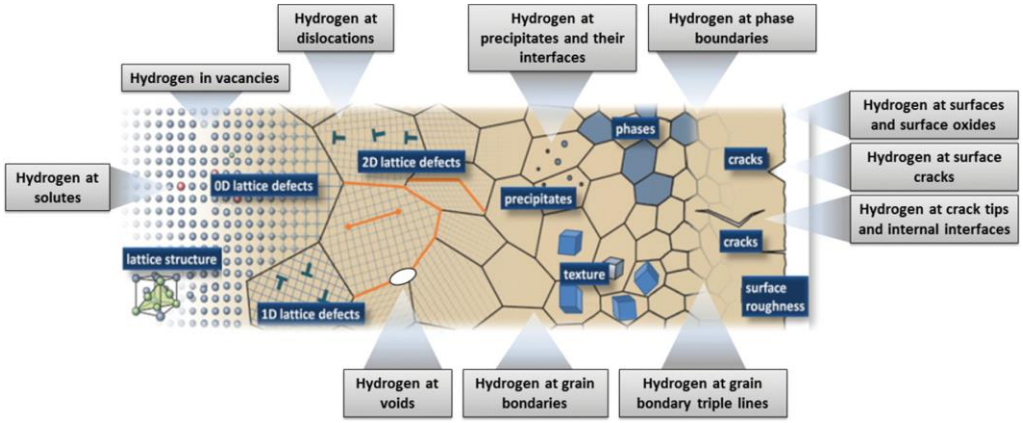

Figure. 1-14 Schematic illustrations of sites and traps for hydrogen in micro-scales [126].

1.3.1 Example of hydrogen embrittlement failure

In this section, an overview of HE faced in different application fields such as nuclear power plants, thermal power plant, and automotive applications is given. Meanwhile, the complexity, critical problems, and challenges of understanding HE are summarized.

(1) Boiling water reactor [16, 129]

Nuclear energy is considered an important resource for reducing greenhouse gases and associated climate change. The boiling water reactors is predominant reactor design around the world, which plays an important role in the utilization of nuclear energy. The core of a nuclear reactor presents a harsh environment for materials due to the

combination of high temperature, high stresses, a chemically aggressive coolant, and intense radiation, which poses a great threat or challenge to the service life of materials. Moreover, major pressure boundary components (*e.g.*, steam generator, steam lines, turbine, and condenser) are made of either low carbon or low alloy steel. which are exposed to high temperature and high hydrogen atmosphere for a long time. The hydrogen can permeate in steels from the service environment exposure, resulting in a significant decrease in ductility and premature failure of steels in pressurized / boiling water reactor [16]. Figure. 1-15 shows the Brunswick Nuclear Plant Unit 1 N004B narrow range reactor water level instrument failed high and shows the picture of failed 1-inch coupling, which threats the normal operation of the nuclear power plant and might cause catastrophic accidents. Therefore, development of hydrogen resistance steels having high specific strength and ductility has become an importance for improving safety in pressurized / boiling water reactor [129].

(2) Thermal power plant [130]

Pipelines in thermal power plants often serve in an atmosphere of high temperature, high pressure, and water vapor, which can easily lead to hydrogen entering the pipes corrosion in the region. or hydrogen embrittlement of the pipes (Figure. 1-16) [130]. Moreover, an uneven saturation of industrial components with hydrogen, made of different grades of steel, is a typical phenomenon for the in-situ hydrogenation during their operation. Hence, prolonged service under these conditions leads to HE and corrosion of the pipe steel. This phenomenon can pose a risk to the sustainability of oil and pipe steel. Based on the above, the microstructure control plays a crucial role in controlling the mechanical properties and the enhancement of ductility and hydrogen resistance steels.

(3) Automotive [131, 132]

The development of AHSSs for automotive sheet steel applications has been an important focus of research driven by the need of lightweight vehicle body and increased passenger safety. AHSSs must adopt complex and long production processes to obtain excellent mechanical properties, which inevitably introduces some hydrogen into the steel (Figure. 1-17) [132]. The hydrogen can permeate in steels from the production process such as pickling, electroplating, and welding, product assembling, and service environment exposure. Moreover, the strengths of those steels often exceed 1 GPa that is a critical value to consider a risk of the mechanical degradation by hydrogen. In addition, the bolts installed on the bottom control frame of the automotive are prone to hydrogen delayed fracture, and the fracture surface exhibited intergranular fracture (Figure. 1-18). Multiphase microstructure in such steels bring great challenges of revealing the direct

effect of HE. Therefore, the HE behavior of steel has received more and more attention and has become a hot spot of great concern to researchers from all over the world. Concern on HE is growing in the sheet steels for automotive parts.

Figure. 1-15 Configuration of boiling water reactor and failure site [129].

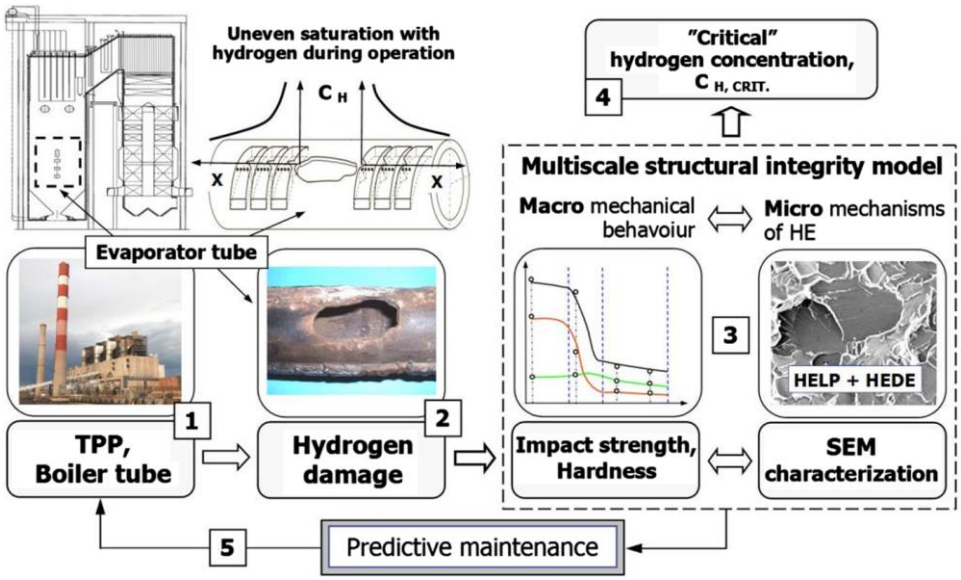

Figure. 1-16 The special multiscale approach for investigation of hydrogen-induce damage in thermal power plant: (1) Industrial component, thermal power plant boiler tube; (2) Hydrogen damage of boiler evaporator tube unevenly saturated with hydrogen during exploitation; (3) Application of a structural integrity model-correlation between material macromechanical behavior and simultaneously active HE micro-mechanisms; (4) Assessment of hydrogen critical concentrations; (5) Predictive maintenance activities [130].

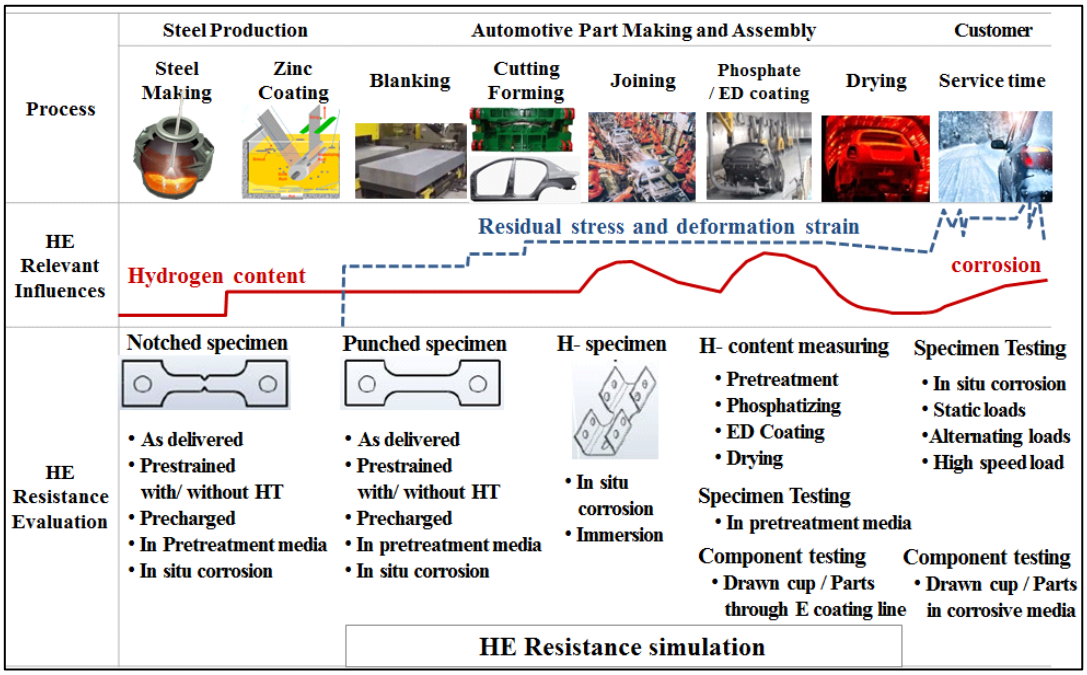

Figure. 1-17 Automotive part making process and simulation test method for HE [132].

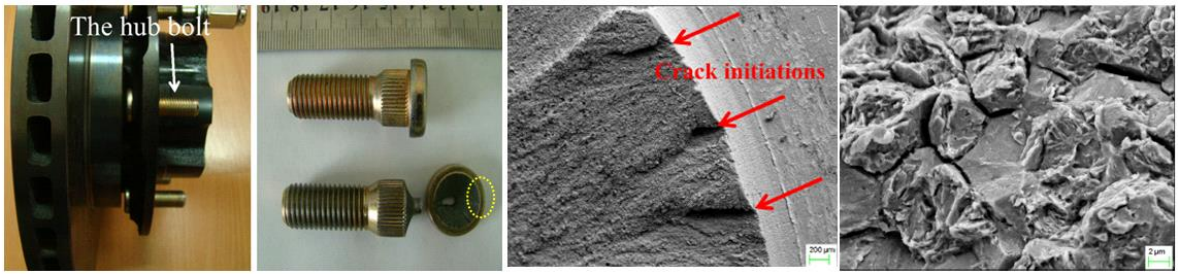

Figure. 1-18 Field case of HE of break hub disk bolt and fractography [132].

1.3.2 Factors influencing hydrogen embrittlement in steel

HE is related to factors such as diffusible hydrogen content, strength level, microstructure, and strain rate. The following summaries are mainly based on the reports of TRIP-aided steels and other types of steels.

(1) Hydrogen content [133, 134]

Hydrogen content is known to be one of the most harmful factors in steel because the presence of that in steels might cause a detrimental effect on mechanical properties. Generally, the presence of a few parts per million weights of hydrogen in steels may cause a dramatic reduction of elongation to fracture, result in a loss of ductility. Figure. 1-19 shows the effect of hydrogen on notched tensile strength with the measured hydrogen contents for notched specimen. The increase of hydrogen content results in a decrease of notched tensile strength.

(2) Strength level [135, 136]

Under the same applied stress, the concentration of hydrostatic pressure near the crack tip or notch increases with the increase of the strength level of the steel material, so the HE susceptibility usually increases with the increase of the strength level. The higher tensile in TRIP980 steel strength exhibited more sensitive hydrogen embrittlement compare with TRIP780 steel, as shown in Figure. 1-20 [136].

(3) Microstructure [136, 137]

Microstructure is a key factor affecting HE, and reasonable microstructure design is the current focus of developing AHSSs with high strength and low HE susceptibility. Various microstructure concepts have been proposed in steels and succeeded in obtaining ultra-high strength without serious loss of elongation. In this regard, Martensite is recognized as the most sensitive microstructure to hydrogen embrittlement due to its high strength level and many microstructural defects (such as prior austenite grain boundaries, lath boundaries, dislocations), as shown in Figure. 1-21 [136]. Ferrite and bainitic ferrite have relatively low HE susceptibility compared with martensite. The effect of austenite on HE susceptibility is not conclusive, and there is still a lot of controversy. austenite has high hydrogen solubility and low hydrogen diffusion coefficient compared with other microstructures. It is believed that austenite can play the role of hydrogen trap and improve the HE resistance such as austenitic stainless steel. However, A disadvantage of the deformation-induced martensitic transformation of retained austenite is the increase in hydrogen diffusivity which assists hydrogen-defects interactions and hydrogen segregation to weak microstructural constituents, resulting the initiation and propagation of hydrogen-assisted crack. From this point of view, hydrogen-resistant steels were designed by increasing the stability of retained austenite. On the other hand, TRIP effect of retained austenite in TRIP-aided steels achieve combination of strength and ductility during deformation. For this reason, microstructure design in TRIP-aided steels and medium Mn steels requires consideration of both TRIP effect and HE resistance in presence of hydrogen.

(4) Strain rate [138–140]

HE is related to the strain rate during the plastic deformation. In particular, a decrease in the strain rate enables hydrogen diffusion to specific microstructures and crack tips, leading to severe HE, because the rate of hydrogen diffusion keeps up with the dislocation movement. Furthermore, the strain rate affects the behavior of dislocation-hydrogen competitive motion, which can alter the evolution of dislocation patterns. These factors cause the acceleration of HE with a decrease in the strain rate. Hao *et al.* [140] reported that HE susceptibility in TWIP steel increases with a decrease in the strain rate.

Furthermore, the primary effect of the decrease in strain rate on HE is the acceleration of the crack propagation. In addition to the promotion of martensitic transformation, a decrease in the strain rate in the presence of hydrogen may cause hydrogen localization at the crack tip, which assists brittle-like martensite cracking.

(5) Pre-strain [141–143]

HE susceptibility depends on pre-strain. For example, Maeda *et al.* [142] reported that pre-strain altered hydrogen-assisted crack site and local hydrogen diffusivity in a nitrogen-doped duplex steel. The changes in dislocation and hydrogen behaviors associated with pre-straining altered the cracking sites in the austenite and ferrite, and decreased HE susceptibility. Verma *et al.* [143] reported that pre-straining to 3% and 6% improved the crack growth resistance in TBF steel because of a reduction in the probability of austenite presence at the crack tip. Moreover, a high level of pre-strain provided high hydrogen concentration and resulted in strain-age-hardening, which resulted in an acceleration of quasi-cleavage fracture.

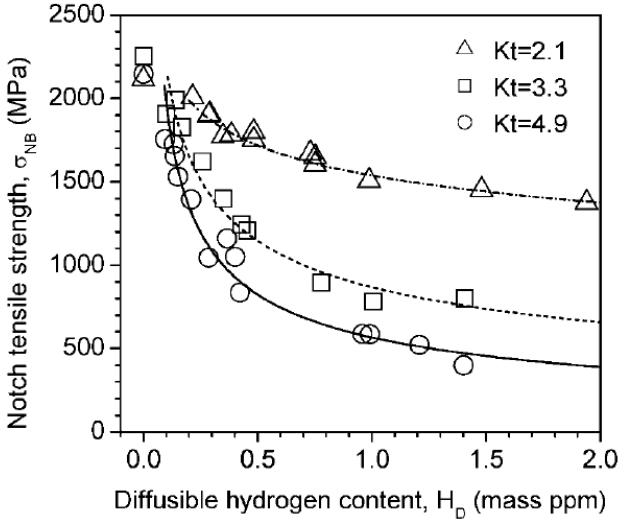

Figure. 1-19 Dependence of notch tensile strength on diffusible hydrogen content for specimens with various stress concentration factors [134].

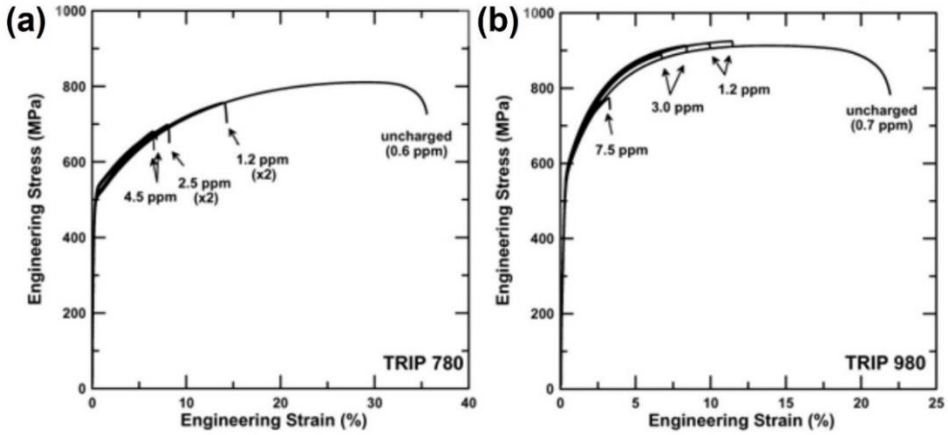

Figure. 1-20 Dependence of HE susceptibility on strength level in TRIP-aided steel [136].

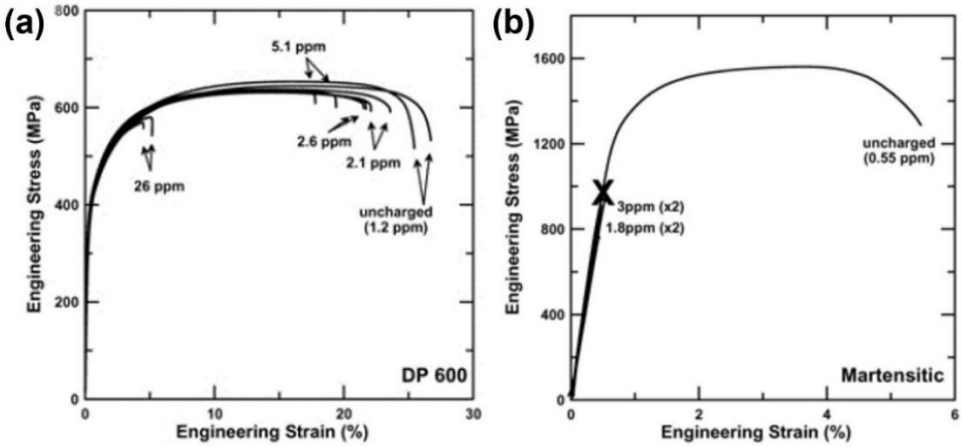

Figure. 1-21 Effect of the microstructure on the HE in DP and martensitic steels [136].

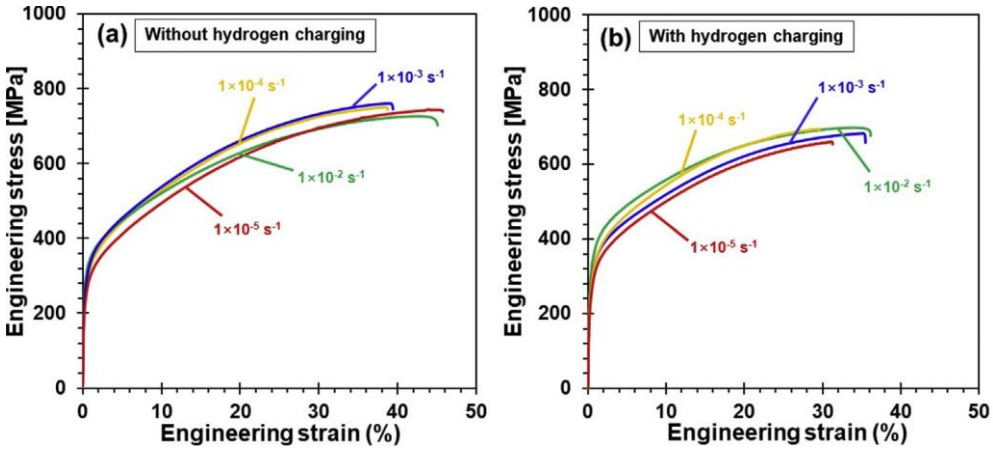

Figure. 1-22 Tensile behavior of hydrogen-uncharging and hydrogen-charging specimens at various strain rates [140].

1.3.3 Hydrogen embrittlement mechanisms

The fundamental mechanisms for HE have been extensively studied over the past several decades [144–146]. Moreover, numerous experimental and theoretical models have been investigated to account for the HE in various materials under different hydrogen charging conditions [147–150]. However, it is still a controversial question without a clear consensus. Most of the HE without hydrides formation can be explained by using one or a combination of these mechanisms. The proposed mechanisms are introduced as following.

(1) Hydrogen-enhanced decohesion [114, 151, 152]

The hydrogen-enhanced decohesion (HEDE) mechanism was first proposed, and further developed in detail by Oriani and McMahon [151]. The cohesive energy between atoms reduces when hydrogen atoms are trapped at the grain boundaries, interphases, and interfaces, as shown in Figure. 1-22 [152]. When the applied stress exceeds the cohesive stress or strength, resulting in the initiation and propagation of intergranular cracks. In the other words, the accumulated hydrogen at crack fronts reduces the interatomic cohesive forces and thus leads to crack propagation at a lower stress level than in a low hydrogen situation. The HEDE mechanism was widely accepted for explaining intergranular fracture in presence of hydrogen.

(2) Adsorption-induced dislocation emission [153, 154]

The adsorption-induced dislocation emission (AIDE) model, proposed by Lynch et al. [153], thus highlights the effects of surface-absorbed hydrogen on promoting dislocation emission at the surface. It is essentially a model describing the interaction between surface and hydrogen atoms including internal diffusible hydrogen and environmental hydrogen.

(3) Hydrogen-enhanced local plasticity [152, 155–158]

Beachem [155] firstly proposed the hydrogen-enhanced localized plasticity (HELP) mechanism of HE responsible for the hydrogen-related fracture, which is based on the hydrogen-enhanced dislocation mobility and dislocation slip behavior around a crack tip. Hence, the hydrogen atmospheres enhance the dislocation mobility and promoted localized plastic deformation. The HELP mechanism is verified by experimental observations (*i.e.*, transmission electron spectroscopy) of enhanced dislocation motion and dislocation slip in the vicinity of the crack tip. For example, Martin *et al*. [158] revealed that fracture origins are generated at the intersections of dislocation planar slip lines, leading to the initiation and propagation of quasi-cleavage cracks in the strain localization region through the expansion of fracture origins along intense slip lines in

pipeline steels. In addition, the HELP mechanism is also supported by the appearance of quasi-cleavage fracture and surface slip line rearrangement in hydrogen-charged specimens.

(4) Hydrogen-enhanced strain-induced vacancies [159, 160]

Hydrogen-enhanced strain-induced vacancies (HESIV) model was proposed based on thermal desorption spectrometry (TDS) in iron and low alloyed ferritic steels. HESIV means that hydrogen can increase the formation of vacancies, and stabilize them, which results in clusterings of vacancies. In addition, HESIV mechanism was also supported by the positron annihilation spectroscopy where the mean positron lifetime in iron was found to be increased by tensile straining and such increase was further enhanced in the presence of hydrogen. Nagumo *et al*. [160] reported that hydrogen trapped at vacancies accelerated the agglomeration of vacancies to form nano voids, resulting in the propagation of hydrogen-induced quasi-cleavage cracks via the coalescence of nano voids.

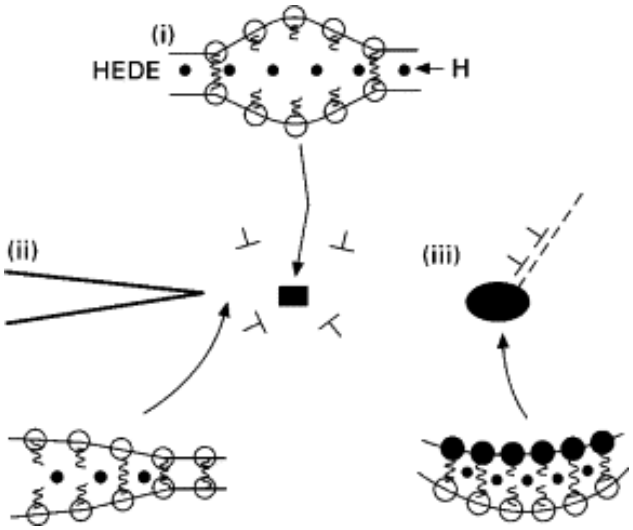

Figure. 1-22 Schematic diagram showing the failure mechanism induced by the HEDE mechanism [152].

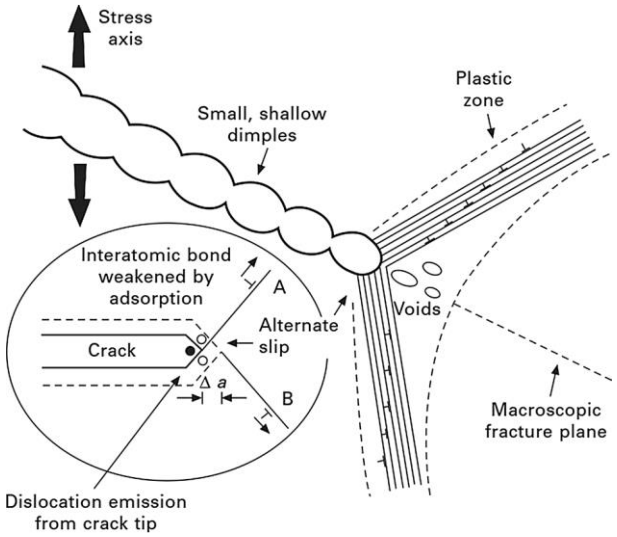

Figure. 1-23 Schematic diagram showing the failure mechanism induced by the AIDE mechanism [154].

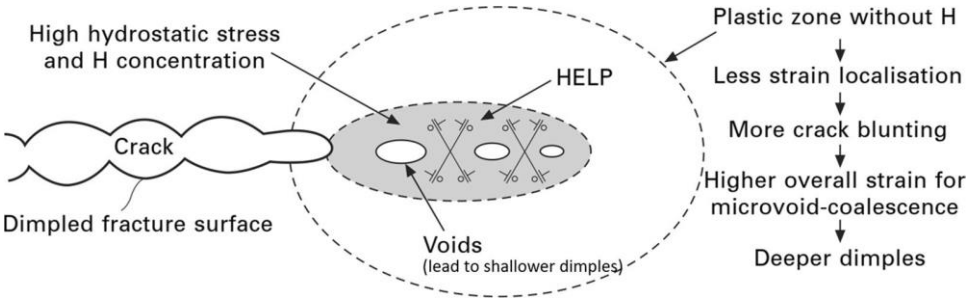

Figure. 1-24 Schematic diagram showing the failure mechanism induced by the HELP mechanism [152].

1.4 Purpose of this study

Striving for developing alloys with high strength and sufficient uniform ductility has been an imperative challenge in structural applications. the concept of a carbide-free bainite matrix has been developed for low-carbon low-alloy TRIP-aided steels due to better mechanical properties than the first generation of AHSSs and the potentially lower costs than the TWIP steels, which can obtain UTS of over 1 GPa and TEl of about 25%. Therefore, the objective of this research focus on the microstructure evolution and hydrogen embrittlement behaviors in TBF steel. Firstly, we focus on the effect of austempering time on mechanical properties and fracture behavior in TBF steel, which aims to establish optimum heat-treatment conditions to achieve the strength increase by bainitic ferrite and the elongation improvement by retained austenite in 0.4%C-bearing TBF cold rolled steel sheets. More specifically, it is the aim of this study to elucidate the relationship between the mechanical properties and fracture behavior as a function of the

austempering time in TBF steel. And then, investigation of the synergistic effects of deformation temperature and hydrogen on the transformation of retained austenite and mechanical properties in TBF steel was conducted. In particular, the micro-damage evolution associated with deformation-induced martensitic transformation was systematically investigated. On that basis, it is shown that how the deformation temperature is significant regarding micro-damage evolution and the associated fracture behavior of the TBF steel. The thesis outline and research methods of the present study are as follows.

1.4.1 Thesis outline

The objective of this research is to develop a better understanding of the austempering time-microstructure-property relationship of 0.4%C-bearing TBF steel. The study specifically focuses on the following aspects:

Chapter 1 introduces the background and objectives of the research. Moreover, the extensive literature review and the state of the knowledge on TRIP-aided steel and HE are presented to understand the current challenges of HE in TRIP-aided steel.

Chapter 2 displays the experiment procedure and various characterization methods in this study used to support these inclusions.

Chapter 3 focuses on the effect austempering time on the microstructure and mechanical properties of TBF steel. and reveals the detailed deformation and fracture mechanisms of TBF steel, which was analyzed the processing-microstructure-properties relationship.

Chapter 4 investigates the hydrogen and deformation temperature on mechanical properties of TBF steel. Detailed transformation behavior of retained austenite and fracture mechanisms of were investigated to understand the behavior of each phase in the presence of hydrogen.

Chapter 5 focuses on the quantitative evaluation of hydrogen and deformation temperature effects on evolutions of deformation-induced martensite and micro-damage to elucidate the temperature effects on microstructure-dependent damage behaviors in TBF steel.

Chapter 6 summarizes the conclusions of the thesis and highlights promising avenues for future work based on our deeper understanding of the microstructure evolution and HE behavior in TBF steel.

1.4.2 Research methods

The objective of the thesis is summarized in the schematics shown in Figure. 1-25. The microstructures of the specimens in present study were characterized using X-ray diffraction (XRD), SEM, and electron backscattered diffraction (EBSD). The volume fraction of retained and the carbon content in retained austenite were calculated according to the XRD results. Electrochemical hydrogen charging was carried out to the introduction hydrogen into specimens, and then SSRT tests were performed at deformation temperature of -100, -30, 21 and 100 ℃. Hydrogen contents were analyzed by TDS. To focuses on the micro-mechanisms responsible for the observed hydrogen embrittlement behavior, the correlation between the microstructural features and the hydrogen-assisted crack was explored in detail by SEM or electron channelling contrast imaging (ECCI) and EBSD. Moreover, the quantitative evaluation of micro-damage was systematically investigated. In addition, the fracture surfaces were observed using SEM.

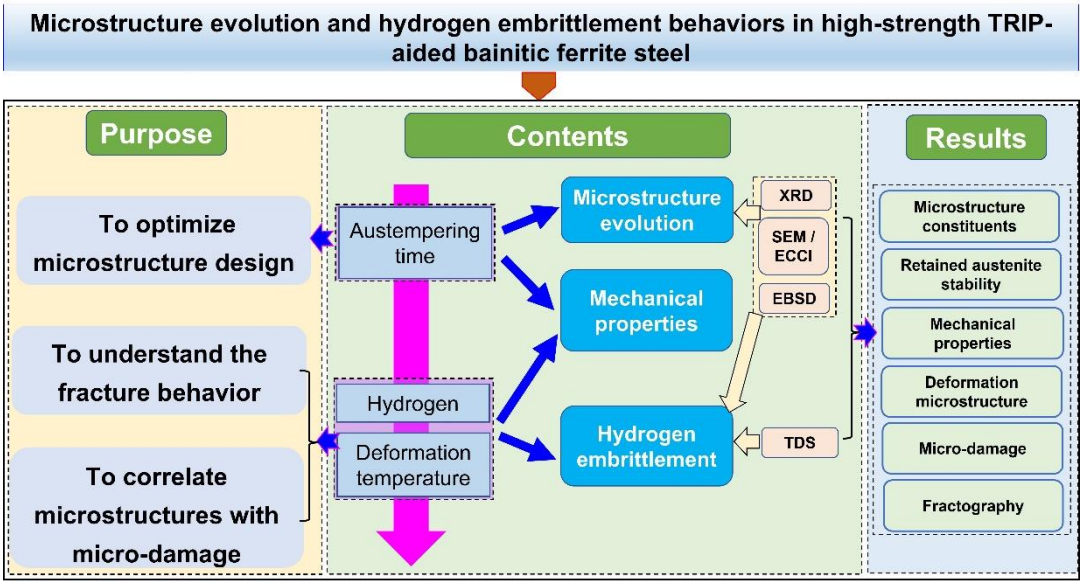

Figure. 1-25 Schematic diagram showing the thesis outline and research methods.

1.5 References

[1]. J. L. Cann, A. D. Luca, D. C. Dunand, D. Dye, D. B. Miracle, H. S. Oh, E. A. Olivetti, T. M. Pollock, W. J. Poole, R. Yang, C. C. Tasan, Sustainability through alloy design: Challenges and opportunities, Prog. Mater. Sci. 117 (2021) 100722.

[2]. D. Raabe, C. C. Tasan, E. A. Olivetti, Strategies for improving the sustainability of structural metals, Nature, 575 (2019) 64–74.

[3]. M. Koyama, Z. Zhang, M. Wang, D. Ponge, D. Raabe, K. Tsuzaki, H. Noguchi, C. C. Tasan, Bone-like crack resistance in hierarchical metastable nanolaminate steels, Science. 355 (2017) 1055–1057.

[4]. P. Sathiyamoorthi, H. S. Kim, High-entropy alloys with heterogeneous microstructure: Processing and mechanical properties, Prog. Mater. Sci. 117 (2022) 100709.

[5]. E. P. George, W. A. Curtin, C. C. Tasan, High entropy alloys: A focused review of mechanical properties and deformation mechanisms, Acta Mater. 188 (2020) 435–474.

[6]. M. Tiryakioğlu, J, Campbell, N. D. Alexopoulos, Quality indices for aluminum alloy castings: A critical review, Metall. Mater. Trans. B. 40 (2009) 802–811.

[7]. D. Herzog, V. Seyda, E. Wycisk, C. Emmelmann additive manufacturing of metals, Acta Mater. 117 (2016) 371-392.

[8]. P. Bajaj, A. Hariharan, A. Kini, P. Kürnsteiner, D. Raabe, E. A.Jägle, Steels in additive manufacturing: A review of their microstructure and properties, Mater. Sci. Eng. A. 722 (2020) 138633.

[9]. J. Zhao, Z. Jiang, Thermomechanical processing of advanced high strength steels, Prog. Mater. Sci. 94 (2018) 174–242.

[10]. D. Raabe, B. Sun, A. K. D. Silva, B. Gault, H. W. Yen, K. Sedighiani, P. Thoudden Sukumar, I. R. S. Filho, S. Katnagallu, E. Jägle, P. Kürnsteiner, N. Kusampudi, L. Stephenson, M. Herbig, C. H. Liebscher, H. Springer, S. Zaefferer, V. Shah, S. L. Wong, C. Baron, M. Diehl, F. Roters, D. Ponge, Current challenges and opportunities in microstructure-related properties of advanced high-strength steels, Metall. Mater. Trans. A. 51 (2020) 5517–5586.

[11]. D. Raabe, H. Springer, I. G. Urrutia F. Roters, M Bausch, J. B. Seol, M. Koyama, P. P. Choi, K. Tsuzaki, Alloy design, combinatorial synthesis, and microstructure–property relations for low-density Fe-Mn-Al-C austenitic steels, JOM. 66 (2014), 1845–1856.

[12]. Advanced high-strength steels application guidelines, Version 5.0, 2014,

WorldAutoSteel, www.worldautosteel.org.

[13]. M. Singh, Application of steel in automotive industry, Int. J. Emerg. Technol. Adv. Eng. 6 (2016), 246–53.

[14]. W. Bleck, X. F. Guo, Y. Ma, The TRIP effect and its application in cold formable sheet steels, Steel Res. Int. 88 (2017) 1–21.

[15]. S. Zaefferer, J. Ohlert, W. Bleck, A study of microstructure, transformation mechanisms and correlation between microstructure and mechanical properties of a low alloyed TRIP steel, Acta Mater. 52 (2004) 2765–2778.

[16]. S. J. Zinkle, G. S. Was, Materials challenges in nuclear energy, Acta Mater. 61 (2013) 735–758.

[17]. C. Lesch, N. Kwiaton, F. B. Klose, Advanced high strength steels (AHSS) for automotive applications: tailored properties by smart microstructural adjustments, Steel Res. Int. 88 (2017) 170020.

[18]. R. Ranjan, H. Beladi, S.B. Singh, P.D. Hodgson, Thermo-mechanical processing of TRIP-aided steels, Metall. Mater. Trans. A. 46 (2015) 3232–3247.

[19]. C. C. Tasan, M. Diehl, D. Yan, M. Bechtold, F. Roters, L. Schemmann, C. Zheng, N. Peranio, D. Ponge, M. Koyama, K. Tsuzaki, D. Raabe, An overview of dual-phase steels: advances in microstructure-oriented processing and micromechanically guided design, Annu. Rev. Mater. Res.45 (2015) 391–431.

[20]. G. A. Cingaraa, Y. Ososkov, M. K. Jain, D. S. Wilkinsona, Effect of martensite distribution on damage behaviour in DP600 dual phase steels, Mater. Sci. Eng. A. 516 (2009) 7–16.

[21]. S. Curtze, V. T. Kuokkala, Dependence of tensile deformation behavior of TWIP steels on stacking fault energy, temperature and strain rate, Acta Mater. 58 (2010) 5129–5141.

[22]. S. M. Lee, S. J. Lee, S. Lee, J. H. Nam, Y. K. Lee, Tensile properties and deformation mode of Si-added Fe-18Mn-0.6C steels, Acta Mater. 144 (2018) 738–747.

[23]. A. S. Akbari, L. Mosecker, A. Schwedt, W. Bleck, Characterization and prediction of flow behavior in high-manganese twinning induced plasticity steels: Part I. mechanism maps and work-hardening behavior, Metall. Mater. Trans. A. 43 (2012) 1688–1704.

[24]. J. Yoo, K. Choi, A. Zargaran, N. Kim, Effect of stacking faults on the ductility of Fe-18Mn-1.5Al-0.6C twinning-induced plasticity steel at low temperatures, Scr. Mater. 137 (2017) 18–21.

[25]. B. C. De Cooman, O. Kwon, K. G. Chin, State-of-the-knowledge on TWIP steel,

Mater Sci. Tech. 28 (2012) 513–527.

[26]. A. S. Akbari, A. K. Mishra, J. Mayer, W. Bleck, Characterization and prediction of flow behavior in high-manganese twinning induced plasticity steels: Part II. Jerky flow and instantaneous strain rate, Metall. Mater. Trans. A. 43 (2012) 1705–1723.

[27]. K. Chung, K. Ahn, D. H. Yoo, K. H. Chung, M. H. Seo, S. H. Park, Formability of TWIP (twinning induced plasticity) automotive sheets, Int. J. Plast. 27 (2011) 52–81.

[28]. K. Rahman, V. Vorontsov, D. Dye, The effect of grain size on the twin initiation stress in a TWIP steel, Acta Mater 89 (2015) 247–257.

[29]. B. C. De Cooman, Y. Estrin, K. S. Kim, Twinning-induced plasticity (TWIP) steels, Acta Mater. 142 (2018) 283–362.

[30]. D. K. Matlock, J. G. Speer, Processing opportunities for new advanced high-strength sheet steels, Mater. Manuf. Process. 25 (2010) 7–13.

[31]. D. W. Suh, S. J. Kim, Medium Mn transformation-induced plasticity steels: recent progress and challenges, Scripta Mater. 126 (2017) 63–67.

[32]. D. V. Edmonds, K. He, F. C. Rizzo, B. C. De Cooman, D. K. Matlock, J. G. Speer, Quenching and partitioning martensite—A novel steel heat treatment, Mater. Sci. Eng. A. 438 (2006) 25–34.

[33]. K. Sugimoto, S. Hidaka, H. Tanino, J. Kobayashi, Warm formability of 0.2 pct C-1.5 pct Si-5 pct Mn transformation-induced plasticity-aided steel, Metall. Mater. Trans. A. 48 (2017) 2237–2246.

[34]. Y. Zhou, M. Koyama, T. Hojo, S. Ajito, E. Akiyama, Transformation-induced microcracks and their arrest with different deformation temperatures in a medium Mn steel, Metall. Mater. Trans. A. 54 (2023), 153–166.

[35]. E. J. Seo, L. Cho, Y. Estrin, B. C. De Cooman, Microstructure-mechanical properties relationships for quenching and partitioning (Q&P) processed steel, Acta Mater. 113 (2016) 124–139.

[36]. D. H. Kim, J. G. Speer, H. S. Kim, B. C. D. Cooman, Observation of an isothermal transformation during quenching and partitioning processing, Metall. Mater. Trans. A. 40 (2009) 2048–2060.

[37]. K. Sugimoto, M. Tsunezawa, T. Hojo, S. Ikeda, Ductility of 0.1–0.6C–1.5Si–1.5Mn ultra high-strength TRIP-aided sheet steels with bainitic ferrite matrix, ISIJ Int. 44 (2004) 1608–1614.

[38]. K. Sugimoto, Effects of partial replacement of Si by Al on cold formability in two groups of low-carbon third-generation advanced high-strength steel sheet: a review, metal. 12 (2022) 2069.

[39]. A. Laureys, T. Depover, R. Petrov, K. Verbeken, Microstructural characterization of hydrogen induced cracking in TRIP-assisted steel by EBSD, Mater. Charact. 112 (2016) 169–179.

[40]. M. Koyama, C. C. Tasan, E. Akiyama, K. Tsuzaki, D. Raabe, Hydrogen-assisted decohesion and localized plasticity in dual-phase steel, Acta Mater. 70 (2014) 174–187.

[41]. M. Koyama, E. Akiyama, Y. Lee, D. Raabe, K. Tsuzaki, Overview of hydrogen embrittlement in high-Mn steels. Int. J. Hydrog. Energy. 42 (2017) 12706–12723.

[42]. I. Jeong, K. M. Ryu, D. G. Lee, Y. Jung, K. Lee, J. S. Lee, D. W Suh, Austenite morphology and resistance to hydrogen embrittlement in medium Mn transformation-induced plasticity steel, Scripta Mater. 126 (2019) 52–56.

[43]. J. H. Ryu, Y. S. Chun, C. S. Lee, H. K. D. H. Bhadeshia, D. W. Suh, Effect of deformation on hydrogen trapping and effusion in TRIP-assisted steel, Acta Mater. 60 (2012) 4085–4092.

[44]. R. A. Oriani, The diffusion and trapping of hydrogen in steel, Acta Metall. 18 (1970) 147–157.

[45]. T. Yamashita, N. Koga, O. Umezawa, Influence of deformability of retained austenite on martensitic transformation in tension for low alloy steel at low temperatures, ISIJ Int. 58 (2018) 1155–1161.

[46]. Q. S. Allen, T. W. Nelson, Microstructural evaluation of hydrogen embrittlement and successive recovery in advanced high strength steel, J Mater Process Technol. 265 (2019) 12–19.

[47]. V. F. Zackay, E. R. Parker, D. Fahr, R. Bush, Trans. ASM, 60 (1967) 252–259.

[48]. G. B. Olson, M. Azrin, Transformation behavior of TRIP steels, Metall. Trans. A. 9 (1978) 713–721.

[49]. K. Sugimoto, M. Misu, M. Kobayashi, H. Shirasawa, Effects of second phase morphology on retained austenite morphology and tensile properties in a TRIP aided dual-phase steel sheet, ISIJ Int. 33 (1993) 775–782.

[50]. S. Zaefferer, J. Ohlert, W. Bleck, A study of microstructure, transformation mechanisms and correlation between microstructure and mechanical properties of a low alloyed TRIP steel, Acta Mater. 52 (2004) 2765–2778.

[51]. K. Sugimoto, T. Hojo, Fatigue hardening behavior of 1.5 GPa grade transformation-induced plasticity-aided martensitic steel, Metall. Mater. Trans. A. 47 (2016) 5272–5279.

[52]. P. J. Jacques, Transformation-induced plasticity for high strength formable steels, Curr. Opin. Solid State Mater. Sci. 8 (2004) 259–265.

[53]. I. B. Timokhina, P. D. Hodgson, E. V. Pereloma, Effect of microstructure on the stability of retained austenite in transformation-induced-plasticity steels, Metall. Mater. Trans. A. 35 (2004) 2331–2341.

[54]. J. Mahieu, J. Maki, B. C. De Cooman, S. Claessens, Phase transformation and mechanical properties of Si-free CMnAl transformation-Induced plasticity-aided steel, Metall. Mater. Trans. A. 33 (2002) 2573–2580.

[55]. S. Chen, Y. Wang, Y. Lin, C. Huang, J. Yang, H. Yen, Microstructure and mechanical behaviors of GPa-grade TRIP steels enabled by hot-rolling processes, Mater. Sci. Eng. A. 761 (2019) 1–13.

[56]. H. S. Park, J.C. Han, N.S. Lim, C.G. Park, Nano-scale observation on the transformation behavior and mechanical stability of individual retained austenite in CMnSiAl TRIP steels, Mater. Sci. Eng. A. 627 (2015) 262–269.

[57]. M. Wang, C. C. Tasan, D. Ponge, D. Raabe, Spectral TRIP enables ductile 1.1 GPa martensite, Acta Mater. 111 (2016) 262–272.

[58]. Y. Shen, L. Qiu, X. Sun, L. Zuo, P. K. Liaw, D. Raabe, Effects of retained austenite volume fraction, morphology, and carbon content on strength and ductility of nanostructured TRIP-assisted steels, Mater. Sci. Eng. A. 636 (2015) 551–564.

[59]. P. Christodoulou, Effect of retained austenite transformation on the fatigue behaviour of aluminum containing TRIP steels. PhD thesis.

[60]. E. P. Kwon, S. Fujieda, K. Shinoda, S. Suzuki, Characterization of transformed and deformed microstructures in transformation induced plasticity steels using electron backscattering diffraction, Mater. Sci. Eng. A. 528 (2011) 5007–5017.

[61]. M. Soleimani, A. Kalhor, H. Mirzadeh, Transformation-induced plasticity (TRIP) in advanced steels: A review, Mater. Sci. Eng. A. 795 (2020) 140023.

[62]. B. C. De Cooman, Structure-properties relationship in TRIP steels containing carbide-free bainite, Curr. Opin. Solid State Mater. Sci. 8 (2004) 285–303.

[63]. Y. Sakuma, O. Matsumura, O. Akisue, Influence of C content and annealing temperature on microstructure and mechanical properties of 400 °C transformed steel containing retained austenite, ISIJ Int. 31 (1991) 1348‑1353.

[64]. K. Sugimoto, M. Kobayashi, S. Hashimoto, Ductility and strain-induced transformation in a high-strength transformation-induced plasticity-aided dual phase steel, Metall. Trans. A. 23 (1992) 3085–3091.

[65]. E. V. Pereloma, I. B. Timokhina, M. K. Miller, P. D. Hodgson, Three-dimensional atom probe analysis of solute distribution in thermomechanically processed TRIP steels, Acta Mater. 55 (2007) 2587–2598.

[66]. J. Chiang, J. D. Boyd, A. K. Pilkey, Effect of microstructure on retained austenite

stability and tensile behaviour in an aluminum-alloyed TRIP steel, Mater. Sci. Eng. A. 638 (2015) 132–142.

[67]. G. N. Haidemenopoulos, Physical Metallurgy: Principles and Design. (2018).

[68]. S. Kaar, D. Krizan, J. Schwabe, H. Hofmann, T. Hebesberger, C. Commenda, L. Samek, Influence of the Al and Mn content on the structure-property relationship in density reduced TRIP-assisted sheet steels, Mater. Sci. Eng. 735 (2018) 475–486.

[69]. L. Samek, E. De Moor, J. Penning, B. C. De Cooman, Influence of alloying elements on the kinetics of strain-induced martensitic nucleation in low-alloy, multiphase high-strength steels, Metall. Mater. Trans. A. 37 (2006) 109–124.

[70]. A. A. Gorni, Steel forming and heat treatment handbook. 2019, 52.

[71]. H. J. Grabke, Surface and grain boundary segregation on and in iron and steels, ISIJ Int. 29 (1989) 529–538.

[72]. P. Jacques, E. Girault, T. Catlin, N. Geerlofs, T. Kop, S. Van Der Zwaag, F. Delannay, Bainite transformation of low carbon Mn-Si TRIP-assisted multiphase steels: Influence of silicon content on cementite precipitation and austenite retention, Mater. Sci. Eng. A. 273–275 (1999) 475–479.

[73]. S. J. Kim, C. G. Lee, I. Choi, S. Lee, Effects of heat treatment and alloying elements on the microstructures and mechanical properties of 0.15 wt pct C transformation-induced plasticity-aided cold-rolled steel sheets, Metall. Mater. Trans. A. 32 (2001) 505–514.

[74]. K. D. Krizan, S. Hahn, A. Pichler, Relationship between microstructure and mechanical properties in Nb–V microalloyed TRIP steel, Mater. Sci. Eng. A. 31 (2015) 661–667.

[75]. E. M. Bellhouse, J.R. McDermid, Effect of continuous galvanizing heat treatments on the microstructure and mechanical properties of high Al-low Si transformation induced plasticity steels, Metall. Mater. Trans. A. 41 (2010) 1460–1473.

[76]. S. Zaefferer, P. Romano, F. Friedel, EBSD as a tool to identify and quantify bainite and ferrite in low-alloyed Al-TRIP steels, J. Microsc. 230 (2008) 499–508.

[77]. T. Hojo, K. I. Sugimoto, Y. Mukai, S. Ikeda, Effects of aluminum on delayed fracture properties of ultra high strength low alloy TRIP-aided steels, ISIJ Int. 48 (2008) 824–829.

[78]. K. Hausmann, D. Krizana, K. S. Hahn, A. Pichler, E. Wernerc, The influence of Nb on transformation behavior and mechanical properties of TRIP-assisted bainitic–ferritic sheet steels, Mater. Sci. Eng. A. 588 (2013) 142–150.

[79]. G. K. Tirumalasetty, M. A. Van Huis, C. Fang, Q. Xu, F.D. Tichelaar, D.N. Hanlon,

J. Sietsma, H. W. Zandbergen, Characterization of NbC and (Nb, Ti) N nanoprecipitates in TRIP assisted multiphase steels, Acta Mater. 59 (2011) 7406–7415.

[80]. K. Hausmann, D. Krizan, K. Spiradek-Hahn, A. Pichler, E. Werner, The influence of Nb on transformation behavior and mechanical properties of TRIP-assisted bainitic–ferritic sheet steels, Mater. Sci. Eng. A. 588 (2013) 142–150.

[81]. D. Krizan, B. C. De Cooman, Mechanical properties of TRIP steel microalloyed with Ti, Metall. Mater. Trans. A. 45 (2014) 3481–3492.

[82]. E. Abbasi, W. M. Rainforth, Microstructural evolution during bainite transformation in a vanadium microalloyed TRIP-assisted steel, Mater. Sci. Eng. A. 651 (2016) 822–830.

[83]. S. Hashimoto, S. Ikeda, K. Sugimoto, S. Miyake, Effects of Nb and Mo addition to 0.2 % C – 1. 5 % Si – 1. 5 % Mn steel on mechanical properties of hot rolled TRIP aided steel sheets, ISIJ Int. 44 (2004) 1590–1598.

[84]. J. Kobayashi, D. Ina, N. Yoshikawa, K. I. Sugimoto, Effects of the addition of Cr, Mo and Ni on the microstructure and retained austenite characteristics of 0.2% C-Si-Mn-Nb ultrahigh-strength TRIP-aided bainitic ferrite steels, ISIJ Int. 52 (2012) 1894‑1901.

[85]. S. Cheng, X. Wang, Z. Feng, B. Clausen, H. Choo, P. K. Liaw, Probing the characteristic deformation behaviors of transformation-induced plasticity steels, Metall. Mater. Trans. A. 39 (2008) 3105–3112.

[86]. K. Sugimoto, T. Iida, J. Sakaguchi, T. Kashima, Retained austenite characteristics and tensile properties in a TRIP type bainitic sheet steel, ISIJ Int. 40 (2000) 902–908.

[87]. C. Wang, H. Ding, M. Cai, B. Rolfe, Characterization of microstructures and tensile properties of TRIP-aided steels with different matrix microstructure, Mater. Sci. Eng. A. 610 (2014) 65–75.

[88]. Z. Zhao, H. Yin, A. Zhao, Z. Gong, J. He, T. Tong, H. Hu, The influence of the austempering temperature on the transformation behavior and properties of ultra-high-strength TRIP-aided bainitic-ferritic sheet steel, Mater. Sci. Eng. A, 613 (2014) 8–16.

[89]. N. Takayama, G. Miyamoto, T. Furuhara, Effects of transformation temperature on variant pairing of bainitic ferrite in low carbon steel, Acta Mater. 60 (2012) 2387–2396.

[90]. A. Grajcar, W. Kwaśny, W. Zalecki, Microstructure–property relationships in TRIP aided medium-C bainitic steel with lamellar retained austenite, Mater. Sci. Technol. 31 (2015) 781–794.

[91]. J. Huang, Z. Tang, H. Ding, H. Zhang, L. Bi, R. D. K. Misra, Combining a novel cyclic pre-quenching and two-stage heat treatment in a low-alloyed TRIP-aided steel to significantly enhance mechanical properties through microstructural refinement, Mater. Sci. Eng. A. 764 (2019) 138231.

[92]. V. T. Duong, Y. Y. Song, K. S. Park, H. K. D. H. Bhadeshia, D. W. Suh, Austenite in transformation-induced plasticity steel subjected to multiple isothermal heat treatments, Metall. Mater. Trans. A. 45 (2014) 4201–4209.

[93]. J. Li, F. Liu, S. Wang, J. Li, Y. Liu, Q. Meng, Effect of two-step bainite treatment on the morphology and texture of retained austenite and mechanical properties of austenitizing pretreated transformation-induced plasticity steel, Mater. Sci. Eng. A. 771 (2020) 138567.

[94]. P. J. Jacques, Q. Furnémont, F. Lani, T. Pardoen, F. Delannay, Multiscale mechanics of TRIP-assisted multiphase steels: I. Characterization and mechanical testing, Acta Mater. 55 (2007) 3681–3693.

[95]. I. B. Timokhina, A. A. Gazder, J. Wang, I. Bikmukhametov, P. D. Hodgson, F. Niessen, E. V. Pereloma, On the degradation of retained austenite in transformation induced plasticity steel, Metall. Mater. Trans. A. 51 (2020) 3802–3810.

[96]. E. Pereloma, H. Beladi, L. Zhang, I. Timokhina, Understanding the behavior of advanced high-strength steels using atom probe tomography, Metall. Mater. Trans. A. 43 (2012) 3958–3971.

[97]. N. H. Van Dijk, A. M. Butt, L. Zhao, J. Sietsma, S. E. Offerman, J. P. Wright, S. Van Der Zwaag, Thermal stability of retained austenite in TRIP steels studied by synchrotron X-ray diffraction during cooling, Acta Mater. 53 (2005) 5439–5447.

[98]. P. Xu, Y. Tomota, Y. Arakaki, S. Harjo, H. Sueyoshi, Evaluation of austenite volume fraction in TRIP steel sheets using neutron diffraction, Mater. Charact. 127 (2017) 104–110.

[99]. K. Sugimoto, T. Iida, J. Sakaguchi, T. Kashima, Retained austenite characteristics and tensile properties in a TRIP type bainitic sheet steel, ISIJ Int. 40 (2000) 902–908.

[100]. J. Kobayashi, D. Ina, N. Yoshikawa, K. Sugimoto, Effects of the addition of Cr, Mo and Ni on the microstructure and retained austenite characteristics of 0.2% C–Si–Mn–Nb ultrahigh-strength TRIP-aided bainitic ferrite steels, ISIJ Int. 52 (2012) 1894–1901.

[101]. S. Lee, S. J. Lee, B. C. De Cooman, Austenite stability of ultrafine-grained transformation-induced plasticity steel with Mn partitioning, Scr. Mater. 65 (2011) 225–228.

[102]. A. Matsuzaki, H. K. D. H. Bhadeshia, Effect of austenite grain size and bainite

morphology on overall kinetics of bainite transformation in steels, Mater. Sci. Technol. 15 (1999) 518–522.

[103]. F. G. Caballero, C. García-mateo, J. Chao, M. J. Santofimia, C. Capdevila, C. G. De Andrés, Effects of morphology and stability of retained austenite on the ductility of TRIP-aided bainitic steels, ISIJ Int. 48 (2008) 1256–1262.

[104]. Z. Xiong, A. A. Saleh, R. K. W. Marceau, A. S. Taylor, N. E. Stanford, A. G. Kostryzhev, E. V. Pereloma, Site-specific atomic-scale characterisation of retained austenite in a strip cast TRIP steel, Acta Mater. 134 (2017) 1–15.

[105]. G. Lacroix, T. Pardoen, P. J. Jacques, The fracture toughness of TRIP-assisted multiphase steels, Acta Mater. 56 (2008) 3900–3913.

[106]. N. Tsuchida, S. Okura, T. Tanaka, Y. Toji, High-speed tensile deformation behavior of 1 GPa-grade TRIP-aided multi-phase steels, ISIJ Int. 58 (2018) 978–986.

[107]. T. Yamashita, N. Koga, O. Umezawa, Influence of deformability of retained austenite on martensitic transformation in tension for low alloy steel at low temperatures, ISIJ Int. 58 (2018) 1155–1161.

[108]. W. H. Johnson, Proc. R. Soc. London 23, 168 (1875).

[109]. Z. D. Harris, S. K. Lawrence, D. L. Medlin, G. Guetard, J. T. Burns, B. P. Somerday, Elucidating the contribution of mobile hydrogen-deformation interactions to hydrogen-induced intergranular cracking in polycrystalline nickel, Acta Mater. 158 (2018) 180–192.

[110]. Y. Ogawa, K. Noguchi, O. Takakuwa, Criteria for hydrogen-assisted crack initiation in Ni-based superalloy 718, Acta Mater. 229 (2022) 117789.

[111]. H. Zhao, P. Chakraborty, D. Ponge, T. Hickel, B. Sun, C. Wu, B. Gault, D. Raabe, Hydrogen trapping and embrittlement in high-strength Al alloys, Nature. 602 (2022) 437–441.

[112]. K. Ichii, M. Koyama, C. C. Tasan, K. Tsuzaki, Comparative study of hydrogen embrittlement in stable and metastable high-entropy alloys, Scr. Mater. 150 (2018) 74–77.

[113]. I. M. Robertson, P. Sofronis, A. Nagao, M. L. Martin, S. Wang, D. W. Gross, K. E. Nygren, Hydrogen embrittlement understood, Metall. Mater. Trans. B. 46 (2015) 2323–2341.

[114]. M. Nagumo, Fundamentals of hydrogen embrittlement, Springer, New York, 2016.

[115]. A. Barnoush, H. Vehoff, Recent developments in the study of hydrogen embrittlement: Hydrogen effect on dislocation nucleation, Acta Mater. 58 (2010) 5274–5285.

[116]. Y. Matsumoto, K. Takai, Method of evaluating delayed fracture susceptibility of

tempered martensitic steel showing quasi-cleavage fracture, Metall. Mater. Trans. A. 48(2017) 666–677.

[117]. Y. Shibayama, T. Hojo, E. Akiyama, An evaluation method for hydrogen embrittlement of high strength steel sheets using U-bend specimens, ISIJ Int. 61(2021) 1104–1111.

[118]. T. Chen, T. Chiba, M. Koyama, E. Akiyama, K. Takai, Factors distinguishing hydrogen-assisted intergranular and intergranular-like fractures in a tempered lath martensitic steel, Metall. Mater. Trans. A. 53 (2022) 1645–1658.

[119]. M. Koyama, H. Springer, S. V. Merzlikin, K. Tsuzaki, E. Akiyama, D. Raabe, Hydrogen embrittlement associated with strain localization in a precipitation-hardened Fe-Mn-Al-C light weight austenitic steel, Int. J. Hydrogen Energy, 39(2014) 4634–4646.

[120]. J. Takahashi, K. Kawakami, Y. Kobayashi, Origin of hydrogen trapping site in vanadium carbide precipitation strengthening steel, Acta Mater. 153 (2018) 193–204.

[121]. S. I. Lee, J. M. Lee, S. Y. Lee, H. J. Kim, J. Y. Suh, J. H. Shim, U. B. Baek, S. H. Nahm, J. Lee, B. Hwang, Tensile and fracture behaviors of austenitic high-manganese steels subject to different hydrogen embrittlement test methods, Mater. Sci. Eng. A. 799 (2019) 138367.

[122]. Y. Zhao, J. M. Park, D. H. Lee, E. J. Song, J. Y. Suh, U. Ramamurty, J. Jang, Influences of hydrogen charging method on the hydrogen distribution and nanomechanical properties of face-centered cubic high-entropy alloy: A comparative study, Scr. Mater. 168 (2019) 76–80.

[123]. S. Takagi, Y. Toji, M. Yoshino, K. Hasegawa, Hydrogen embrittlement resistance evaluation of ultra high strength steel sheets for automobiles, ISIJ Int. 52 (2012) 316–322.

[124]. J. Venezuela, J. Blanch, A. Zulkiply, Q. Liu, Q. Zhou, M. Zhang, A. Atrensa, Further study of the hydrogen embrittlement of martensitic advanced high strength steel in simulated auto service conditions, Corros. Sci. 135 (2018) 120–135.

[125]. S. Hong, S. Y. Shin, H. S. Kim, S. Lee, S. K. Kim, K. G. Chin, N. J. Kim, Effects of inclusions on delayed fracture properties of three Twinning induced plasticity (TWIP) Steels, Metall. Mater. Trans. A. 44 (2013) 776–786.

[126]. M. Koyama, E. Akiyama, Y. K. Lee, D. Raabe, K. Tsuzaki, Overview of hydrogen embrittlement in high-Mn steels, Int. J. Hydrogen Energy, 42(2017) 12706–12723.

[127]. M. R Louthan, G. R Caskey, J. A. Donovan, D. E Rawl, Hydrogen embrittlement of metals, Mater. Sci. Eng. A. 10 (1972) 357–368.

[128]. A. Oudriss, A. Fleurentin, G. Courlit, E. Conforto, C. Berziou, C. Rébéré, S.

Cohendoz, J. M. Sobrino, J. Creus, X. Feaugas, Consequence of the diffusive hydrogen contents on tensile properties of martensitic steel during the desorption at room temperature, Mater. Sci. Eng. A. 658 (2016) 400–408.

[129]. T. Zimmerman, Brunswick RCS Leakage, 2019.

[130]. M. B. Djukic, G. M. Bakic, V. S. Zeravcic, A. Sedmak, B. Rajicic, The synergistic action and interplay of hydrogen embrittlement mechanisms in steels and iron: localized plasticity and decohesion, Eng Fract Mech, 216 (2019), 106528.

[131]. M. Nagumo, Function of hydrogen in embrittlement of high-strength steels, ISIJ Int. 41 (2001) 590–598.

[132]. W. S. Yang, J. W. Seo, S. H. Ahn, A study on hydrogen embrittlement research on automotive steel sheets, Corros. Sci. Technol. 17(2018) 193–201.

[133]. M. Koyama, E. Akiyama, K. Tsuzaki, Effect of hydrogen content on the embrittlement in a Fe-Mn-C twinning-induced plasticity steel, Corros. Sci. 59 (2012) 277–281.

[134]. M. Wang, E. Akiyama, K. Tsuzaki, Fracture criterion for hydrogen embrittlement of, high strength steel, Mater. Sci. Technol. 22 (2006) 167–172.

[135]. H. Li, J. Venezuela, Q. Zhou, Z. Shi, M. Yan, R. Knibbe, M. Zhang, F. Dong, A. Atrens, Effect of plastic strain damage on the hydrogen embrittlement of a dual-phase (DP) and a quenching and partitioning (Q&P) advanced high-strength steel, Mater. Sci. Eng. A. 785 (2020) 139343.

[136]. J. A. Ronevich, J. G. Speer, D.K. Matlock, Hydrogen embrittlement of commercially produced advanced high strength sheet steels, SAE Int. J. Mater. Manuf., 3 (2010) 255–267.

[137]. T. Michler, J. Naumann, Microstructural aspects upon hydrogen environment embrittlement of various bcc steels, Int. J. Hydrogen Energy, 35 (2010) 821–832.

[138]. C. Hao, M. Koyama, E. Akiyama, Quantitative evaluation of hydrogen effects on evolutions of deformation-induced ε-martensite and damage in a high-Mn Steel, Metall. Mater. Trans. A. 51 (2020) 6184–6194.

[139]. T. Hojo, R. Kikuchi, H. Waki, F. Nishimura, Y. Ukai, E. Akiyama, Effect of strain rate on the hydrogen embrittlement property of ultra high-strength low alloy TRIP aided steel, ISIJ Int. 58 (2018) 751–759.

[140]. C. Hao, M. Koyama, S. Ajito, E. Akiyama, Strain rate sensitivity of hydrogen-assisted ε-martensitic transformation and associated hydrogen embrittlement in high-Mn steel, Int. J. Hydrogen Energy, 46(2021) 27221–27233.

[141]. J. A. Ronevich, B. C. De Cooman, J. G. Speer, E. De Moor, D. K. Matlock, Hydrogen effects in prestrained transformation induced plasticity steel, Metall. Mater.

Trans. A. 43 (2012) 2293–2301.
[142]. M. Y. Maeda, M. Koyama, H. Nishimura, O. M. Cintho, E. Akiyama, Pre-straining alters hydrogen-assisted cracking site and local hydrogen diffusivity in a nitrogen-doped duplex steel, Scr. Mater. 207 (2022) 114272.
[143]. V. K. Verma, M. Koyama, B. Kumai, T. Hojo, E. Akiyama, Roles of hydrogen content and pre-strain on damage evolution of TRIP-aided bainitic ferrite steel, ISIJ Int. 61 (2021) 1309–1314.
[144]. R. A. Oriani, The diffusion and trapping of hydrogen in steel, Acta Metall. 18 (1970) 147–157.
[145]. Q. Liu, J. Venezuela, Mi. Zhang, Q. Zhou, A, Atrens, Hydrogen trapping in some advanced high strength steels, Corros. Sci. 111 (2016) 770–785.
[146]. T. Chen, T. Chiba, M. Koyama, A. Shibata, E. Akiyama, K. Takai, Hierarchical characteristics of hydrogen-assisted crack growth and microstructural strain evolution in tempered martensitic steels: case of quasi-cleavage fracture, Metall. Mater. Trans. A. 47 (2021) 718–725.
[147]. M. Wang, E. Akiyama, K. Tsuzaki, Determination of the critical hydrogen concentration for delayed fracture of high strength steel by constant load test and numerical calculation, Corros. Sci. 48 (2006) 2189–2202.
[148]. J. Song, W. A. Curtin, A nanoscale mechanism of hydrogen embrittlement in metals, Acta Mater. 59 (2011) 1557–1569.
[149]. Y. Chen, D. Chen, M. Chiang, G. Cheng, H. Lin, H. Yen, Response of hydrogen desorption and hydrogen embrittlement to precipitation of nanometer-sized copper in tempered martensitic low-carbon steel, JOM. 71(2019) 1349–1356.
[150]. H. J. Seo, Y. Heo, J. N. Kima, J. Lee, S. Choi, C. S. Lee, Effect of V/Mo ratio on the evolution of carbide precipitates and hydrogen embrittlement of tempered martensitic steel, Corros. Sci. 176 (2020) 108929.
[151]. R. Oriani, B. Ges. Phys. Chem. 76, 848 (1972)
[152]. N. N. Sergeev, A. N. Sergeev, S. N. Kutepov, A. G. Kolmakov, and A. E. Gvozdev, Mechanism of the hydrogen cracking of metals and alloys, Part II (review), Inorganic Materials: Applied Research. 10 (2019) 32–41.
[153]. S. P. Lynch, Hydrogen embrittlement phenomena and mechanisms, Corrosion Rev, 30 (2012). 105-123
[154]. S. K. Dwivedi, M. Vishwakarma, Effect of hydrogen in advanced high strength steel materials, Int. J. Hydrogen Energy, 44(2019) 28007–28030.
[155]. H. K. Birnbaum, P. Sofronis, Hydrogen-enhanced localized plasticity-a mechanism for hydrogen-related fracture, Mater. Sci. Eng. A. 176 (1994) 191–202.

[156]. M. L. Martin, M. Dadfarnia, A. Nagao, S. Wang, P. Sofronis, Enumeration of the hydrogen-enhanced localized plasticity mechanism for hydrogen embrittlement in structural materials, Acta Mater. 165 (2019) 734–750.

[157]. A. Nagao, M. Dadfarnia, B. P. Somerday, P. Sofronis, R. O. Ritchie, Hydrogen-enhanced-plasticity mediate d decohesion for hydrogen-induced intergranular and "quasi-cleavage" fracture of lath martensitic steels, J. Mech. Phys. Solids, 112(2018) 403–430.

[158]. M. L. Martin, I. M. Robertson, P. Sofronis, Interpreting hydrogen-induced fracture surfaces in terms of deformation processes: A new approach, Acta Mater. 59 (2011) 3680–3687.

[159]. M. Nagumo, K. Takai, The predominant role of strain-induced vacancies in hydrogen embrittlement of steels: Overview, Acta Mater. 165 (2019) 722–733.

[160]. M. Hatano, M. Fujinami, K. Arai, H. Fujii, M. Nagumo, Hydrogen embrittlement of austenitic stainless steels revealed by deformation microstructures and strain-induced creation of vacancies, Acta Mater. 67 (2014) 342–353.

Chapter 2: Materials and experimental procedure

2 Materials and experimental procedure

2.1 Materials and experiment

2.1.1 Preparation of materials

A low-alloy steel with a nominal composition of Fe–1.5Mn–1.5Si–0.4C (wt.%) was selected, and its detailed chemical composition is listed in Table 2-1. 1.5% Si was considered to be sufficient to suppress the formation of cementite during thermal processing. 1.5% Mn was employed to function as an austenite stabilizer and solid solution strengthen, and 0.4% C can make the more stability of austenite at room temperature. The steels used in the present study was melted in a vacuum induction furnace. After reheating at 1200 ℃ for 1 h, the ingot was hot rolled to a thickness of 3.2 mm at a finishing temperature of 850 ℃, followed by air cooling to room temperature. Thereafter, the hot-rolled plate was further cold-rolled to a thickness of 1.2 mm. A schematic drawing of the hot and cold rolling processes is shown in Figure. 2-1.

Table 2-1. Chemical composition of the present study (in mass%).

C	Si	Mn	Al	P	S	N
0.39	1.47	1.50	0.04	0.014	0.0012	0.0008

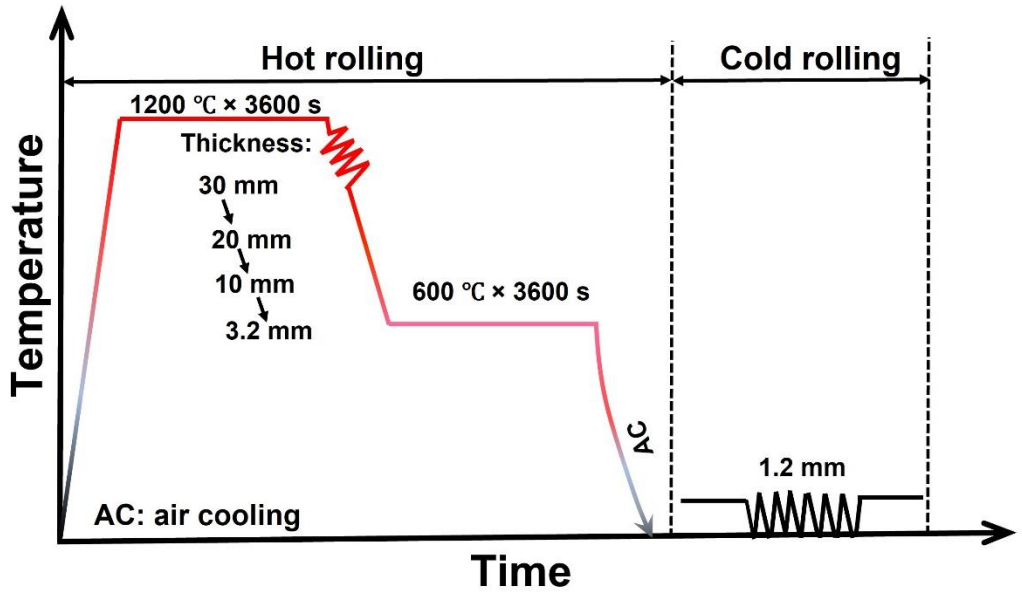

Figure. 2-1 Schematic of hot rolling and cold-rolling processes in this study.

2.1.2 Hydrogen charging methods

The tensile specimen surfaces were mechanically polished using abrasive papers and electrolytically polished in a solution of 20% perchloric acid and 80% acetic acid at 20 V for 120 s before hydrogen charging. The final thickness of the specimen was ~0.95 mm. Electrochemical hydrogen charging to the hydrogen-charging specimens was performed in a 3% NaCl aqueous solution containing 3 g/L NH_4SCN at a constant current density of 10 A/m^2 for 48 h before tensile tests. A platinum wire was used as the counter electrode, as shown in Figure. 2-2. In the hydrogen charging condition, neither blisters nor macro-cracks on the surface of the samples were observed.

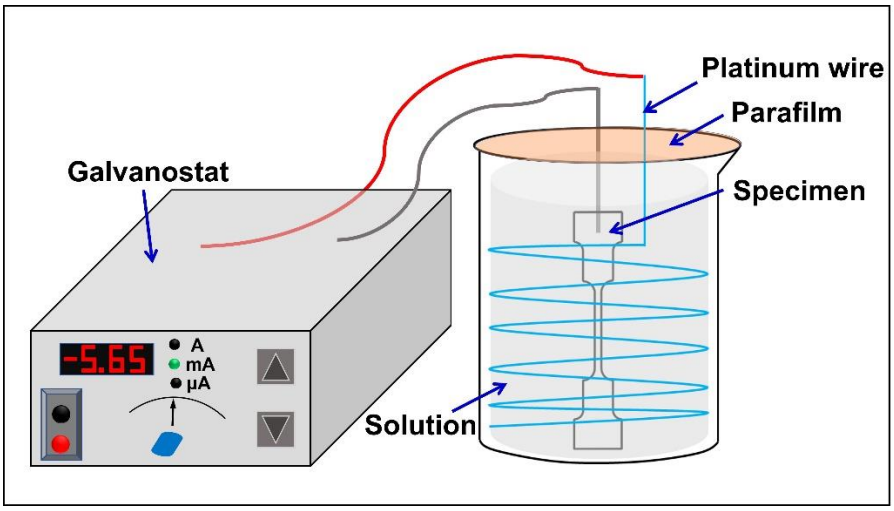

Figure. 2-2 Schematic of hydrogen-charging method.

2.1.3 Tensile tests

For the tensile test in Chapter 3, dog-bone-shaped tensile specimens with a gauge length of 25 mm, a gauge width of 6 mm, and a thickness of 1.2 mm were machined along the rolling direction of the cold-rolled sheets and were tensile tested at 21 ℃ at a strain rate of 1×10^{-4} s^{-1} using Shimadzu tensile testing machine. Figure. 2-3 shows the detailed tensile specimens geometry size.

For the tensile test in Chapter 4 and Chapter 5, SSRT tests were performed on a tensile testing machine equipped with a thermostatic chamber at an initial strain rate of 1×10^{-4} s^{-1} at different deformation temperatures of -100, -30, 21, and 100 °C, as shown in Figure. 2-4.

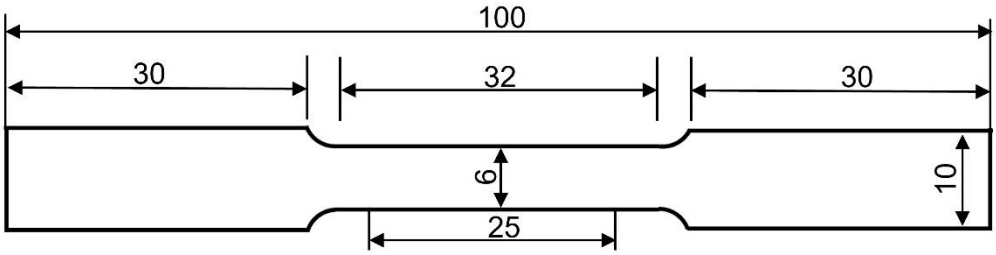

Figure. 2-3 Specimen dimensions for tensile testing (unit: mm).

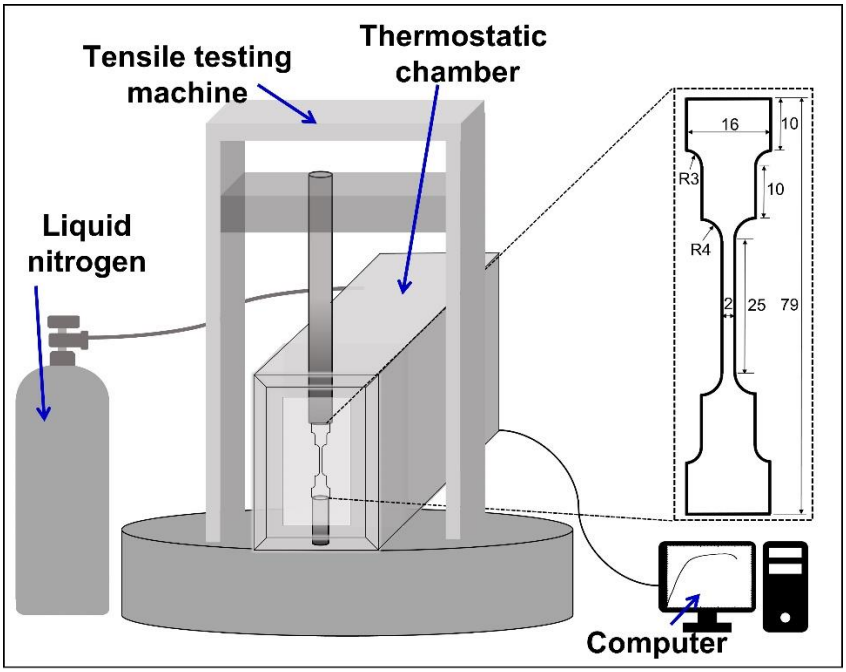

Figure. 2-4 Configuration of tensile testing apparatus (unit: mm).

2.2 Characterization methods

2.2.1 X-ray diffraction

The volume fractions of retained austenite before and after tensile deformation were determined by XRD with CuKα radiation using integrated intensities of the $(200)_\alpha$, $(211)_\alpha$, $(200)_\gamma$, $(220)_\gamma$, and $(311)_\gamma$ peaks. The average carbon concentration in retained austenite (C_γ) was calculated using equation (2-1) [1]:

$$a_\gamma = 3.5780 + 0.0330C_\gamma + 0.00095Mn_\gamma + 0.0056Al_\gamma + 0.0220N_\gamma \quad (2\text{-}1)$$

where Mn_γ, Al_γ, and N_γ are the Mn, Al, and N concentrations in austenite, which are considered to be the corresponding average concentrations of the alloy, respectively; a_γ is the lattice parameter of austenite.

The peak fitting of each diffraction peak was conducted using HighScore software

which was attached to the XRD equipment. The measurement was performed at least two times to reduce error.

2.2.2 Scanning electron microscopy

The microstructure of the heat-treated steels was characterized by SEM and EBSD. The specimens were first mechanically ground with #320 and #600 waterproof SiC papers, polished by 9 and 3 μm diamond slurries, and chemically polished using colloidal silica. EBSD analyses were performed at an accelerating voltage of 20 kV with a working distance of 15 mm and a step size of 50 or 100 nm. The acquired EBSD was analyzed using the TSL OIM software package.

ECCI has been proven as an excellent SEM technique based on the strong dependence of the backscatter electron intensity on the orientation of crystal lattice planes with respect to the incident electron beam due to the electron channeling mechanism [2, 3]. Compared to transmission electron microscopy, less artefacts and much larger observation area can be obtained by ECCI. ECCI has been proved to be successful in observation of microstructures. Thus, it is a powerful and well-suited technique to study the effect of hydrogen on microstructure in a detailed and statistically meaningful way. In this study, the ECCI was performed at 30 kV acceleration voltage with working distance of approximately 5 mm by using the same SEM facility equipped with a solid state four-quadrant backscatter electron detector.

2.2.3 Thermal desorption spectroscopy

Hydrogen-charged specimens after the tensile tests were kept in liquid nitrogen until the TDS analysis. Figure. 2-5 shows a schematic illustration of the typical set-up for the thermal desorption analysis with gas chromatography. When the charged specimen is heated in the furnace, the trapped hydrogen starts to evolve. The desorbed hydrogen moves into the gas chromatograph with the aid of a carrier gas He. Then the amount of desorbed hydrogen is monitored by a detector [4].

The hydrogen desorption behavior was analyzed using TDS. The specimens were heated from room temperature to 800 °C at a heating rate of 100 °C/h. The diffusible hydrogen content was defined as the total amount of desorbed hydrogen in the temperature range from ambient temperature to 300 ℃.

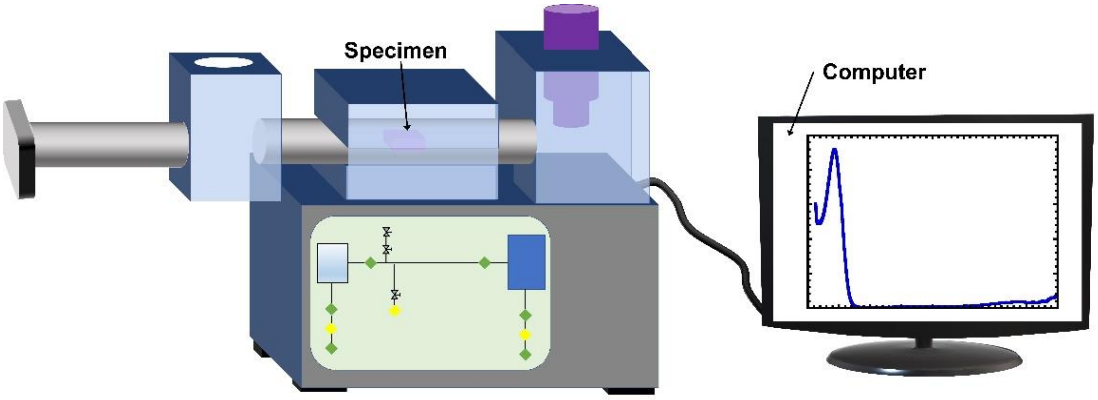

Figure. 2-5 Configuration of thermal desorption spectroscopy.

2.3 References

[1]. T. Hojo, R. Kikuchi, H. Waki, F. Nishimura, Y. Ukai, E. Akiyama, Effect of strain rate on the hydrogen embrittlement property of ultra high-strength low alloy TRIP aided steel, ISIJ Int. 58 (2018) 751–759.

[2]. M. Koyama, E. Akiyama, K. Tsuzaki, D. Raabe, Hydrogen-assisted failure in a twinning-induced plasticity steel studied under in situ hydrogen charging by electron channeling contrast imaging, Acta Mater. 61 (2013) 4607–4618.

[3]. S. Zaefferer, N. N. Elhami, Theory and application of electron channelling contrast imaging under controlled diffraction conditions, Acta Mater. 75 (2014) 20–50.

[4]. F. J. Castroa, G. Meyer, Thermal desorption spectroscopy (TDS) method for hydrogen desorption characterization (I): theoretical aspects, J. Alloy. Compd. 330 (2002) 59–63.

Chapter 3: Effect of austempering treatment on the microstructure and mechanical properties of TRIP-aided bainitic ferrite steel

3 Effect of austempering treatment on the microstructure and mechanical properties of TRIP-aided bainitic ferrite steel

3.1 Introduction

As mentioned in Chapter 1, AHSSs with a good combination of specific strength and ductility are required to achieve weight reduction and enhance crash safety [1–3]. In this context, TRIP-aided steels with multiphase microstructures and low alloying designs have attracted significant attention not only because of their outstanding mechanical performance but also because of their relatively low production costs [4–6]. Most previous studies on TRIP-aided steels involved heat-treatment processes to obtain different matrix structures and mechanical properties [7, 8]. Conventional TRIP-aided steel consisting of polygonal ferrite, bainite, and blocky retained austenite can be produced by intercritical annealing followed by austempering treatment to achieve strengths of 600–1000 MPa with an elongation greater than 15% [9–17]. Unfortunately, limitations related to strengthening and their relatively low stretch-flangeability or bendability hinder the further industrial application of conventional TRIP-aided steels for automobile structural components [18]. Therefore, the concept of a carbide-free bainite matrix has been adopted for low-carbon low-alloy TRIP-aided steels, which are produced by annealing in the austenite region followed by isothermal bainitic transformation. These low-carbon low-alloy TRIP-aided steels mainly consist of a bainitic ferrite lath matrix with a high dislocation density and a relatively stable retained austenite film and are referred to as TRIP-assisted bainitic ferritic (TBF) steels. Such TBF steels are considered the most effective way to increase the strength and stretch-flangeability of TRIP-aided steels [19].

In addition, previous research on TBF steels has focused on the effects of isothermal transformation temperature [20, 21], alloying composition [22–24], and the stability of retained austenite [25, 26] on mechanical properties. Extensive investigation suggests that the carbon content of 0.4% in the TBF steels achieves excellent mechanical properties for industrial applications. Moreover, bainite transformation kinetics and carbon partitioning of retained austenite during isothermal transformation treatment were systematically investigated by Furuhara et al. [27]. The detailed investigations of the effect of the retained austenite characteristics on the tensile fracture behavior in the 0.4% C-bearing TBF steels are also needed. Meanwhile, although some researchers have proposed that a multi-step bainitic transformation treatment can potentially improve the strength of some steels via ultra-grain refinement of the bainitic microstructure and TRIP effect [28]. For

example, Kim et al. 29] obtained two retained austenite morphologies through double bainitic transformation and found that film-type retained austenite improved the tensile properties. Further studies on deformation mechanisms and fracture morphologies in 0.4% C-bearing TBF steels with respect to austempering time are required to design next-generation TBF steels. In this study, the effects of volume fraction and carbon concentration of retained austenite which were changed by the austempering time on the mechanical properties and tensile fracture morphologies of 0.4% C-bearing TBF steels were systematically investigated, and the corresponding fracture mechanisms were proposed.

3.2 Experimental procedure

The cold-rolled steel sheets were subjected to different heat treatments. Annealing and austempering treatments were performed in two salt baths as follows. According to the following equations [30], the bainite transformation start temperature (B_s) and M_s of the steel sheet were estimated to be 470 ℃, and 350 ℃, respectively. Therefore, the austemerping temperature in this study was chosen to 400 ℃. The specimens were first austenitized at 900 ℃ for 1200 s followed by austempering at 400 ℃ for 0, 100, 200, 500, 1000, and 3600 s. Subsequently, the samples were oil-quenched to room temperature. A schematic of the heat-treatment process is shown in Figure. 3-1.

$$B_s\ (℃) = 656 - 57.7C - 35Mn - 75Si \quad (3\text{-}1)$$

$$M_s\ (℃) = 550 - 361C - 39Mn - 0Si + 30Al - 5Mo \quad (3\text{-}2)$$

The microstructure of the heat-treated steels was characterized by SEM and EBSD. The samples were etched with 5% nital for about 10 s before SEM observation. The volume fractions of retained austenite before and after tensile deformation were determined by XRD.

The tensile tests were performed using Shimadzu tensile machine. 0.2% proof stress was determined to be the YS in the specimens, and elongation was calculated by measuring the length of the gauge part before and after tensile tests. In addition, the behavior of the voids and cracks in the cross-sectional area near the fracture region was observed using SEM and EBSD. The mean crack length and void density, defined as the number of observed voids divided by the observed area, were quantitatively measured from the SEM images. The observed area was composed of some SEM images that were randomly captured near the fracture region of approximately 1 mm to reduce statistical errors, and crack length was determined by the linear intercept method. Note that the maximum crack length was not considered in the statistical analysis of mean crack length. The surfaces of the tensile-fractured specimens were also observed by SEM.

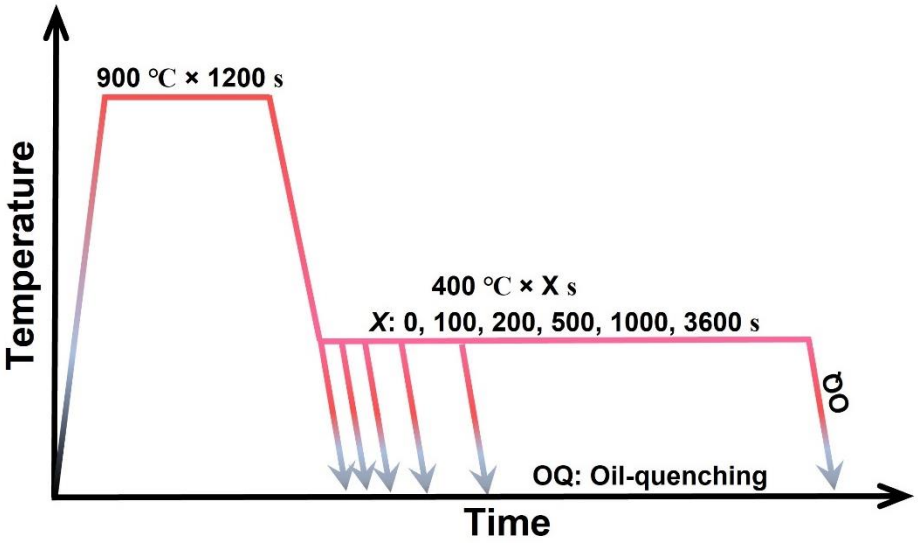

Figure. 3-1 Schematic diagram of annealing and austempering treatment processes.

3.3 Results

3.3.1 Microstructure

Figure. 3-2 shows the microstructures of the specimens after heat treatment at different austempering times. The microstructure of the specimen without austempering mainly consisted of lath martensite or martensite/austenite (M/A) constituents (Figure. 3-2(a)). However, it was difficult to distinguish martensite and M/A constituents in this SEM microstructures. Subsequent au tempering at 400 ℃ for 100 s considerably decreased the martensite or M/A constituents fractions and formed a lath-like bainitic ferrite (BF) matrix (Figure. 3-2(b)). Although retained austenite remains during austempering, it could not be identified by SEM. The prior austenite grain size was calculated to be approximately 27 μm using the mean linear intercept method. With an increase in the austempering time from 100 to 1000 s, the bainitic ferrite increased. When the specimen was austempered for 3600 s, the fraction of bainitic ferrite/bainite slightly increased and a small amount of martensite could be noted in the specimen (Figure. 3-2(f)). In addition, it was observed that a larger number of carbide particles precipitated in the sample at an austempering time of 3600 s when compared to other specimens.

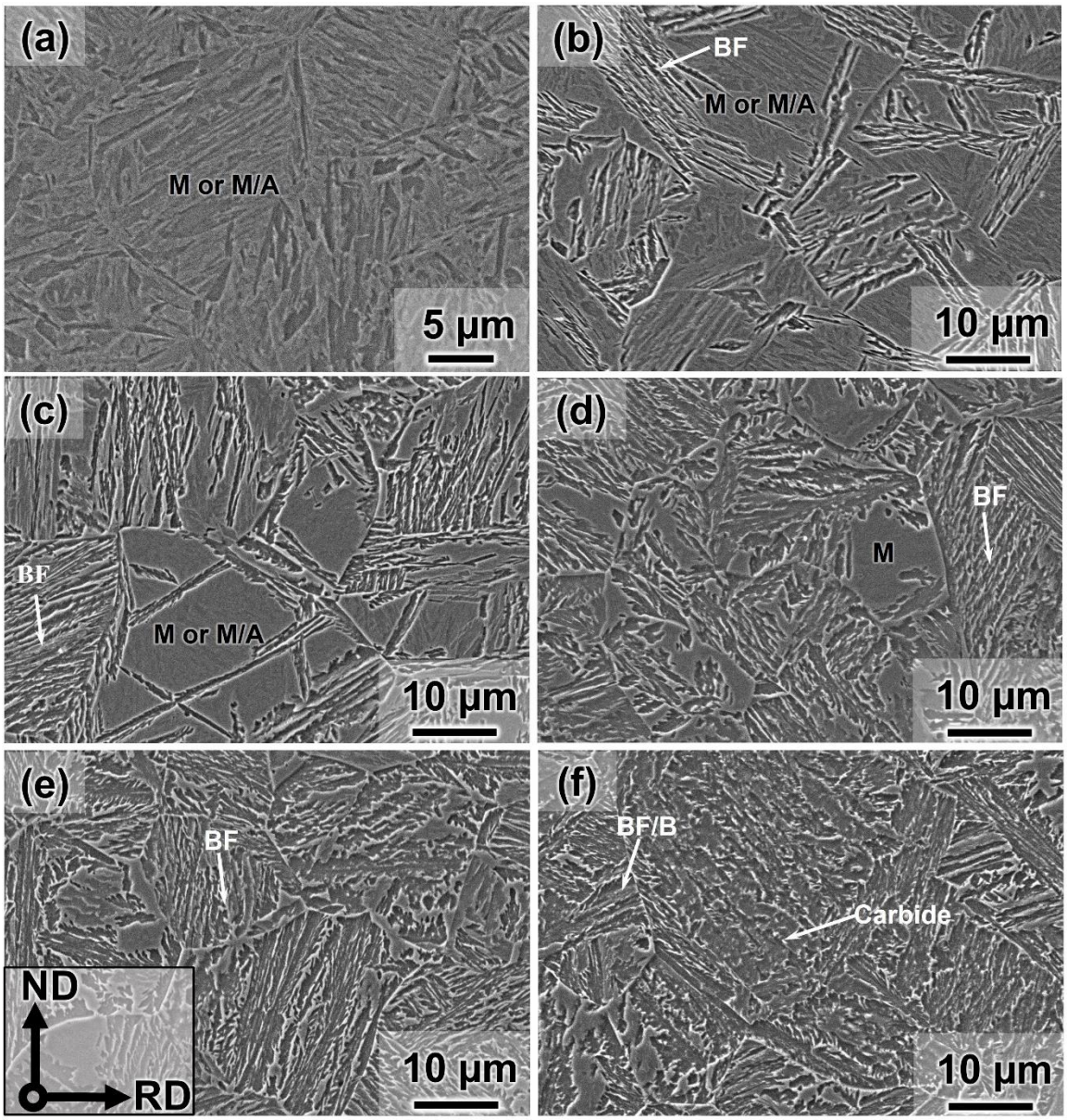

Figure. 3-2 SEM images of specimens subjected to austempering for (a) 0, (b) 100, (c) 200, (d) 500, (e) 1000, and (f) 3600 s. ND and RD represent normal direction and rolling direction, respectively. M, M/A, BF and B represent martensite, martensite/austenite constituents, bainitic ferrite and bainite, respectively.

To clarify the details of retained austenite in TBF steels, phase, IPF, and kernel average misorientation (KAM) maps are shown in Figure. 3-3 and Figure. 3-4. In the phase maps, the BCC phase represents bainitic ferrite/bainite and martensite whereas the FCC phase represents retained austenite. The microstructure of the specimen subjected to no austempering treatment consisted of martensite as the matrix with a small fraction of film-type retained austenite (RA_F) located at the block boundaries. Meanwhile, the KAM map in Figure. 3-3(a3) shows misorientations in the local lath martensite regions. In some

regions of the mixture of austenite and martensite, there was a large misorientation, as shown in the KAM map, which indicates that the mixture microstructure was M/A constituents [31]. In other words, at an austempering times of 100 and 200 s, the microstructures consisted of a mixture of bainitic ferrite, martensite, or M/A constituents and retained austenite. Moreover, the amount of retained austenite increased with an increase in austempering time. Note that the retained austenite exhibited both RA_F and block-type (RA_B) morphologies in the TBF steels austempered for 200 s. RA_F was mainly located near the bainitic ferrite packet boundaries and between bainitic ferrite back boundaries whereas RA_B was surrounded by prior austenite grain boundaries.

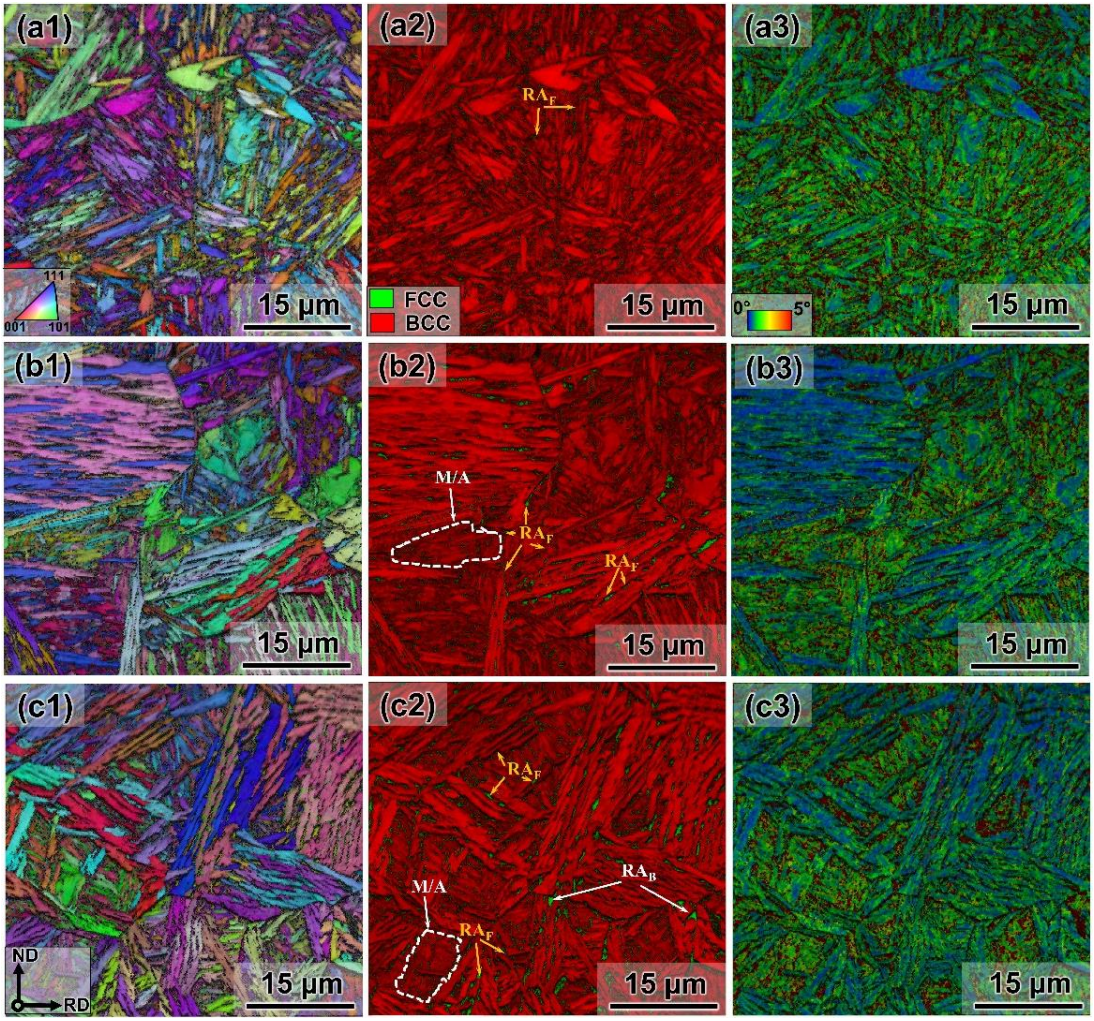

Figure. 3-3 EBSD analysis of TBF steels austempered for (a1)–(a3) 0, (b1)–(b3) 100, and (c1)–(c3) 200 s (a1), (a1, b1, c1) show IPFmaps with image quality (IQ); (a2, b2, c2) represent phase maps with IQ; (a3, b3, c3) show KAM maps with IQ. M/A, RA_F, and RA_B represent martensite/austenite constituents, film-type retained austenite and block-type retained austenite, respectively.

Figure. 3-4 shows the EBSD results of TBF steels austempered for 500, 1000, and

3600 s. When compared to the specimens austempered for 0–200 s, in the specimen austempered for 500 s, the size and amount of RA_B increased significantly, the M/A constituents disappeared, and the lath structures of bainitic ferrite were coarser (Figure. 3-4(a1)). When the austempering time was further increased to 1000 s, retained austenite was more homogenously distributed and RA_B was mainly located at the packet and prior austenite grain boundaries. However, the amount of RA_B in the 1000 s-austempered specimen was smaller than that in the 500 s-austempered specimen. Moreover, the local orientation gradients in the bainitic ferrite matrix were smaller than those in the martensite matrix (Figure. 3-4(b3)). At an austempering time of 3600 s, the amount of retained austenite decreased significantly when compared to the other specimens.

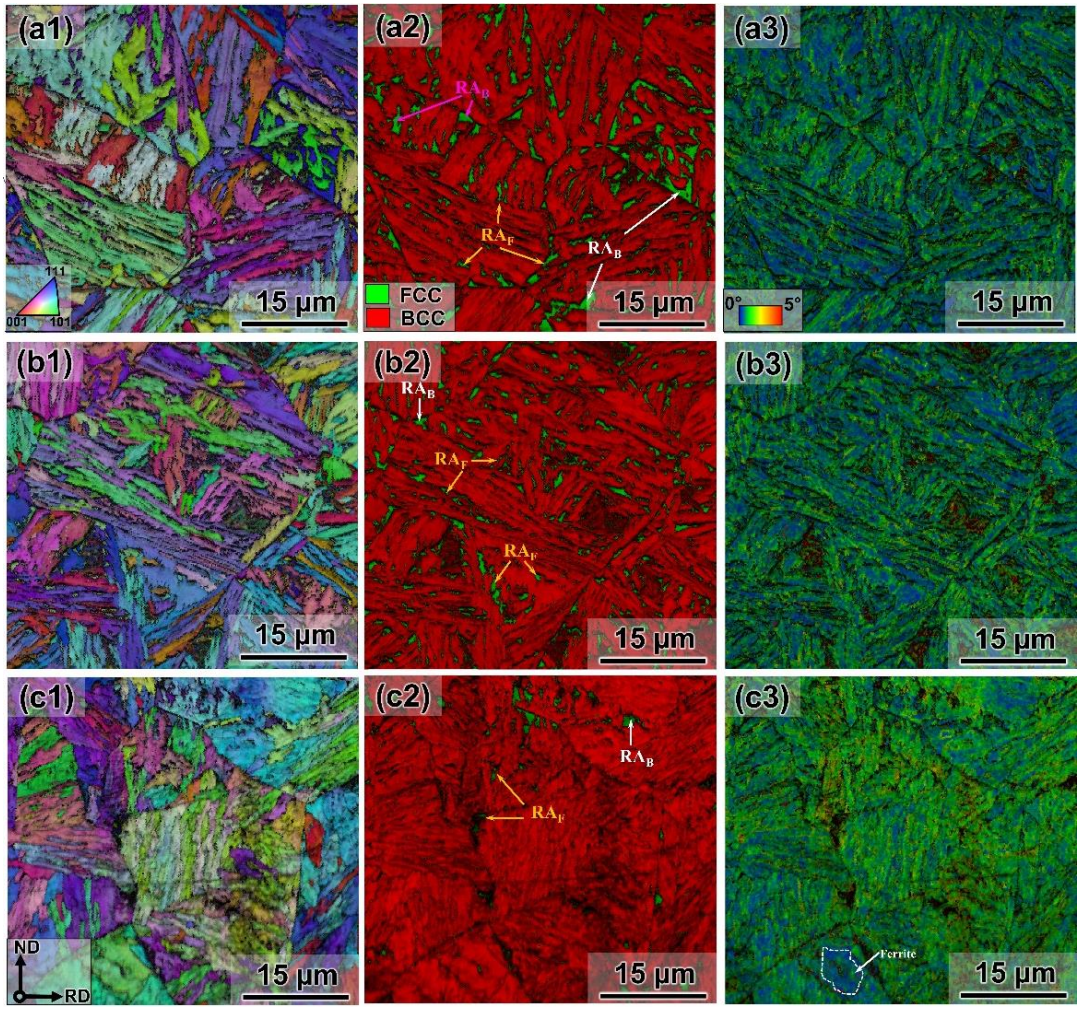

Figure. 3-4 EBSD analysis of TBF steels austempered for (a1)–(a3) 500, (b1)–(b3) 1000, and (c1)–(c3) 3600 s.

XRD patterns of as-heat-treated TBF steels, the volume fraction of retained austenite, carbon concentration in retained austenite, and total carbon content in retained austenite

in the heat-treated specimens are shown in Figure. 3-5. As the austempering time increased, the volume fraction of retained austenite of the TBF steel austempered at 0–1000 s increased from 2.1 to around 12 vol% (hereafter %), followed by a decrease to 4.8% in the TBF steel austempered for 3600 s. Meanwhile, the carbon concentration in retained austenite increased and then gradually decreased to 1.22% at austempering for 3600 s.

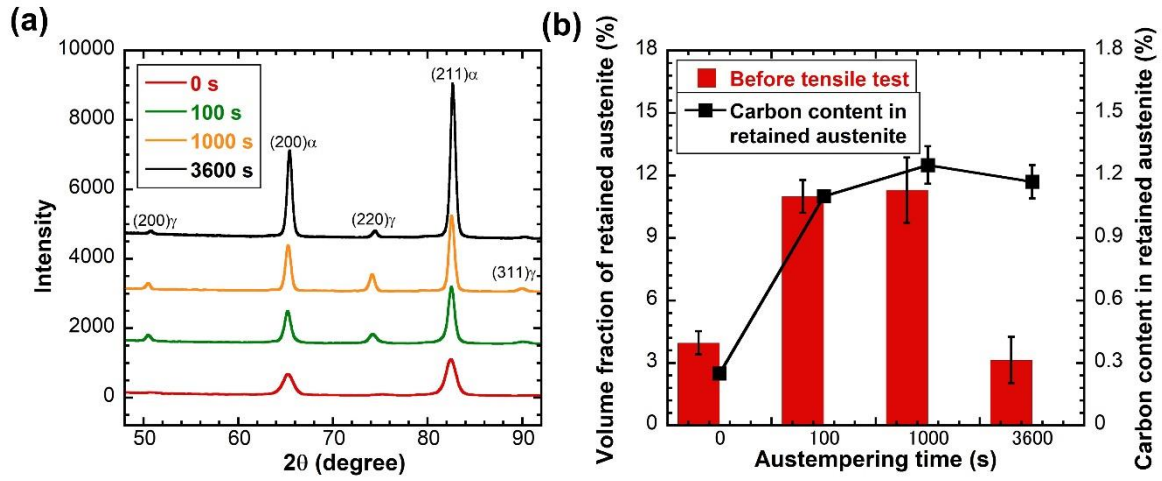

Figure. 3-5 (a) XRD patterns, (b) initial volume fraction of retained austenite and its carbon concentration.

3.3.2 Mechanical properties

The tensile properties of TBF steels austempered for different times are shown in Figure. 3-6. As shown in Figure. 3-6(a), all the specimens exhibited continuous yielding and high strength of more than 1180 MPa. In the 0 and 100 s-austempered specimens, the YS and ultimate tensile strength (UTS) were 1640 and 980 MPa and 1695 and 1730 MPa, respectively, while the uniform elongation (UEl) and total elongation (TEl) were 0.5% and 8.5% and 3.6% and 10.8%, respectively. The UTS decreased while the TEl and the product of strength and elongation (UTS × TEl) increased upon further increasing the austempering time to 1000 s; however, YS remained fairly constant. When austempering treatment was conducted for 3600 s, YS and UTS slightly increased, while TEl and (UTS × TEl) decreased as compared to the 1000 s specimen. The reduction in area corresponding to local elongation increased with increasing austempering time for 1000 s, and then decreased for 3600 s. Figure. 3-6(d) shows the work-hardening rate curves of the TBF steels. Based on the difference in slope, these curves could be divided into three stages, viz. work-hardening rate oscillating in the early stages of straining, a region in which work-hardening decreased remarkably, and a region in which the work-hardening

rate slowly decreased at high strain region until necking. In comparison, the sample austempered at 400 ℃ for 1000 s exhibited a higher work-hardening rate in the high strain region. Therefore, it is noteworthy that the TBF steel austempered for 1000 s showed excellent mechanical properties with a YS of 960 MPa, UTS of 1182 MPa, UEl of 19.8%, and TEl of 23.5%; these properties are equivalent to those of Q&P steels with a martensite matrix [32].

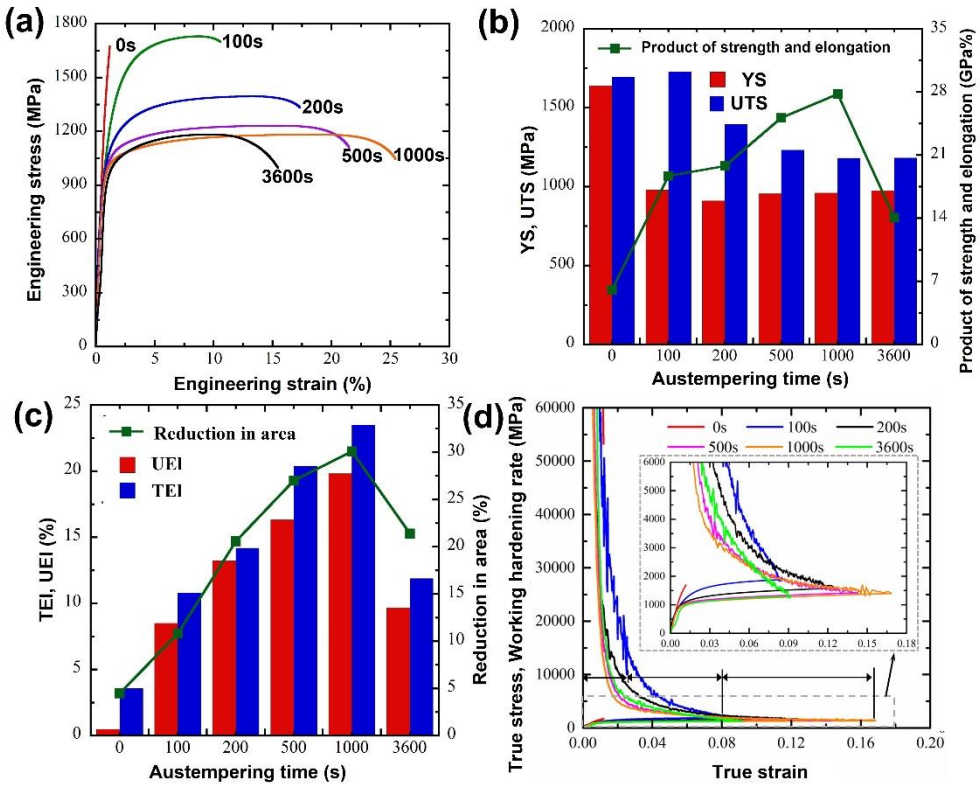

Figure. 3-6 (a) Engineering stress-strain curves, (b) UTS, YS and strength-elongation balance, (c) TEl and UEl and reduction in area and (d) work-hardening rates with true stress-strain curves.

XRD patterns after tensile test and the volume fraction of retained austenite after tensile tests are shown in Figure. 3-7. It can be seen that the volume fraction of retained austenite in the samples austempered for 0–3600 s was significantly reduced after tensile testing.

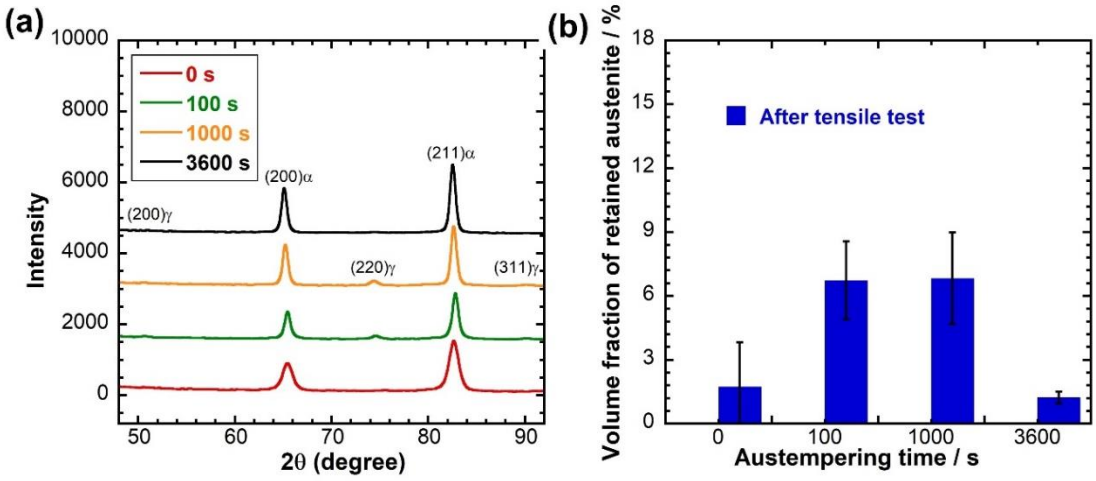

Figure. 3-7 (a) XRD patterns and (b) volume fraction of retained austenite.

3.3.3 Fracture behavior

The deformation microstructures and damage morphologies underneath the tensile fracture surfaces of specimens austempered for different times are presented in Figure. 3-8. The tensile direction of these specimens is parallel to the rolling direction. Relatively clear microstructural damages, such as cracks and voids, could be observed in the TBF steels austempered for 0–3600 s and the fractured specimens exhibited macroscopically localized necking, as shown in Figure. 3-8(a)–(f). In particular, in the 500 and 1000 s-austempered specimens, fracture occurred along a direction toward 45° with respect to the tensile direction due to shear fracture. Two types of crack propagation, viz. parallel (longitudinal) and perpendicular (transverse) to the tensile direction, were observed. In the specimen austempered for 0 s, longitudinal cracks larger than 400 μm originated near the fracture region. Meanwhile, secondary cracks were observed at the grain boundaries of martensite (Figure. 3-8(a1)). It is to be noted that the grain boundary triple junctions were also preferential crack initiation sites, as shown in Figure. 3-8(a2). The longitudinal crack initiation sites in the 100 and 200 s-austempered samples were located near the martensite and/or M/A constituents/ bainitic ferrite interfaces. The initiated cracks then propagated along the M/A constituents/bainitic ferrite interface and then coalesced with other cracks (Figure. 3-8(b1) and (c1)). However, the longitudinal cracks were blunted because there was no driving force for their propagation in this direction. Furthermore, voids and transverse cracks were nucleated inside martensite, as marked in Figure. 3-8(b2) and (c2). As the austempering time increased, the longitudinal crack length of the samples decreased (Figure. 3-8(d1) and (e1)). Voids formed inside the matrix and bainitic ferrite/martensite interfaces did not grow drastically, but large voids were observed due

to transverse crack blunting in TBF steels austempered for 500 and 1000 s (Figure. 3-8(d2) and (e2)). In the steel austempered for 3600 s, the longitudinal crack was short, and voids were initiated at the bainitic ferrite/bainite lath boundaries. A similar phenomenon was observed in the 500 and 1000 s-austempered steels as well. The measured mean crack lengths and void densities in different TBF steels are summarized in Figure. 3-9. Meanwhile, the relationship between distance from fracture surface and the reduction in thickness which corresponds to the strain is shown in Table 3-1. As the austempering time increased from 0 to 3600 s, void density initially increased and then decreased slightly, and the mean crack length decreased from 29.1 to 10.2 μm and then slightly increased to 13.4 μm.

Table 3-1. Damage observation area and reduction in thickness of specimens.

Austempering time /s	Distance from fracture surface /μm	Reduction in thickness /(%)
0	362±270	2.36±0.98
100	363±270	4.31±1.19
200	365±277	6.41±0.84
500	365±263	9.49±1.16
1000	391±293	10.71±1.13
3600	398±294	5.39±1.57

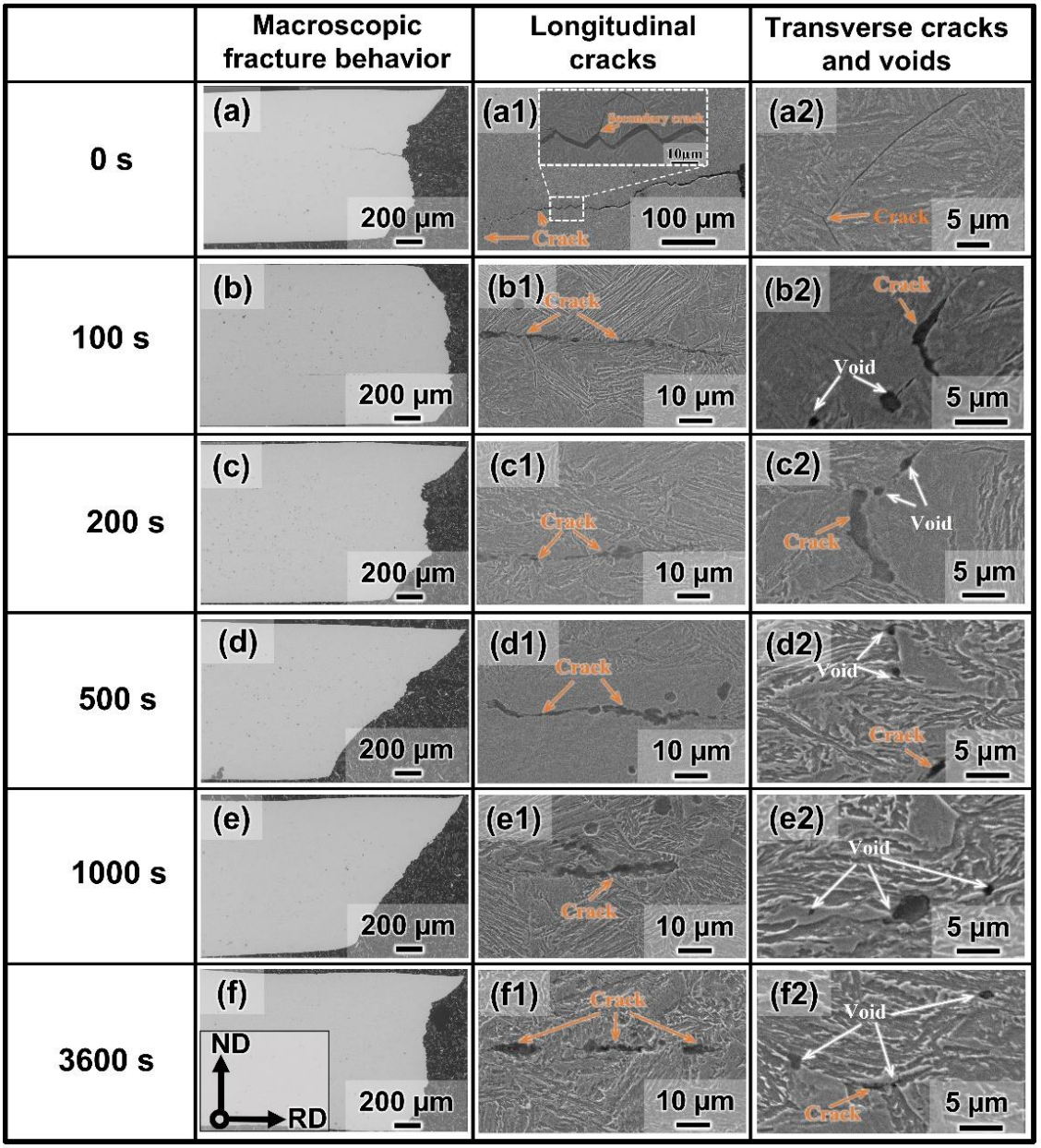

Figure. 3-8 SEM images of deformation microstructures underneath the tensile fracture surfaces of TBF steels austempered for (a) 0, (b) 100, (c) 200, (d) 500, (e) 1000 and (f) 3600 s.

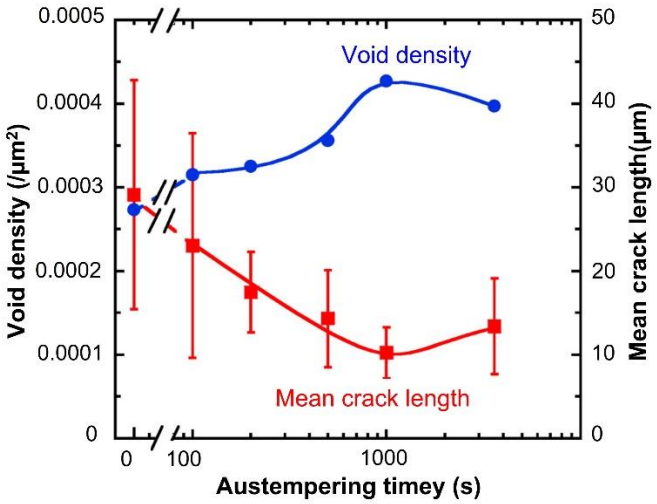

Figure. 3-9 Variation in the void density and mean crack length of TBF steels with respect to austempering time.

In order to discuss the reasons for the observed fracture behavior, EBSD analysis was conducted on the cross sections of fractured tensile specimens, as shown in Figures. 3-10 through Figures. 3-13. Crack initiation and propagation were observed in the TBF steel austempered for 0 s at the prior austenite grain boundaries and transgranular cracks terminated in martensite, as shown in Figure. 3-10. The branching crack or secondary crack was also observed along the prior austenite grain boundaries as indicated the black arrows (Figure. 3-13(a)). In the TBF steels austempered for 100 s, most of the cracks were initiated from the grain interior due to crack coalescence, resulting in the formation of transgranular cracks (Figure. 3-11(c)).

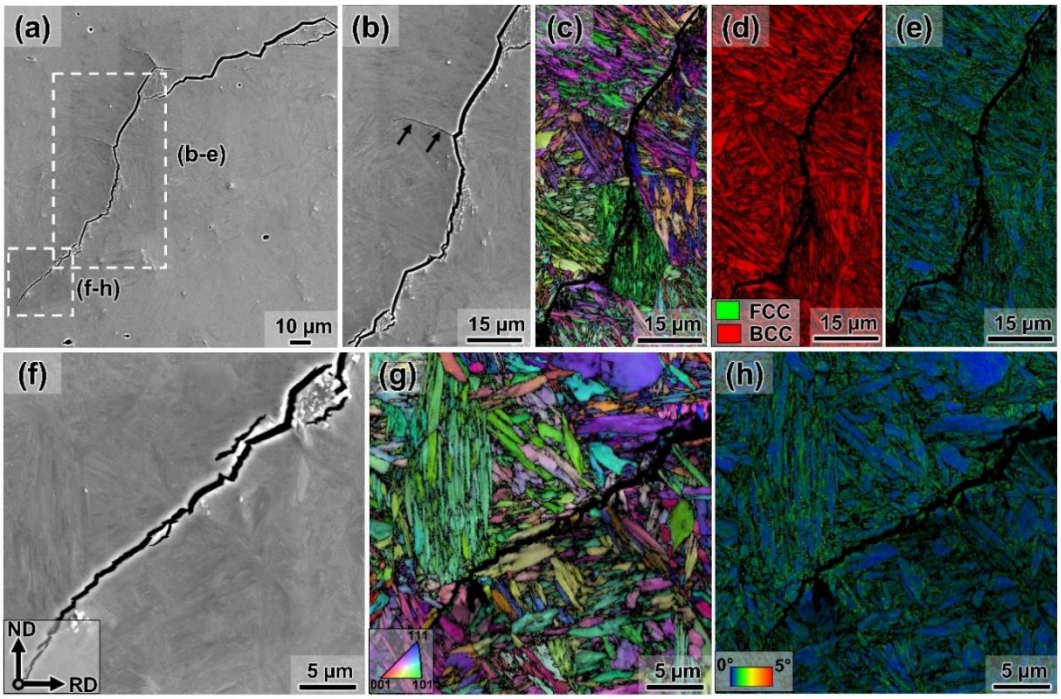

Figure. 3-10 SEM images and corresponding EBSD analysis of the cross-sectional area beneath the fracture surfaces of austempered time of 0 s. (a, b, f) SEM images, (c, g) IPF map with IQ, (d) phase map with IQ, and (e, h) KAM map with IQ.

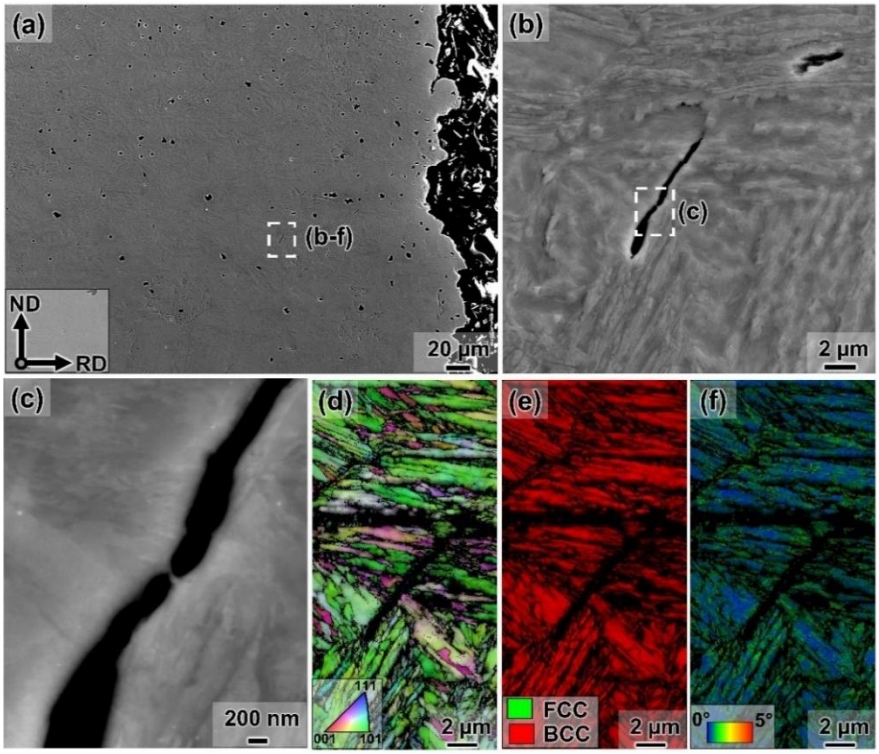

Figure. 3-11 SEM images and corresponding EBSD analysis of the cross-sectional area beneath the fracture surfaces of austempered time of 100 s. (a, b, c) SEM images, (d) IPF map with IQ, (e) phase map with IQ, and (f) KAM map with IQ.

Figure. 3-12 and Figure. 3-13 show the deformation microstructure and cracks in TBF steels austempering time of 1000 and 3600 s. In both these specimens, transgranular cracks could be observed. It is noteworthy that the EBSD images of the TBF steel austempered for 1000 s were lower image quality and included darker regions when compared to other TBF steels, indicating that the microstructure had undergone serious deformation and lattice distortion. In addition, almost all the retained austenite transformed into martensite during tensile deformation (Figure. 3-12(b)). Small voids appeared in the TBF steel austempered for 1000 s; in the 3600 s-austempered specimen, the crack tip underwent blunting and cracks propagated along bainitic ferrite/bainite lath boundaries and coalesced with other cracks in the longitudinal direction, as shown in Figure. 3-13(f). These observations are discussed in detail in the next section.

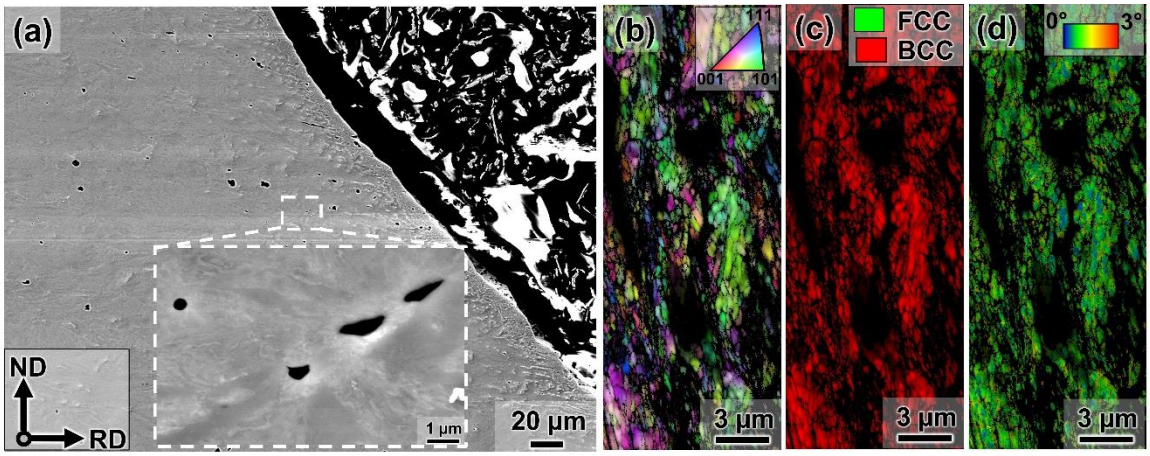

Figure. 3-12 SEM images and corresponding EBSD analysis of the cross-sectional area beneath the fracture surfaces of austempered time of 1000 s.

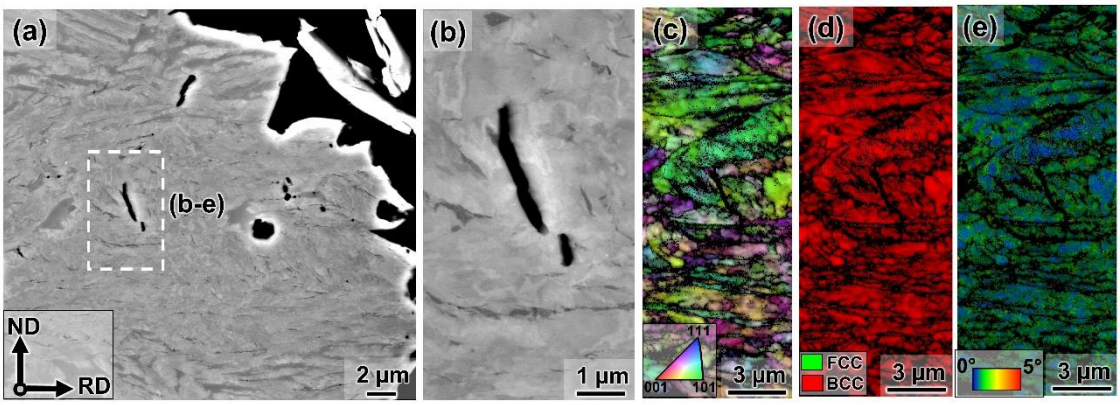

Figure. 3-13 SEM images and corresponding EBSD analysis of the cross-sectional area beneath the fracture surfaces of austempered time of 3600 s. (a, b) SEM images, (c) IPF map with IQ, (d) phase map with IQ, and (e) KAM map with IQ.

Figure. 3-14 shows the fracture surfaces of specimens. As shown in Figure.3-14(a), the fracture morphology in the 0 s-austempered specimen was a mixture of quasi-cleavage and intergranular fractures. In the 100 s-austempered specimen, the fracture surface consisted of quasi-cleavage facets and small dimples. As the austempering time increased, the fracture surface was mainly composed of typical dimples. Dimples in the specimen austempered for 1000 s were deeper and larger than those in the other specimens. As shown in Figure. 3-14(f), the fracture morphology of the TBF steel austempered for 3600 s exhibited small dimples and large quasi-cleavage facets.

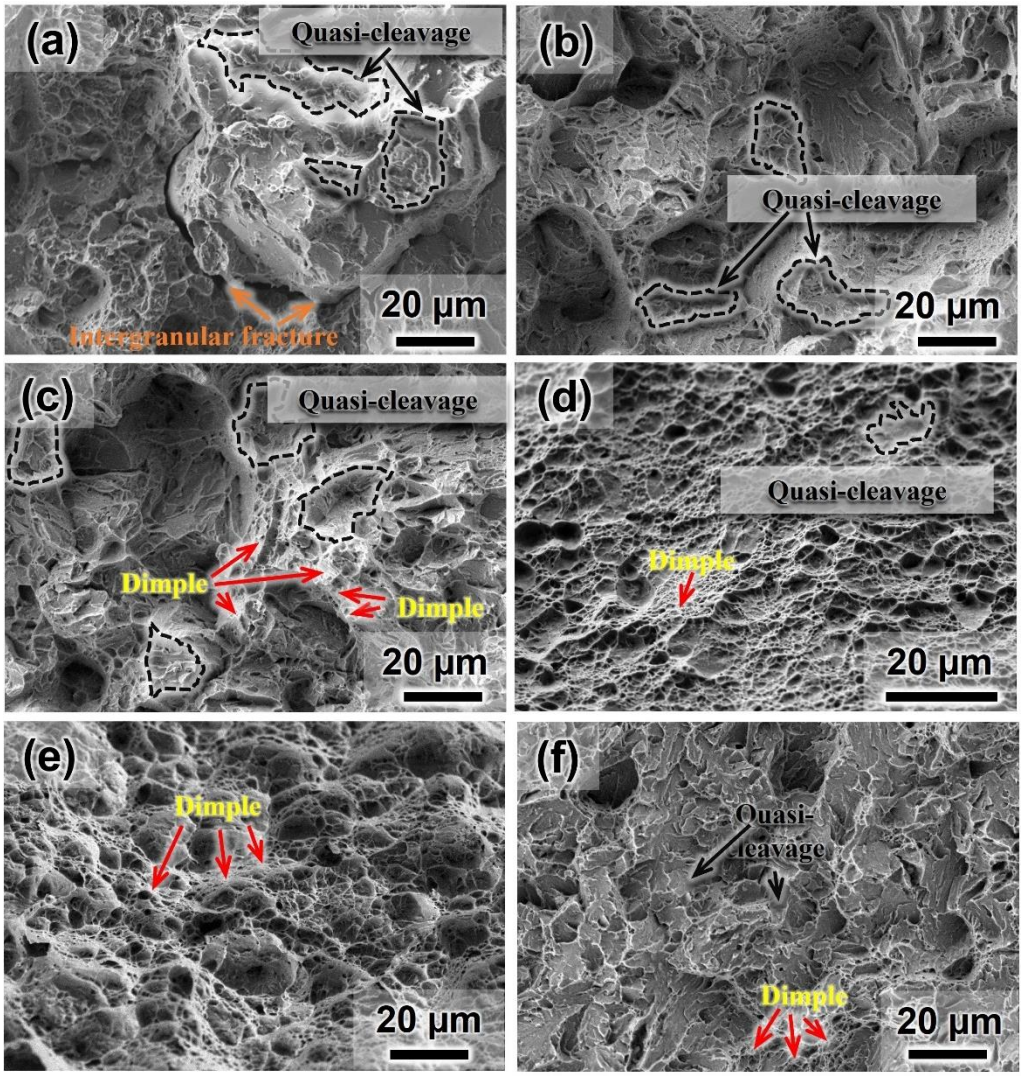

Figure. 3-14 SEM images of fracture surface of specimens austempered for (a) 0, (b) 100, (c) 200, (d) 500, (e) 1000, and (f) 3600 s.

3.4 Discussions

3.4.1 Microstructure evolution

The main purpose of annealing in the austenite region followed by austempering treatment is to obtain a matrix of bainitic ferrite and a certain amount of metastable retained austenite in TBF steels. Thus, the conditions of austempering treatment (*i.e.*, austempering temperature and time) are the important factors to determine the microstructure of the TBF steels. The schematic of the microstructural evolution during austempering treatment in TBF steels is shown in Figure. 3-15. Upon direct oil-quenching after annealing, the microstructure exhibited lath martensite and a small amount of retained austenite. The lath martensitic microstructure changed to a mixture of bainitic ferrite, retained austenite, and M/A constituents when the austempering time increased. The amount of bainitic ferrite increased with austempering time, which led to carbon partitioning in austenite owing to the low solubility of carbon in bainitic ferrite and the stabilization of austenite [33, 34]. Therefore, a large amount of austenite remained at room temperature, although oil quenching was conducted after austempering. It could be observed that the high volume fraction of retained austenite was obtained as austempering time between 100 and 1000 s. At an austempering time of 3600 s, some carbide particles precipitated and the amount of retained austenite decreased; however, the amount of bainitic ferrite/bainite was slightly higher than that in the TBF steel austempered for 1000 s. Jacques et al. [35] reported that preventing carbide precipitation improves austenite stability via carbon enrichment. Therefore, a longer austempering time had an adverse effect on the amount and stability of retained austenite in TBF steels.

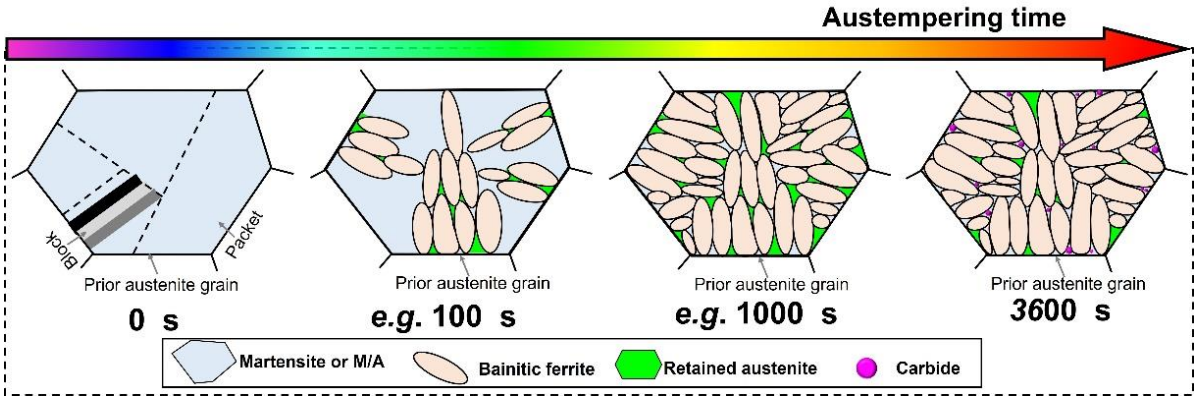

Figure. 3-15 Schematic image showing microstructural evolution subjected to austempering for different times and final cooling to room temperature.

3.4.2 Relationship between microstructure and mechanical properties

As the austempering time of TBF steels increased, it was observed that their UEl and TEl increased (Figure. 3-6). In the 100 s-austempered specimen, high and instantaneous work-hardening rates were observed at the beginning of straining, which remarkably decreased later. This was because the retained austenite with low stability transformed into martensite at a small strain, thus adversely affecting the UEl of the steel. In the austempering time range of 0–200 s, YS decreased due to the lower strength of bainitic ferrite when compared to martensite [36]. However, the YS of all these samples was higher than 900 MPa, which is significantly higher than that of conventional TRIP-aided steels with a polygonal ferrite matrix [37, 38]. Such a high YS can be attributed to the fine bainitic ferrite laths with a relatively high dislocation density in TBF steels when compared to polygonal ferrite in the conventional TRIP-aided steels [39]. In addition, the UTS and UEl were closely related to the work-hardening behavior and transformation behavior of retained austenite, as shown in Figure. 3-6(d). The deformation-induced martensitic transformation improves the work-hardening rate, and the necking occurs when true stress reaches the work-hardening rate. Moreover, if retained austenite possesses high stability, corresponding to high carbon concentration in retained austenite, the occurrence of the martensitic transformation of retained austenite is delayed. Resultantly, high work-hardening rate is kept until later stage of plastic strain. The UTS of 100 and 200 s-austempered TBF steels was higher than that of the 500 s-austempered specimen due to their bainitic ferrite and martensite matrix microstructures. In addition, their UEl was lower than that of the 500 s-austempered specimen, which lacked the TRIP effect at high strains. A low volume fraction of retained austenite and its carbon concentration, which implies a low stability of retained austenite, was noted in TBF steels austempered for 100 and 200 s (Figure. 3-5). Therefore, the effective transformation of a large amount of retained austenite did not occur in the high plastic strain region; instead, necking occurred in the low plastic strain region, unlike in the case of the specimens austempered for 500 and 1000 s. Consequently, the 100 and 200 s-austempered TBF steels exhibited low UEl and TEl (Figure. 3-6). It can be seen that the work-hardening rate in the 1000 s-austempered TBF steel before necking was higher than those in other samples. This can be attributed to the higher volume fraction and stability of retained austenite and a highly effective TRIP phenomenon, which delayed the onset of necking. However, at the austempering time of 3600 s, the bainitic ferrite/bainite laths assumed block-like shapes and the volume fraction of and total carbon content in retained austenite decreased (Figure. 3-5). These factors might have been responsible for the low UEl and TEl of this

specimen; furthermore, a small amount of undesirable carbide appeared in the matrix of this specimen and might have contributed to reducing its UEl and TEl [40]. The reduction in area of the TBF steels austempered for 500 and 1000 s was improved, whereas that of the sample austempered for 3600 s was reduced. Local elongation, which corresponds to elongation after necking, followed a similar trend. These two parameters, local elongation and the reduction in area are affected by damages, such as voids, and the cracks evolution behavior. The fracture mechanism of the TBF steels will be discussed in the next section.

3.4.3 Relationship between microstructure and fracture behavior

From the fracture surfaces shown in Figure. 3-14, it can be inferred that the fracture mode of the TBF steels was dependent on the austempering time. A schematic of the changes occurring in the fracture behavior of TBF steels with respect to austempering time is shown in Figure. 3-16. The sources of the voids are cracks and inclusions. Specifically, the crack appeared along microstructural interfaces such as bainitic ferrite/ martensite interfaces, grain boundaries, and internal martensite boundaries (*e.g.* packet boundaries). When the cracks open largely, it becomes voids. In addition, the inclusions act as a source of the voids in the grain interior. In the specimen without austempering, numerous secondary cracks could be observed mainly at prior austenite grain boundaries and partially in the grain interior (Figure. 3-8 and Figure. 3-10). Intergranular and transgranular crack initiation and growth resulted in intergranular and quasi-cleavage features in the fracture surface (Figure. 3-14 (a)). In addition, a predominant number of the secondary cracks were formed parallel to the tensile direction, which is hereafter referred to as a longitudinal crack (Figure.3-16(a)). Longitudinal cracks have been reportedto occur in Mn segregation bands, including MnS inclusions in martensitic steel and they are reported to accelerate brittle crack propagation [41]. Because the steel used in this study includes Mn, it may be surmised that the observed longitudinal cracks were formed due to the same reason and they assisted in brittle fracture. In addition, TBF steels without austempering did not exhibit a sufficient TRIP effect to suppress crack initiation and propagation due to a low volume fraction and carbon concentration in retained austenite; thus, this specimen underwent premature fracture after yielding.

At austempering times of 100 and 200 s, the intergranular crack length decreased and void initiation was enhanced, as shown in Figure. 3-8. Accordingly, the major fracture-surface features changed from intergranular to quasi-cleavage (Figure. 3-14(b) and Figure. 3-14 (c)). In addition, dimples, which indicate ductile fracture, appeared on the fracture surface of the specimen austempered for 200 s. The suppression of intergranular fracture is attributed to the softening of the matrix due to the transformation

from austenite to bainitic ferrite. Meanwhile, the appearance of quasi-cleavage and dimples can be interpreted from the crack/void initiation sites. Most of the quasi-cleavage cracks were initiated at the martensite lath and packet boundaries and/or the matrix/martensite or matrix/M/A constituent interfaces [42, 43]. In addition, a number of voids were formed at the bainitic ferrite and martensite lath boundaries. Because crack/void initiation and growth can easily occur at the microstructural interfaces of soft and hard phases [44, 45], quasi-cleavage cracks and void initiation/growth can be associated with the formation of new interfaces by the austempering and subsequent deformation (Figure. 3-16(b) and Figure. 3-16(c)). In other words, crack/void formation and growth within prior austenite grains can be attributed to an increase in the number density of interfaces between carbon-free bainitic ferrite and high-carbon-containing deformation-induced martensite. However, since bainitic ferrite is more ductile than martensite, plasticity-induced crack opening resulted in the significant crack blunting in the austempered samples. Thus, the crack length was dramatically shortened and void density increased (Figure. 3-9).

When austempered for 500 and 1000 s, the TBF steel showed a large amount of relatively stable retained austenite, as shown in Figure. 3-5. The retained austenite was mainly located at the lath and packet boundaries, as shown in Figure. 3-4. The transformation of retained austenite was prominent in the high strain region during tensile deformation (Figure. 3-5), which resulted in the suppression of void/crack initiation and growth (Figure. 3-16(d) and Figure. 3-16(e)). Because the TBF steel austempered for 1000 s exhibited a high volume fraction and carbon concentration in retained austenite when compared to the specimen austempered for 0 s, the brittle features were fully suppressed and the fracture surface was covered only with dimples.

When the austempering treatment was carried out for 3600 s, the microstructure of the resultant TBF steel consisted of a bainitic ferrite/ bainite matrics, a smaller amount of retained austenite when compared to that at 500 and 1000 s, and carbide precipitates (Figures. 3-2, Figure. 3-4 and Figure. 3-5); this limited the TRIP effect during deformation. Meanwhile, cracks propagated along the bainitic ferrite and/or bainite lath boundaries and these coalesced with other cracks (Figure.3-16(f)). Therefore, the 3600 s-austempered TBF steel exhibited relatively lower ductility as compared to the 500 and 1000 s-austempered steels; in addition, the void density slightly decreased and crack length slightly increased at 3600 s when compared to the 500 and 1000 s specimens (Figure.3-9).

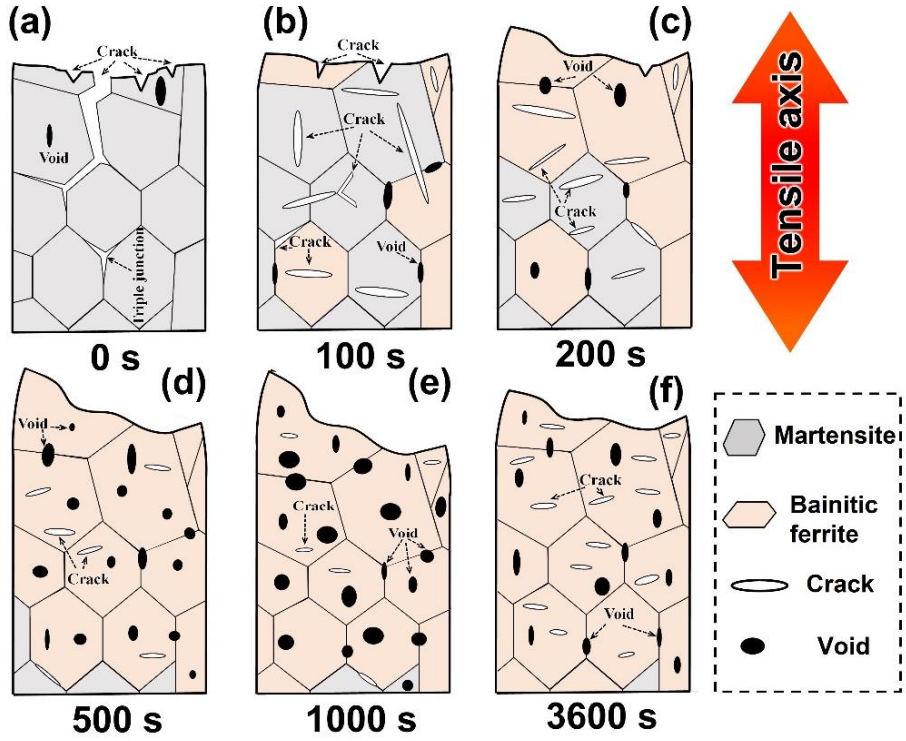

Figure. 3-16. Schematic showing the fracture behavior of TBF steels as a function of austempering time.

3.5 Summary

Multiphase microstructures were obtained by austempering treatment in Fe-0.4C-1.5Si-1.5Mn TBF steel for different austempering time. The correlation between microstructure and mechanical properties was systematically studied and their microscopic fracture behavior was investigated. The summaries are as follows:

（1） The microstructure of the TBF steels consisted of bainitic ferrite/bainite, retained austenite, and martensite. When the austempering time increased from 0 to 1000 s, the volume fraction of retained austenite increased from 2.1 to around 12%, followed by a decrease to 4.8% at an austempering time of 3600 s.

（2） The UEl and TEl of TBF steels were remarkably dependent on the austempering time; UEl increased from 0.5% to 19.8% and subsequently decreased to 9.7% whereas TEl increased from 3.6% to 23.5% and subsequently decreased to 11.9%. The TBF steel austempered for 1000 s showed excellent mechanical properties with a YS of 960 MPa, UTS of 1182 MPa, and TEl of 23.5%.

（3） As the austempering time increased from 0 to 3600 s, void density in the TBF steel initially increased and then decreased slightly, meanwhile, the mean crack length decreased from 29.1 to 10.2 μm and then slightly increased to 13.4 μm, thus

changing the fracture mode from intergranular to quasi-cleavage and dimplefractures. Moreover, bainitic ferrite lath boundaries became the main path for crack propagation during deformation.

（4） The excellent strength-elongation balance of the TBF steel austempered for 1000 s was attributed to the effective deformation induced transformation in a large fraction of the metastable retained austenite, which effectively suppressed crack and void initiation, propagation, and growth.

3.6 Reference

[1]. D. K. Matlock, J. G. Speer, Processing opportunities for new advanced high-strength sheet steels, Mater. Manuf. Process. 25 (2010) 7–13.

[2]. D. W. Suh, S. J. Kim, Medium Mn transformation-induced plasticity steels: recent progress and challenges, Scripta Mater. 126 (2017) 63–67.

[3]. B. C. De Cooman, Y. Estrin, K. S. Kim, Twinning-induced plasticity (TWIP) steels, Acta Mater. 142 (2018) 283–362.

[4]. B. C. De Cooman, Structure-properties relationship in TRIP steels containing carbide-free bainite, Curr. Opin. Solid State Mater. Sci. 8 (2004) 285–303.

[5]. K. Sugimoto, T. Hojo, Fatigue hardening behavior of 1.5 GPa grade transformation-induced plasticity-aided martensitic steel, Metall. Mater. Trans. A. 47 (2016)5272–5279.

[6]. R. Ranjan, H. Beladi, S. B. Singh, P. D. Hodgson, Thermo-mechanical processing of TRIP-aided steels, Metall. Mater. Trans. A. 46 (2015) 3232–3247.

[7]. Y. F. Shen, L. N. Qiu, X. Sun, L. Zuo, P. K. Liaw, D. Raabe, Effects of retained austenite volume fraction, morphology, and carbon content on strength and ductility of nanostructured TRIP-assisted steels, Mater. Sci. Eng. A. 636 (2015) 551–564.

[8]. S. Kaar, D. Krizan, J. Schwabe, H. Hofmann, T. Hebesberger, C. Commenda, L. Samek, Influence of the Al and Mn content on the structure-property relationship in density reduced TRIP-assisted sheet steels, Mater. Sci. Eng. A. 735 (2018) 475–486.

[9]. K. D. Krizan, S. Hahn, A. Pichler, Relationship between microstructure and mechanical properties in Nb–V microalloyed TRIP steel, Mater. Sci. Eng. A. 31 (2015) 661–667.

[10]. J. Chiang, J. D. Boyd, A. K. Pilkey, Effect of microstructure on retained austenite stability and tensile behaviour in an aluminum-alloyed TRIP steel, Mater. Sci. Eng. A. 638 (2015) 132–142.

[11]. D. Krizan, B. C. De Cooman, Mechanical properties of TRIP steel microalloyed

with Ti, Metall. Mater. Trans. A. 45 (2014) 3481–3492.

[12]. G. K. Tirumalasetty, M. A. Van Huis, C. Kwakernaak, J. Sietsma, W.G. Sloof, H. W. Zandbergen, Deformation-induced austenite grain rotation and transformation in TRIP-assisted steel, Acta Mater. 60 (2012) 1311–1321.

[13]. E. P. Kwon, S. Fujieda, K. Shinoda, S. Suzuki, Characterization of transformed and deformed microstructures in transformation induced plasticity steels using electron backscattering diffraction, Mater. Sci. Eng. A. 528 (2011) 5007–5017.

[14]. P. J. Jacques, Transformation-induced plasticity for high strength formable steels, Curr. Opin. Solid State Mater. Sci. A. 8 (2004) 259–265.

[15]. J. Mahieu, J. Maki, B. C. De Cooman, S. Claessens, Phase transformation and mechanical properties of Si-free CMnAl transformation-Induced plasticity-aided steel, Metall. Mater. Trans. A. 33 (2002) 2573–2580.

[16]. S. Cheng, X. L. Wang, Z. L. Feng, B. Clausen, H. Choo, P.K. Liaw, Probing the characteristic deformation behaviors of transformation-induced plasticity steels, Metall. Mater. Trans. A. 39 (2008) 3105–3112.

[17]. E. M. Bellhouse, J.R. Mcdermid, Effect of continuous galvanizing heat treatments on the microstructure and mechanical properties of high Al-low Si transformation induced plasticity steels, Metall. Mater. Trans. A. 41 (2010) 1460–1473.

[18]. K. Sugimoto, S. Hidaka, H. Tanino, J. Kobayashi, Warm formability of 0.2 pct C-1.5 pct Si-5 pct Mn transformation-induced plasticity-aided steel, Metall. Mater. Trans. A. 48 (2017) 2237–2246.

[19]. G. Lacroix, T. Pardoen, P.J. Jacques, The fracture toughness of TRIP-assisted multiphase steels, Acta Mater. 56 (2008) 3900–3913.

[20]. K. Sugimoto, M. Tsunezawa, T. Hojo, S. Ikeda, Ductility of 0.1–0.6C–1.5Si–1.5Mn ultra high-strength TRIP-aided sheet steels with bainitic ferrite matrix, ISIJ Int. 44 (2004) 1608–1614.

[21]. K. Sugimoto, T. Iida, J. Sakaguchi, T. Kashima, Retained austenite characteristics and tensile properties in a TRIP type bainitic sheet steel, ISIJ Int. 40 (2000) 902–908.

[22]. S. Hashimoto, S. Ikeda, K. Sugimoto, S. Miyake, Effects of Nb and Mo addition to 0.2% C–1.5% Si –1.5% Mn steel on mechanical properties of hot rolled TRIP aided steel sheets, ISIJ Int. 44 (2004) 1590–1598.

[23]. E. Abbasi, W.M. Rainforth, Microstructural evolution during bainite transformation in a vanadium microalloyed TRIP-assisted steel, Mater. Sci. Eng. A. 651 (2016) 822–830.

[24]. K. Hausmann, D. Krizan, K. S. Hahn, A. Pichler, E. Werner, The influence of Nb

on transformation behavior and mechanical properties of TRIP-assisted bainitic–ferritic sheet steels, Mater. Sci. Eng. A. 588 (2013) 142–150.

[25]. K. Sugimoto, M. Misu, M. Kobayashi, H. Shirasawa, Effects of second phase morphology on retained austenite morphology and tensile properties in a TRIPaided dual-phase steel sheet, ISIJ Int. 33 (1993) 775–782.

[26]. K. Sugimoto, M. Kobayashi, S. Hashimoto, Ductility and strain-induced transformation in a high-strength transformation-induced plasticity-aided dualphase steel, Metall. Trans. A. 23 (1992) 3085–3091.

[27]. T. Furuhara, T. Chiba, T. Kaneshita, H. Wu, G. Miyamoto, Crystallography and interphase boundary of martensite and bainite in steels, Metall. Mater. Trans. A. 48 (2017) 2739–2752.

[28]. V. T. Duong, Y. Y. Song, K. S. Park, H. K. D. H. Bhadeshia, D. W. Suh, Austenite in transformation-induced plasticity steel subjected to multiple isothermal heat treatments, Metall. Mater. Trans. A. 45 (2014) 4201–4209.

[29]. K. W. Kim, K. I. Kim, C. H. Lee, J. Y. Kang, T. H. Lee, K. M. Cho, K. H. Oh, Control of retained austenite morphology through double bainitic transformation, Mater. Sci. Eng. A. 673 (2016) 557–561.

[30]. A. A. Gorni, Steel forming and heat treatment handbook. 2019, 52.

[31]. M. A. Valdes-Tabernero, C. Celada-Casero, I. Sabirov, A. Kumar, R.H. Petrov, The effect of heating rate and soaking time on microstructure of an advanced high strength steel, Mater. Char. 155 (2019), 109822.

[32]. A. Arlazarov, O. Bouaziz, J. P. Masse, F. Kegel, Characterization and modeling of mechanical behavior of quenching and partitioning steels, Mater. Sci. Eng. A. 620 (2015) 293–300.

[33]. S. Zaefferer, P. Romano, F. Friedel, EBSD as a tool to identify and quantify bainite and ferrite in low-alloyed Al-TRIP steels, J. Microsc. 230 (2008) 499–508.

[34]. I. Timokhina, H. Beladi, X.Y. Xiong, P.D. Hodgson, On the low temperature strain aging of bainite in the TRIP steel, Metall. Mater. Trans. 44 (2013) 5177–5191.

[35]. P. Jacques, E. Girault, T. Catlin, N. Geerlofs, T. Kop, S. Van Der Zwaag, F. Delannay, Bainite transformation of low carbon Mn-Si TRIP-assisted multiphase steels: influence of silicon content on cementite precipitation and austenite retention, Mater. Sci. Eng. A. 273–275 (1999) 475–479.

[36]. H. S. Park, J. B. Seol, N. S. Lim, S. I. Kim, C. G. Park, Study of the decomposition behavior of retained austenite and the partitioning of alloying elements during tempering in CMnSiAl TRIP steels, Mater. Des. 82 (2015) 173–180.

[37]. H. K. D. H. Bhadeshia, D. V. Edmonds, The bainite transformation in a silicon

steel, Metall. Trans. A. 10 (1979) 895–907.

[38]. P. J. Jacques, J. Ladrière, F. Delannay, On the influence of interactions between phases on the mechanical stability of retained austenite in transformation-induced plasticity multiphase steels, Metall. Mater. Trans. A. 32 (2001) 2759–2768.

[39]. K. Lee, J. H. Ryu, S. W. Lee, W. H. Lee, J. I. Kim, D. W. Suh, Influence of the initial microstructure on the heat treatment response and tensile properties of TRIP assisted steel, Metall. Mater. Trans. A. 47 (2016) 5259–5265.

[40]. H. J. Jun, S. H. Park, S. D. Choi, C. G. Park, Decomposition of retained austenite during coiling process of hot rolled TRIP-aided steels, Mater. Sci. Eng. A. 379 (2004) 204–209.

[41]. D. Sasaki, M. Koyama, H. Noguchi, Factors affecting hydrogen-assisted cracking in a commercial tempered martensitic steel: Mn segregation, MnS, and the stress state around abnormal cracks, Mater. Sci. Eng. A. 640 (2015) 72–81.

[42]. E. Hornbogex, Martensitic transformation at a propagating crack, Acta Metall. 26 (1977) 147–152.

[43]. M. Calcagnotto, Y. Adachi, D. Ponge, D. Raabe, Deformation and fracture mechanisms in fine- and ultrafine-grained ferrite/martensite dual-phase steels and the effect of aging, Acta Mater. 59 (2011) 658–670.

[44]. M. Koyama, C. C. Tasan, E. Akiyama, K. Tsuzaki, Hydrogen-assisted decohesion and localized plasticity in dual-phase steel, Acta Mater. 70 (2014) 174–187.

[45]. H. Ghadbeigi, C. Pinna, S. Celotto, Failure mechanisms in DP600 steel: initiation, evolution and fracture, Mater. Sci. Eng. A.588 (2013) 420–431.

Chapter 4: Effect of hydrogen and deformation temperature on mechanical properties and fracture behavior of TRIP-aided bainitic ferrite steel

4 Effect deformation temperature on mechanical properties and fracture behavior of TRIP-aided bainitic ferrite steel

4.1 Introduction

One of the problems in high-strength TRIP-aided steels is HE [1–3]. Furthermore, each microstructural component in multiphase TRIP-aided steels exhibited variable hydrogen trapping ability and different diffusivity and solubility of hydrogen, making it difficult to evaluate the hydrogen-related behavior of TRIP-aided steels [4, 5]. Hence, fundamental studies on HE are essential to understand mechanical properties and improve the resistance to HE of TRIP-aided steels.

A key factor affecting HE resistance of TRIP-aided steels is a degree of the TRIP effect, because deformation-induced martensite is a preferential site for hydrogen-related cracking. The degree of the TRIP effect is dependent on volume fraction and stability of retained austenite [6, 7]. In particular, the mechanical stability of austenite is sensitive to deformation conditions, *e.g.*, strain rate, stress state, and deformation temperature [8, 9]. Because HE resistance is intrinsically dependent on the deformation conditions even without martensitic transformation, clarification of underlying deformation condition dependence of the HE beheavior of the TRIP-aided steels has been regarded as a big challenge. Nonetheless, TRIP-aided steels used as automobile structural parts were inevitably exposed to different temperatures and hydrogen environments during production and service [10, 11]. Therefore, the investigation of the deformation temperature dependence of mechanical properties of TRIP-aided steels in the presence of hydrogen needs to be conducted. In addition, examining the temperature effect is helpful to understand the fracture behaviors with different austenite stability at an identical austenite fraction, although there is the abovementioned complexity in the deformation condition dependence of HE resistance.

In the present study, SSRTs at different deformation temperatures were performed using the hydrogen-uncharged and hydrogen-charged specimens. Specifically, synergistic effects of deformation temperature and hydrogen on mechanical properties of TRIP-aided steel with bainitic ferrite matrix were evaluated based on behavioral characteristics of deformation-induced martensitic transformation and local plasticity evolution.

4.2 Experimental procedure

The cold-rolled sheets were annealed at 900 ℃ for 1200 s, followed by the

austempering treatment at 400 ℃ for 1000 s. Subsequently, the sheets were oil-quenched to room temperature. The detailed austempering procedure has been reported as shown in Chapter 3. Electrochemical hydrogen charging to the specimens was performed in a 3% NaCl aqueous solution containing 3 g/L NH_4SCN at a constant current density of 10 A/m^2 for 48 h before tensile tests. A platinum wire was used as the counter electrode.

SSRT tests were performed on a tensile testing machine equipped with a thermostatic chamber at an initial strain rate of 1×10^{-4} s^{-1} at different deformation temperatures of -100, -30, 21, and 100 °C. The 0.2% offset stress was regarded as the yield strength. The hydrogen desorption behavior was analyzed using TDS.

The initial and deformed microstructures of the specimens were characterized using XRD, SEM, and EBSD. In addition, the fracture surfaces were examined using SEM. The transformation ratio of retained austenite was defined as:

$$\text{Transformation ratio (\%)}=\frac{V_{\gamma\text{-bef}}-V_{\gamma\text{-aft}}}{V_{\gamma\text{-bef}}}\times100 \quad (4\text{-}1)$$

where $V_{\gamma\text{-bef}}$ and $V_{\gamma\text{-aft}}$ are the volume fractions of retained austenite before and after the tensile tests, respectively.

4.3 Results

4.3.1 Microstructural characterizations

Figure. 4-1 shows the initial microstructure of the present steel after the austempering treatment, which comprised bainitic ferrite and retained austenite. The volume fraction of the retained austenite was 11.0 ± 1.2 vol% (hereafter %) based on XRD measurements. Furthermore, the retained austenite exhibited two different types: blocky and filmy morphologies. The blocky retained austenite was located at prior austenite grain boundaries, whereas the filmy retained austenite was observed between the bainitic ferrite laths. In addition, the prior austenite grain size was calculated to be approximately 21 ± 3 μm using the intercept method. The packet size and block width of bainitic ferrite were measured by the intercept method base on the IPF maps, which were 13.6 ± 1.3 and 1.6 ± 0.3 μm, respectively.

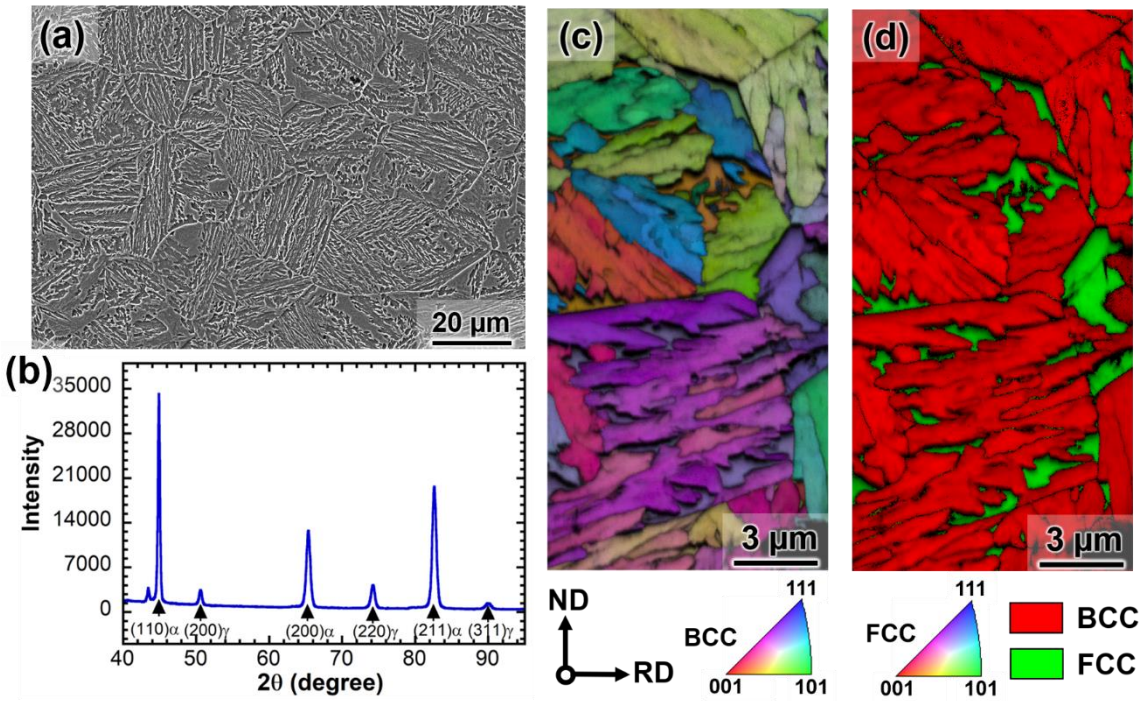

Figure. 4-1 Initial microstructure of the present steel: (a) SEM image; (b) XRD pattern; (c) IPF with IQ; (d) phase map with IQ.

4.3.2 Tensile properties

Figures. 4-2(a) and (b) show engineering stress–strain curves of the hydrogen-uncharged and hydrogen-charged specimens at different deformation temperatures. All the specimens exhibited continuous yielding behavior, which was commonly observed in TRIP-aided steels [12, 13]. Post-necking strain was observed in the hydrogen-uncharged specimens instead of the hydrogen-charged specimens. The specimens deformed at 21 and 100 ℃ exhibited a serrated flow in the curves, irrespective of hydrogen charging, which indicated the occurrence of dynamic strain aging [14] (the serrated flow at -100 ℃ arises from temperature instability). The degree of the serrated flow was reduced by the hydrogen charging. This might be attributed to the combined effects of the solution hardening, the dislocation pinning, and the enhancement of dislocation motion owing to the hydrogen absorption [4, 11]. With regard to the work-hardening behavior, as shown in Figures. 4-2(c) and (d), work-hardening rates tended to increase with a decrease in the test temperature and did not significantly change with hydrogen charging. The premature fracture in the hydrogen-charged specimens tested at and below 21℃ occurred before satisfying the Considère criteria.

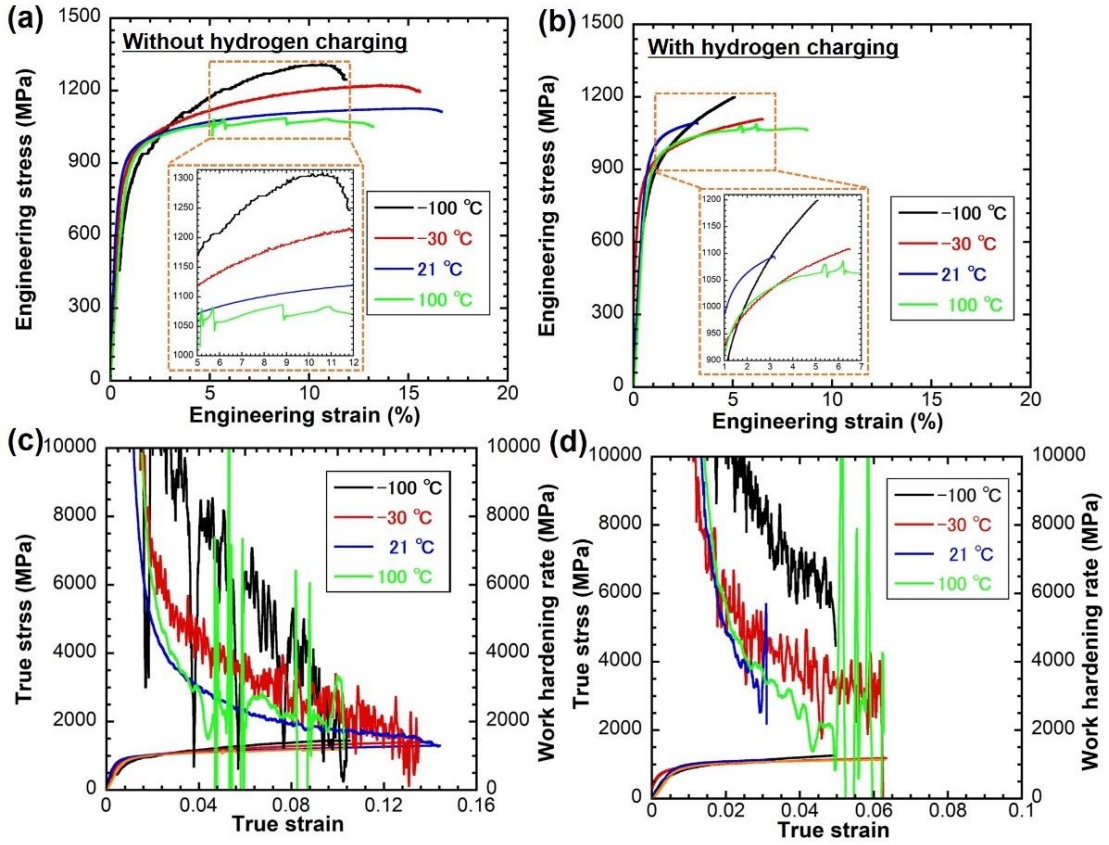

Figure. 4-2 (a, b) Engineering stress–strain and (c, d) true stress–strain and work-hardening rate curves of (a, c) hydrogen-uncharged and (b, d) hydrogen-charged specimens.

Tensile properties of the hydrogen-uncharged and hydrogen-charged specimens are illustrated in Figure. 4-3. The deformation temperature dependence of UTS with and without hydrogen charging exhibited similar variations. Hydrogen charging slightly increased the YS (Figure. 4-3(a)) and deteriorated the UEl (Figure. 4-3(b)) at all the temperature ranges.

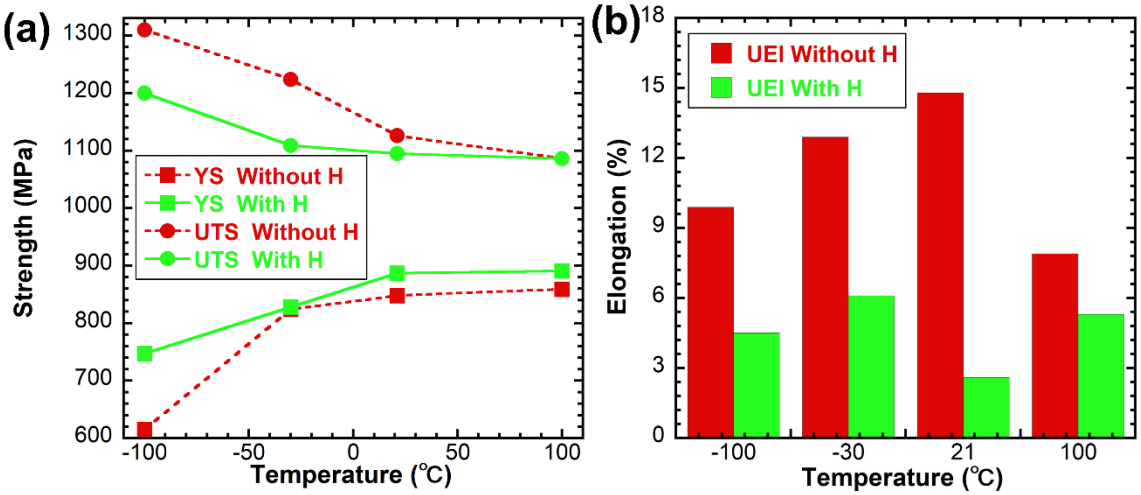

Figure. 4-3 Deformation temperature dependence of mechanical properties on specimens with and without hydrogen charging. (a) YS, and UTS, (b) UEl.

Figure. 4-4 shows hydrogen desorption profiles of the hydrogen-charged specimens tensile-tested at different temperatures. Only a single peak appeared in each profile, and the peak positions of the specimens tested at 21 and 100 ℃ were higher than the others. The cumulative hydrogen content (C_H) of the specimens tested at -100, -30, 21, and 100 ℃ were 1.41, 1.79, 1.70, and 1.59 mass ppm, respectively.

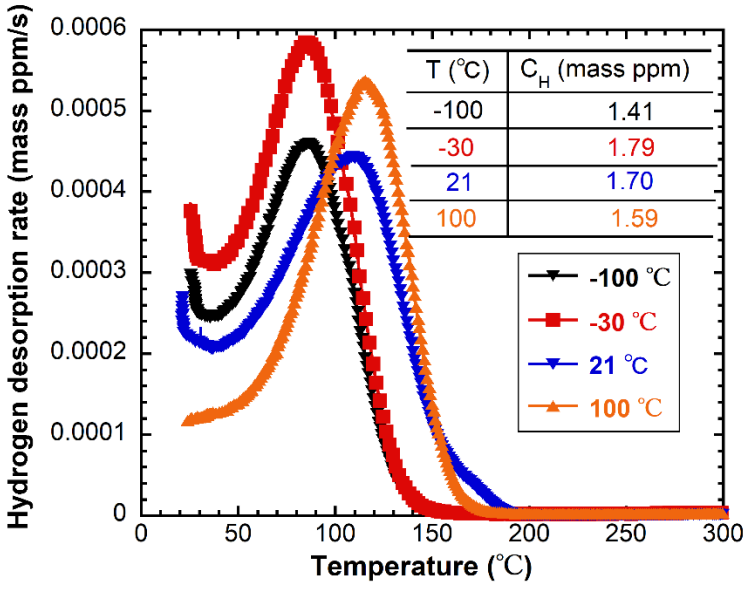

Figure. 4-4 Thermal desorption curves of specimens at different deformation temperatures. T and C_H denote the deformation temperature and hydrogen content of specimens, respectively.

4.3.3 Microstructure evolution behavior

Figure. 4-5(a) shows XRD patterns of hydrogen-uncharged specimens after the tensile test. The XRD analysis in this study was performed using a uniformly deformed region of fractured specimens. Based on the XRD profiles, the volume fraction of the retained austenite was obtained (Figure. 4-5(b)) and decreased with a decrease in the test temperature. The same variation trend in the volume fraction of the retained austenite was observed in hydrogen-charged specimens after the tensile test (Figure. 4-6). The volume fraction of the retained austenite of hydrogen-charged specimens fractured at and below 21 ℃ was higher than that of hydrogen-uncharged specimens at the same deformation temperatures.

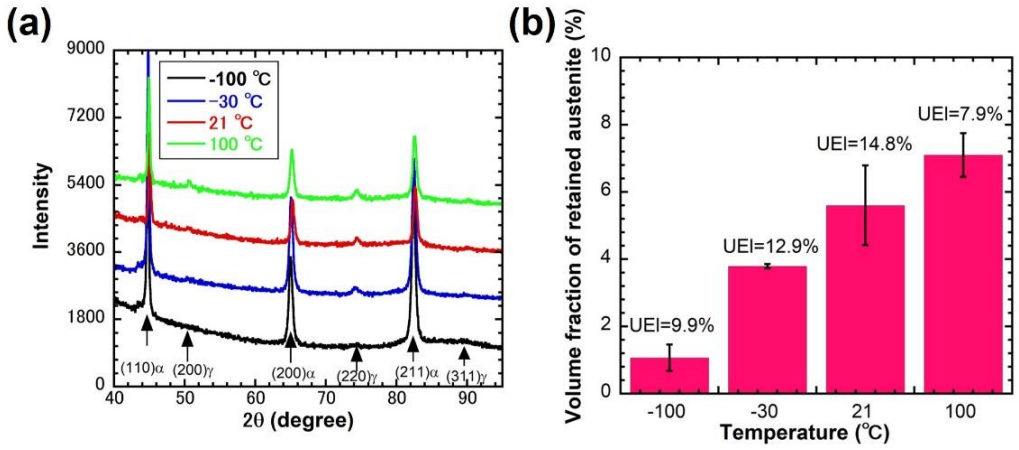

Figure. 4-5 (a) XRD patterns and (b) volume fraction of the retained austenite measured using uniformly deformed portions of hydrogen-uncharged specimens fractured at different temperatures.

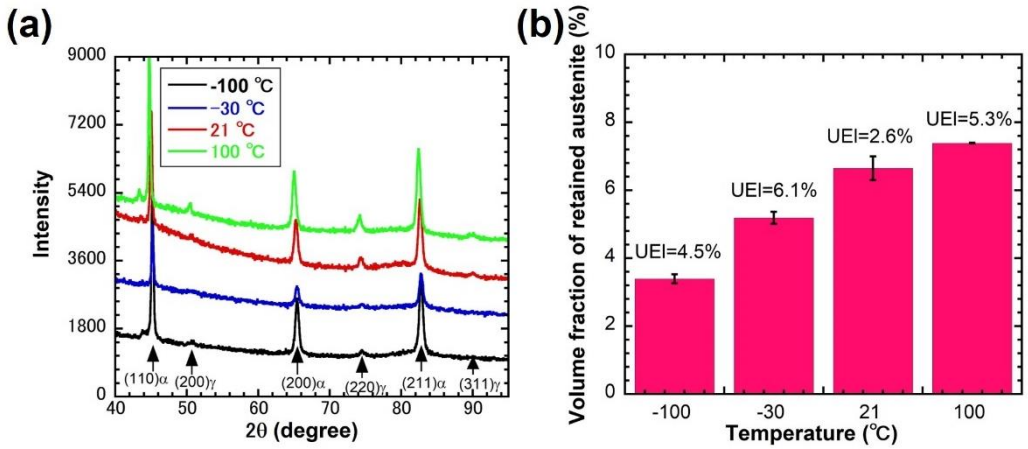

Figure. 4-6 (a) XRD patterns and (b) volume fraction of the retained austenite measured using uniformly deformed portions of hydrogen-charged specimens fractured at different temperatures.

Figure. 4-7(a) shows an XRD pattern and volume fraction of the retained austenite of an undeformed specimen before and after immersion into liquid nitrogen (-196 °C) for 30 s to reveal the thermal stability of the retained austenite. The volume fraction of the retained austenite after immersion into liquid nitrogen was similar to that before cooling, although the M_s temperature of retained austenite was calculated as approximately 34 °C [14]. It is implied that the volume fraction of the retained austenite before each tensile test ($V_{\gamma\text{-bef}}$) is constant in the present tensile test conditions because no thermally induced martensitic transformation significantly occurred before the tensile test at respective temperatures. Figure. 4-7(b) displays the transformation ratio of the retained austenite under each condition. In the hydrogen-uncharged and hydrogen-charged specimens, the transformation ratio of the retained austenite increased with a decrease in the deformation temperature, but hydrogen charging decreased the transformation ratio of the retained austenite. The decrease in the transformation ratio due to the hydrogen charging might be attributed to the occurrence of premature fracture, resulting in the small UEl (*i.e.*, applying small plastic deformation) in the hydrogen-charged specimens.

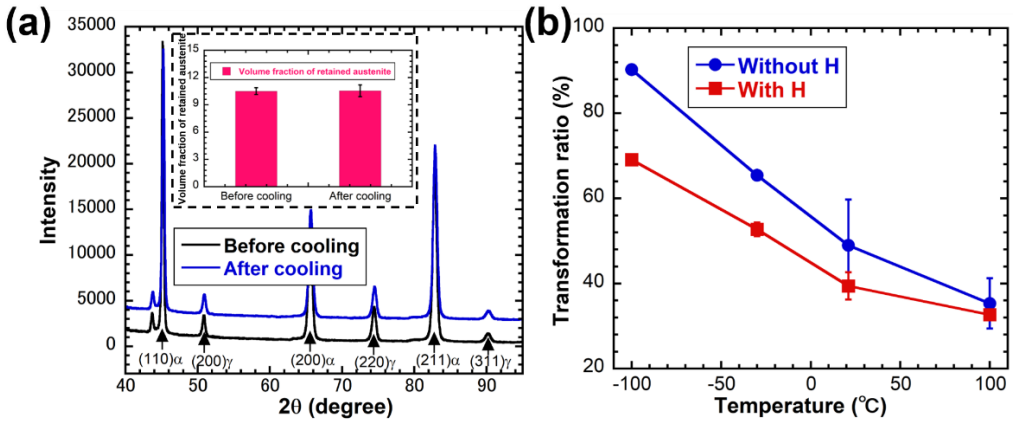

Figure. 4-7 (a) XRD pattern and volume fraction of the retained austenite of an undeformed specimen before and after immersion into liquid nitrogen (-196 °C). (b) Transformation ratio of the retained austenite of the hydrogen-uncharged and hydrogen-charged specimens plotted against deformation temperature.

To characterize the plasticity/transformation behavior during post-uniform elongation, microstructures of two different regions in the fractured specimens were observed. Specifically, regions within 3 mm from the fracture surface and at a distance of >3 mm from the fracture surface were observed. Hereafter, the former and latter regions are referred to as near-fracture-surface region and uniformly deformed region, respectively. Figures. 4-8(a) and (b) exhibit that hydrogen-uncharged specimens tested at -100 and -30 °C exhibited ~1% fraction of the retained austenite in the uniformly

deformed region, and the retained austenite fraction was nearly equal to those of the near-fracture-surface regions. When the deformation temperature was at and above 21 ℃, the remaining retained austenite fraction in the hydrogen-uncharged specimens increased with an increase in the test temperature, and there were significant differences in the retained austenite fraction between the uniformly deformed and near-fracture-surface regions (Figures. 4-8(c) and (d)). The retained austenite fraction of the hydrogen-charged specimens was higher than those of the hydrogen-uncharged specimens, which is consistent with the XRD results. The retained austenite fractions of the uniformly deformed regions at -100, -30, and 21 ℃ were nearly the same as those of the near-fracture-surface regions (Figures. 4-8(e)–(g)). For the hydrogen-charged specimen fractured at 100 ℃, a significant difference in the retained austenite fraction between the uniformly deformed and near-fracture-surface regions appeared (Figure. 4-8(h)).

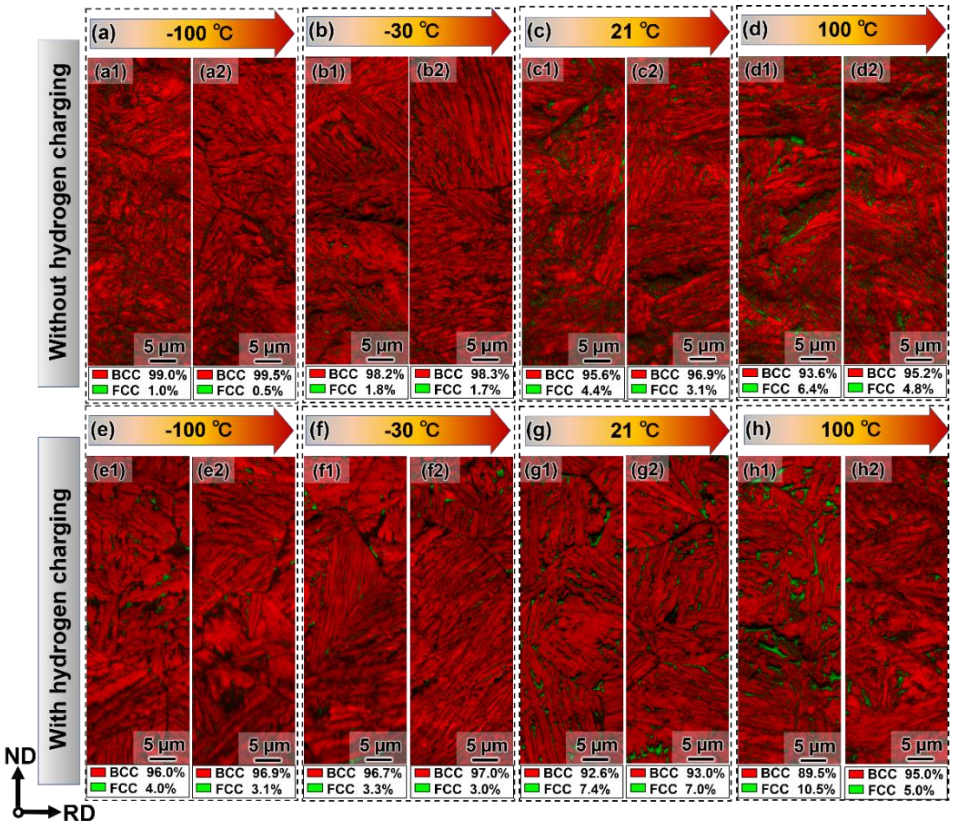

Figure. 4-8 Phase maps of hydrogen-uncharged and hydrogen-charged specimens at deformation temperatures of (a, e) -100, (b, f) -30, (c, g) 21, and (d, h) 100 ℃. Left and right images of each set correspond to the uniformly deformed and near-fracture-surface regions, respectively. The percentage listed in each image indicates area fraction of each phase.

According to KAM maps in the same locations as Figure. 4-9, plasticity evolution became more significant in the hydrogen-uncharged specimens than that in the hydrogen-

charged specimens, irrespective of the deformation temperature (Figure. 4-9). This result is consistent with the result that the elongation was deteriorated by hydrogen charging. In the hydrogen-charged specimens, a significant evolution of KAM values appeared at the deformation temperature of 100 ℃.

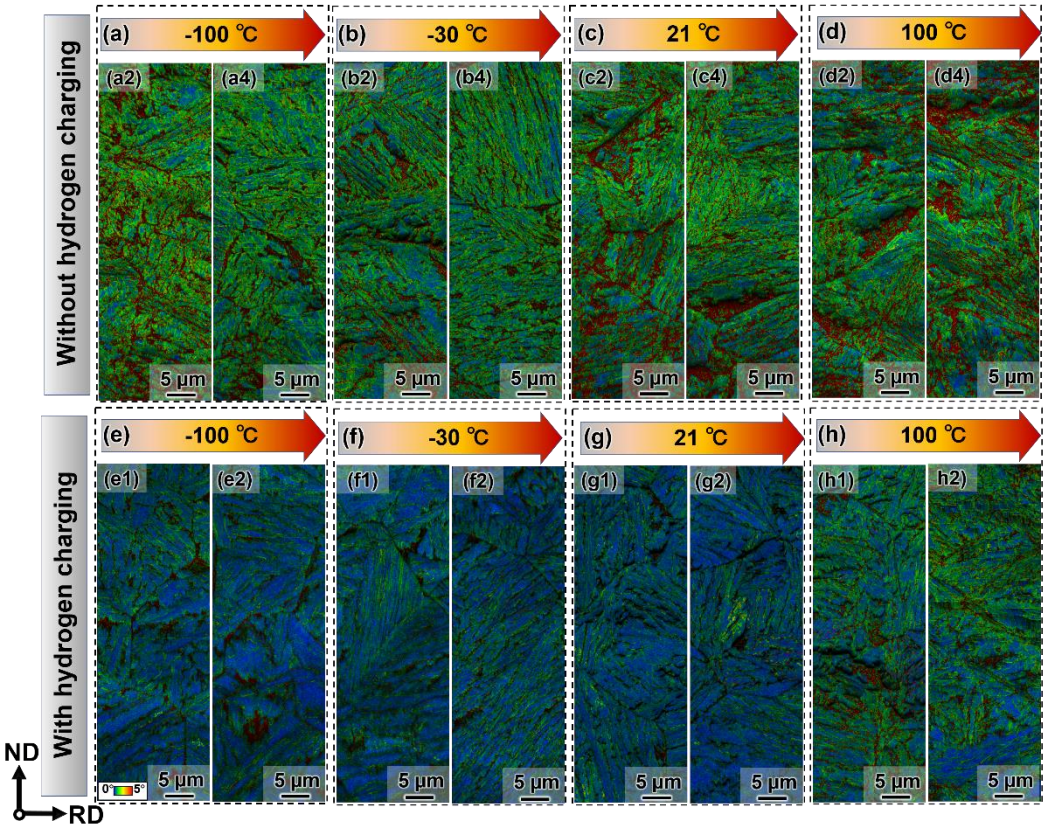

Figure. 4-9 KAM maps of the hydrogen-uncharged and hydrogen-charged specimens at deformation temperatures of (a, e) -100, (b, f) -30, (c, g) 21, and (d, h) 100 ℃. Left and right images of each set correspond to the uniformly deformed and near-fracture-surface regions, respectively.

4.3.4 Fracture surface

Figure. 4-10 shows fractographs of the hydrogen-uncharged specimens. In the hydrogen-uncharged specimens, with an increase in the deformation temperature from -100 to 100 ℃, the shear lip zone gradually enlarged, exhibiting the “cup and cone-like” fracture based on the macroscopic scale. Moreover, fractographic features changed from the quasi-cleavage (Figures. 4-10(b) and (c)) and quasi-cleavage/ductile mixed modes (Figures. 4-10(e) and (f)) to ductile mode. When hydrogen was introduced, quasi-cleavage features were observed for specimens fractured at -100 and -30 ℃. Hydrogen-charged specimens deformed at 21 and 100 ℃ exhibited mixed quasi-cleavage/ductile fracture features (Figures. 4-11(h, i) and (k, l)). The brittle features were observed in the

central region of the specimens at 21 and 100 ℃. This implies that hydrogen charging promoted brittle-like fractures, irrespective of the deformation temperature.

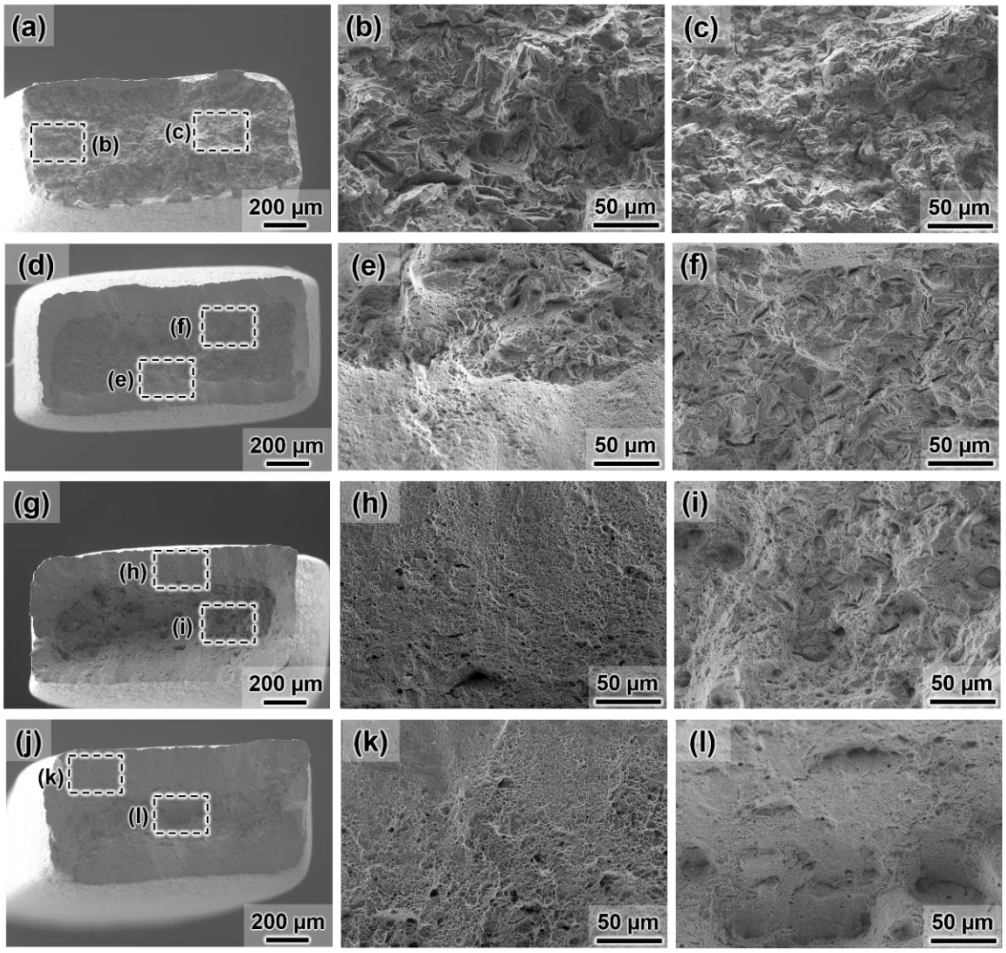

Figure. 4-10 SEM fractographs of hydrogen-uncharged specimens deformed at (a, b, c) -100, (d, e, f) -30, (g, h, i) 21, and (j, k, l) 100 ℃.

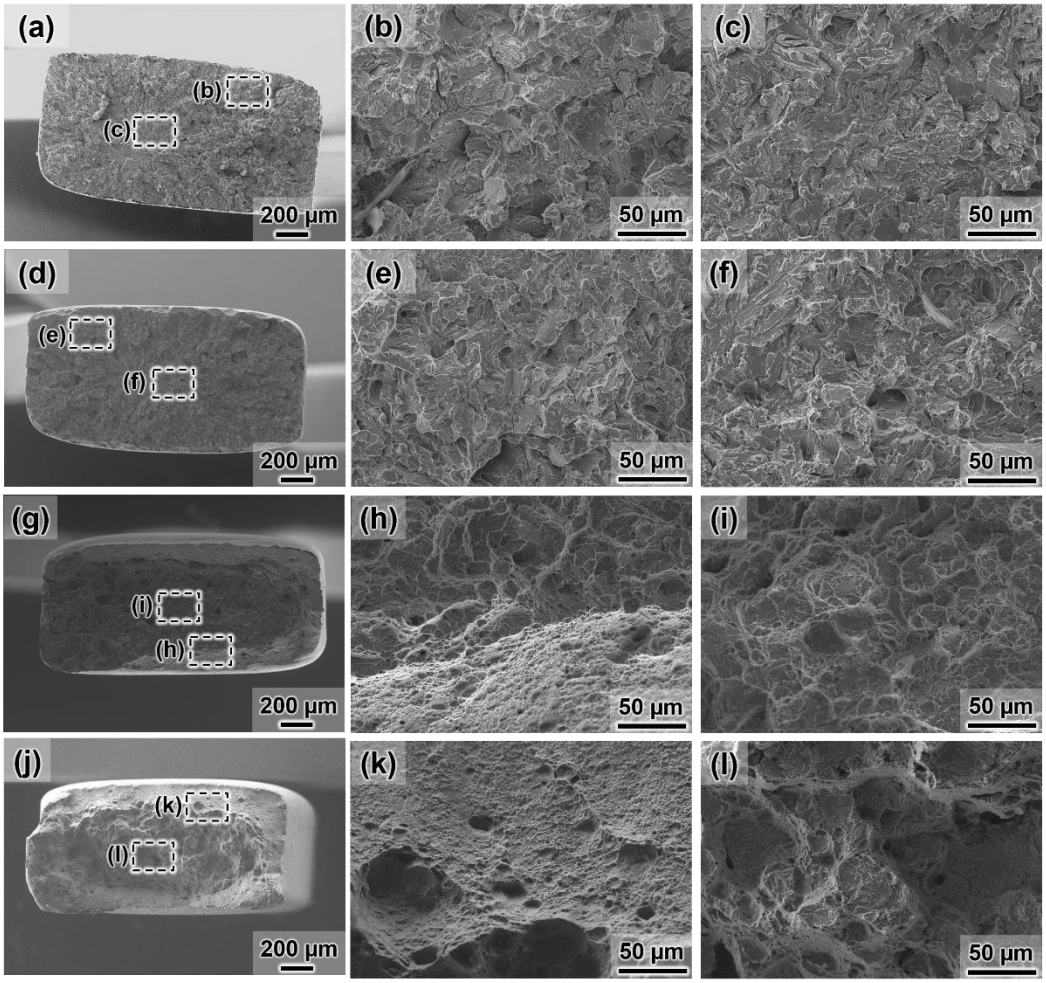

Figure. 4-11 SEM fractographs of hydrogen-charged specimens deformed at (a, b, c) -100, (d, e, f) -30, (g, h, i) 21, and (j, k, l) 100 ℃.

4.4 Discussion

4.4.1 Effect of deformation temperature on mechanical properties

Variation in tensile properties was closely related to the transformation behavior of the retained austenite and fracture mode. First, the variation in mechanical properties of hydrogen-uncharged specimens is noted. Detrimental factors for UEl are (1) flow stress, (2) critical stress for brittle cracking, and (3) work-hardening rate [16–19]. This implies that when true stress reaches critical stress for brittle cracking, premature fracture occurs, thus decreasing UEl. In addition, when true stress is the same as the work-hardening rate at the identical strain, necking occurs, which stops the uniform deformation of ductile materials. Therefore, low YS, high resistance to brittle cracking, and sustained high work hardening realize high uniform deformability. In the present steel, the influence of the test

temperature on the TRIP effect impacts these factors. Although YS in general steels increases with a decrease in the deformation temperature [20, 21], the variation trend changes when deformation-induced martensitic transformation dominates the yielding behavior. Specifically, as the driving force for martensitic transformation increases with a decrease in temperature, the critical stress for martensitic transformation, which corresponds to YS, decreases with a decrease in temperature. Figure. 4-5 shows the significant promotion of deformation-induced martensitic transformation owing to a decrease in temperature. Accordingly, YS decreased with a decrease in temperature (Figure. 4-3(a)). However, the promotion of martensitic transformation at low temperatures accelerates the TRIP effect, which increases work-hardening rates. The enhancement of work hardening adversely and positively affects mechanical properties at low temperatures. An increase in work-hardening rates increases UTS and delays the occurrence of necking but accelerates to reach the critical stress for brittle cracking. Therefore, UEl increased by decreasing temperature within the specified range where the fracture mode was ductile (Figures. 4-10(g) and (j)). On the other hand, UEl decreased when the deformation temperature decreased below -30 ℃ where brittle fracture occurred predominantly.

The UEl increased with increasing tensile testing temperature, but the UEl of the specimen tensile tested at 100 ℃ decreased. The low UEl deformed at 100 ℃ compared with that at 21 ℃ was because the effective work hardening was not possessed due to the suppression of transformation of retained austenite owing to the excessive increase in the stability of retained austenite.

4.4.2 Effect of deformation temperature on mechanical properties

The variation trend of the volume fraction of the retained austenite against deformation temperature in the hydrogen-charged specimens was similar to that in the hydrogen-uncharged specimens (Figure. 4-5 and Figure. 4-6). However, the fracture behavior of the hydrogen-charged specimens drastically changed when compared with that in the hydrogen-uncharged specimens (Figure. 4-10 and Figure. 4-11). The characteristic fracture behavior is associated with deformation-induced martensitic transformation, which is discussed in the next section. Other than the effect of the martensitic transformation, hydrogen plays a dual role regardingthe acceleration of brittle-like cracking. First, it increases the YS by solution hardening [21, 22]. Second, it decreases the critical stress, thus leading to brittle cracking [23, 24]. The increase in the YS or flow stress and decrease in the critical stress for brittle cracking accelerate to induce brittle premature fracture, which decreases elongation. Furthermore, in the present steel,

the serrated flow occurred at a tensile testing temperature of 100 ℃ owing to dynamic strain aging [25]. As the serrated flow involves deformation localization, *i.e.*, Portevin-Le Chatelier (PLC) banding, microscopic behavior can be varied particularly at a high temperature where dynamic strain aging occurs significantly. Specifically, when the work-hardening rate is high and the fracture mode is ductile, the deformation localization does not exhibit any detrimental effect on fracture. However, the difference between microscopic and macroscopic strains and the evolution of stress triaxiality in the PLC band can accelerate the occurrence of premature fracture when local plasticity plays an intrinsic role in microstructure cracking. The localized plasticity causes lattice defect accumulation, enhances dislocation-driven microscopic stress concentration, and increases macroscopic local stress caused by the evolution of stress triaxiality. These factors assist brittle-like cracking and subsequent fractures.

The significant contribution of stress triaxiality associated with PLC banding is evident in the fractographic feature (Figure. 4-11). The brittle fracture region was observed in the central region of the fracture surfaces at 21 and 100 ℃ where the serrated flow appeared. As brittle cracking preferentially occurred in the central region before the ductile fracture, there must be a relevant reason. When a classical ductile fracture mechanism is considered, fracture initiates from the central region of the specimen owing to necking and the associated evolution of stress triaxiality. As the fracture in the hydrogen-charged specimen deformed at 21℃ occurred before satisfying the Considère criterion, another factor that caused localized plastic deformation, which occurs during stable deformation, must be considered. A possible reason is that the PLC-banding-related localized plasticity caused significant necking and associated stress triaxiality evolution, which resulted in preferential brittle cracking in the central region of the specimen. Hence, the effect of PLC banding associated with dynamic strain aging is an additional factor that assists the quasi-cleavage fracture, which can explain the low fracture strength and ductility at 21 ℃. Furthermore, the PLC-banding can assist the fracture of the ductile stage, known as blue brittleness [26, 27]. Therefore, to understand the effect of temperature on the hydrogen embrittlement behavior of the TRIP-aided steel, the effects of martensitic transformation, solution hardening, and dynamic strain aging should be considered.

4.4.3 Microscopic plasticity evolution

The transformation ratio of the retained austenite (Figure. 4-7) and EBSD phase maps obtained after the fractures at -100 and -30 ℃ (Figure. 4-8) in the hydrogen-uncharged and hydrogen-charged specimens exhibited remarkable deformation-induced

martensitic transformation. Although the transformation ratios of the retained austenite of the hydrogen-charged specimens were slightly lower than that of the hydrogen-uncharged specimens, it arises from the difference in the UEl (volume fraction of the retained austenite was measured based on uniformly deformed portions of the fractured specimens). The deformation-induced transformation results in high-strength regions (martensite) that contain supersaturated hydrogen, causing quasi-cleavage and quasi-cleavage/ductile mixed modes at low temperatures. The hydrogen-charged specimens fractured at -100 and -30 ℃ did not exhibit any significant differences in the KAM and retained austenite fraction between the near-fracture-surface and uniformly deformed regions (Figures. 4-8(e, f) and 9(e, f)); however, the hydrogen-uncharged specimens exhibited differences (Figures. 4-8(a, b) and 9(a, b)). This fact indicates that the hydrogen-assisted failure occurred without macroscopic plasticity localization, *i.e.*, necking.

When the deformation temperature increased to 100 ℃, the transformation ratio of the specimens was lower than that of the specimens deformed at -100 and -30 ℃ (Figure. 4-8(h)). Furthermore, the KAM value of the retained austenite obtained at 100 ℃ with hydrogen charging was higher than those at other temperatures (Figure. 4-9(h)). These results indicate that the fracture occurred after the distinct plastic deformation of the retained austenite and necking at 100 ℃, which corresponds to the stress–strain response that indicated the fracture occurred after satisfying the Considère criterion (Figure. 4-2). In addition, a significant amount of the retained austenite remains near the fracture surface that underwent necking. These facts indicate that the suppression of the deformation-induced martensitic transformation is the key factor that allowed significant ductility at 100 ℃ in the hydrogen-charged specimen. The suppression of deformation-induced martensitic transformation at 100 ℃ positively affects hydrogen embrittlement resistance in two ways: (1) reduction in the number density of the hydrogen-related crack initiation site associated with deformation-induced martensitic transformation of retained austenite [28] and (2) decrease in flow stress, which resulted in relatively high UEl at 100 ℃ in the hydrogen-charged specimens.

4.5 Summary

SSRT tests of the hydrogen-charged and hydrogen-uncharged specimens of TBF steel was performed at a deformation temperature range of -100 to 100 ℃. The summaries are as follows:

（1） In the hydrogen-uncharged condition, the martensitic transformation was accelerated with a decrease in the deformation temperature, resulting in a decrease in the YS and an increase in the UTS owing to an increase in the work-hardening rates. The UEl

at 21 ℃ was the maximum and decreased with a decrease in the deformation temperature. The decrease in the UEl at low deformation temperature was attributed to the increase in workhardening rates, which accelerated to reach the critical stress for brittle cracking, implying the occurrence of brittle premature fracture before necking.

（2） The UEl decreased, and the brittle-like quasi-cleavage fracture occurred in the hydrogen-charged specimens deformed at low temperatures, although the transformation ratios were high at the low deformation temperature in the hydrogen-charged and hydrogen-uncharged specimens. These might be caused by the occurrence of transformed martensite that comprised supersaturated hydrogen and hydrogen-assisted failure without macroscopic plasticity localization, *i.e.*, necking.

（3） The significant decrease in the UEl of the hydrogen-charged specimen tensile tested at 100 ℃ was not possessed whereas the UEl decreased in the specimen tensile tested at 21 ℃ although mixed quasi-cleavage/ductile fracture features were obtained and serrated flow was exhibited in the stress-strain curves at both specimens at 21 and 100 ℃, which indicated dynamic strain aging occurred. The decrease in the UEl tensile tested at 21 ℃, might have been caused by the PLC-banding-related localized plasticity, which causes significant necking and associated stress triaxiality evolution. The excellent hydrogen embrittlement resistance of the hydrogen-charged specimen deformed at 100 ℃ might be attributed to the suppression of deformation-induced martensitic transformation, which reduces the number density of the hydrogen-related crack initiation site and decreases flow stress.

4.6 References

[1]. T. Hojo, K. I. Sugimoto, Y. Mukai, S. Ikeda, Effects of aluminum on delayed fracture properties of ultra high strength low alloy TRIP-aided steels, ISIJ Int. 48 (2008) 824–829.

[2]. A. Laureys, T. Depover, R. Petrov, K. Verbeken, Microstructural characterization of hydrogen induced cracking in TRIP-assisted steel by EBSD, Mater. Charact. 112 (2016) 169–179.

[3]. J. H. Ryu, Y. S. Chun, C. S. Lee, H. K. D. H. Bhadeshia, D.W. Suh, Effect of deformation on hydrogen trapping and effusion in TRIP-assisted steel, Acta Mater. 60 (2012) 4085–4092.

[4]. Z. D. Harris, S. K. Lawrence, D. L. Medlin, G. Guetard, J. T. Burns, B. P. Somerday, Elucidating the contribution of mobile hydrogen-deformation interactions to hydrogen-induced intergranular cracking in polycrystalline nickel, Acta Mater. 158 (2018) 180–192.

[5]. R. A. Oriani, The diffusion and trapping of hydrogen in steel, Acta Metall. 18 (1970) 147–157.

[6]. J. Mahieu, J. Maki, B. C. De Cooman, S. Claessens, Phase transformation and mechanical properties of Si-free CMnAl transformation-Induced plasticity-aided steel, Metall. Mater. Trans. A. 33 (2002) 2573–2580.

[7]. G. K. Tirumalasetty, M. A. Van Huis, C.M. Fang, Q. Xu, F.D. Tichelaar, D.N. Hanlon, J. Sietsma, H.W. Zandbergen, Characterization of NbC and (Nb, Ti) N nanoprecipitates in TRIP assisted multiphase steels, Acta Mater. 59 (2011) 7406–7415.

[8]. T. Yamashita, S. Morooka, S. Harjo, T. Kawasaki, N. Koga, O. Umezawa, Role of retained austenite in low alloy steel at low temperature monitored by neutron diffraction, Scr. Mater. 177 (2020) 6–10.

[9]. N. Tsuchida, S. Okura, T. Tanaka, Y. Toji, High-speed tensile deformation behavior of 1 GPa-grade TRIP-aided multi-phase steels, ISIJ Int. 58 (2018) 978–986.

[10]. T. Yamashita, N. Koga, O. Umezawa, Influence of deformability of retained austenite on martensitic transformation in tension for low alloy steel at low temperatures, ISIJ Int. 58 (2018) 1155–1161.

[11]. M. L. Martin, M. Dadfarnia, A. Nagao, S. Wang, P. Sofronis, Enumeration of the hydrogen-enhanced localized plasticity mechanism for hydrogen embrittlement in structural materials, Acta Mater. 165 (2019) 734–750.

[12]. J. H. Ryu, J. I. Kim, H. S. Kim, C. S. Oh, H. K. D. H. Bhadeshia, D. W. Suh, Austenite stability and heterogeneous deformation in fine-grained transformation-induced plasticity-assisted steel, Scr. Mater. 68 (2013) 933–936.

[13]. E. Abbasi, W. M. Rainforth, Microstructural evolution during bainite transformation in a vanadium microalloyed TRIP-assisted steel, Mater. Sci. Eng. A. 651 (2016) 822–830.

[14]. D. M. Field, D. C. Van Aken, Dynamic strain aging phenomena and tensile response of medium-Mn TRIP Steel, Metall. Mater. Trans. A. 49 (2018) 1152–1166.

[15]. A. A. Gorni, Steel forming and heat treatment handbook. 2019.

[16]. C. G. Sammis, M. F. Ashby, The failure of brittle porous solids under compressive stress states, Acta Metall. 34 (1986) 511–526.

[17]. M. Koyama, T. Sawaguchi, T. Lee, C.S. Lee, K. Tsuzaki, Work hardening associated with ε-martensitic transformation, deformation twinning and dynamic strain aging in Fe-17Mn-0.6C and Fe-17Mn-0.8C TWIP steels, Mater. Sci. Eng. A. 528 (2011) 7310–7316.

[18]. Y. J. Chao, S. Liu, B. J. Broviak, Brittle fracture: Variation of fracture toughness

with constraint and crack curving under mode I conditions, Exp. Mech. 41 (2001) 232–241.

[19]. A. Pineau, A. A. Benzerga, T. Pardoen, Failure of metals I: Brittle and ductile fracture, Acta Mater. 107 (2016) 424–483.

[20]. L. Mosecker, D. T. Pierce, A. Schwedt, M. Beighmohamadi, J. Mayer, W. Bleck, J. E. Wittig, Temperature effect on deformation mechanisms and mechanical properties of a high manganese C+N alloyed austenitic stainless steel, Mater. Sci. Eng. A. 642 (2015) 71–83.

[21]. M. Koyama, T. Kaneko, T. Sawaguchi, K. Tsuzaki, Microstructural damage evolution and arrest in binary Fe–high-Mn alloys with different deformation temperatures, Int. J. Fract. 213 (2018) 193–206.

[22]. C. Hao, M. Koyama, E. Akiyama, Quantitative Evaluation of Hydrogen Effects on Evolutions of Deformation-Induced ε-Martensite and Damage in a High-Mn Steel, Metall. Mater. Trans. A. 51 (2020) 6184–6194.

[23]. K. S. Kim, J. H. Kang, S. J. Kim, Carbon effect on hydrogen diffusivity and embrittlement in austenitic stainless steels, Corros. Sci. 180 (2021) 109226.

[24]. I. B. Tuğluca, M. Koyama, Y. Shimomura, B. Bal, D. Canadinc, E. Akiyama, K. Tsuzaki, Lowering strain rate simultaneously enhances carbon- and hydrogen-induced mechanical degradation in an Fe-33Mn-1.1C Steel, Metall. Mater. Trans. A. 50 (2019) 1137–1141.

[25]. I. C. Jung, B. C. De Cooman, Temperature dependence of the flow stress of Fe-18Mn-0.6C-xAl twinning-induced plasticity steel, Acta Mater. 61 (2013) 6724–6735.

[26]. B. J. Brindley, The effect of dynamic strain-ageing on the ductile fracture process in mild steel, Acta Metall. 18 (1970) 325–329.

[27]. M. Koyama, Y. Shimomura, A. Chiba, E. Akiyama, K. Tsuzaki, Room-temperature blue brittleness of Fe-Mn-C austenitic steels, Scr. Mater. 141 (2017) 20–23.

[28]. M. Koyama, C. C. Tasan, K. Tsuzaki, Overview of metastability and compositional complexity effects for hydrogen-resistant iron alloys: Inverse austenite stability effects, Eng. Fract. Mech. 214 (2019) 123–133.

Chapter 5: Temperature dependence of hydrogen-assisted damage evolution and fracture behavior in TRIP-aided bainitic ferrite steel

5 Temperature dependence of hydrogen-assisted damage evolution and fracture behavior in TRIP-aided bainitic ferrite steel

5.1 Introduction

For a further understanding of the synergistic effect of deformation temperature and hydrogen uptake, correlating microstructures with micro-damage evolution must be investigated. Specifically, once the deformation-induced transformation of retained austenite occurred, the hydrogen will be inherited from austenite to the deformation-induced martensite. Since the hydrogen solubility in austenite is higher than that in ferrite and martensite, the supersaturated hydrogen exists in martensite [1, 2]. Moreover, some studies also reported that crack initiation occurred at martensitic regions in dual phase steel and TRIP-aided steels [3–5]. Therefore, understanding the synergistic effects of hydrogen and deformation temperature on transformation-related micro-damage evolution and fracture behavior in TBF steels is key to realizing the reliable mechanical performance at various service temperatures.

In the present work, we aimed at detailed investigations on the temperature dependence of HE and fracture behaviors of the TBF steels. The correlation between microstructure and micro-damage during tensile deformation was also analyzed and discussed. Then, hydrogen-related cracks were studied with the correlative use of EBSD and ECCI analyses to reveal the relationship between the microstructure and crack propagation behavior.

5.2 Experimental procedure

The cold-rolled sheet was annealed at 900 ℃ for 1200 s followed by an austempering treatment at 400 ℃ for 1000 s, then oil-quenched to room temperature. The hydrogen charging preparation and tensile test has been reported as shown Chapter 2 and Chapter 4. The mechanical properties of hydrogen-uncharged and hydrogen-charged specimens were performed at deformation temperatures of -100, -30, 21, and 100 °C.

Micro-damage observations were performed using an EBSD and ECCI. The statistical analysis of crack length of hydrogen-uncharged and hydrogen-charged specimens was conducted by using Image J software, as shown in Figure. 5-1. the measured crack length was defined as the straight length of each crack (Figure. 5-3 (a1)). The number density of micro-damage was defined as that the number of micro-damages divided as the observed areas. Local strain (ε) was defined by following equation to reveal

the relationship between micro-damage and the local plastic strain in fractured region [6]:

$$\varepsilon = \ln \frac{t_0}{t} \tag{5-1}$$

where t_0 and t are the initial thickness before deformation and local thickness at the observed point, respectively.

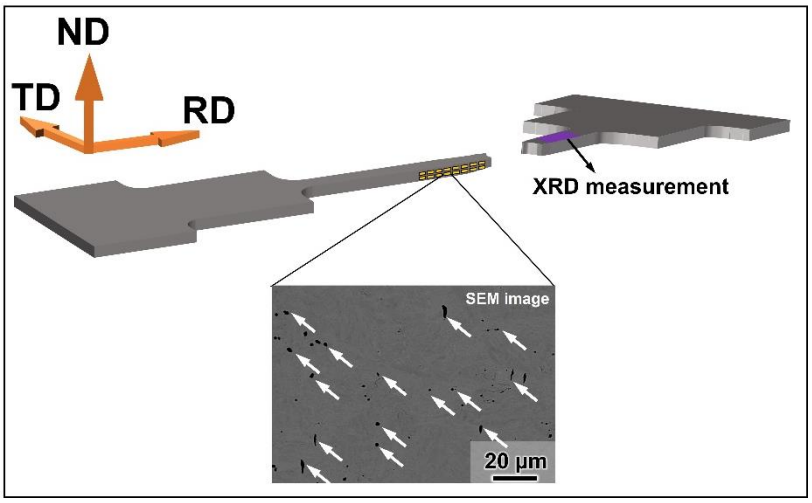

Figure. 5-1. A schematic diagram of the quantitative analysis of micro-damage evolution.

5.3 Results

5.3.1 Micro-damage evolution

Figure. 5-2 shows the transverse cross-sectional images of hydrogen-uncharged specimens. The hydrogen-uncharged specimen tested at -100 ℃ exhibited a relatively flat fracture surface in the macroscopic scale (Figure. 5-2(a)), while other specimens exhibited relatively large necking.

Figure. 5-3 shows the transverse cross-sectional image near fracture surface and micro-damages such as cracks and voids of the hydrogen-uncharged specimens at deformation temperatures of -100 and -30 ℃. Some sharp cracks were observed as shown in Figure. 5-3(a1), while the crack tip blunting occurred near the fractured surface of the specimen (Figure. 5-3(a2)). At the deformation temperature of -30 ℃, some cracks were located within bainitic ferrite matrix, and the formation of sharp cracks at the crack tip blunting were observed as indicated by the black arrow (Figure. 5-3 (b1)). In addition, the cracks exhibited the trend of small crack coalescence (Figure. 5-3 (b2)). Some nano-voids located between bainitic ferrite laths as marked by white arrows were observed.

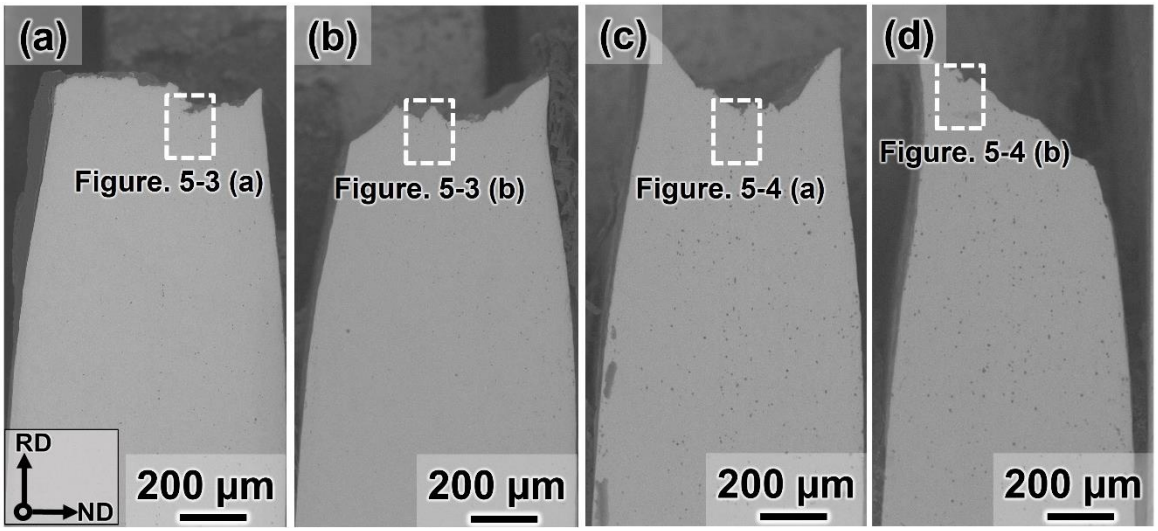

Figure. 5-2. SEM-BSE images of the fractured hydrogen-uncharged specimens at deformation temperatures of (a) -100, (b) -30, (c) 21, and (d) 100 ℃.

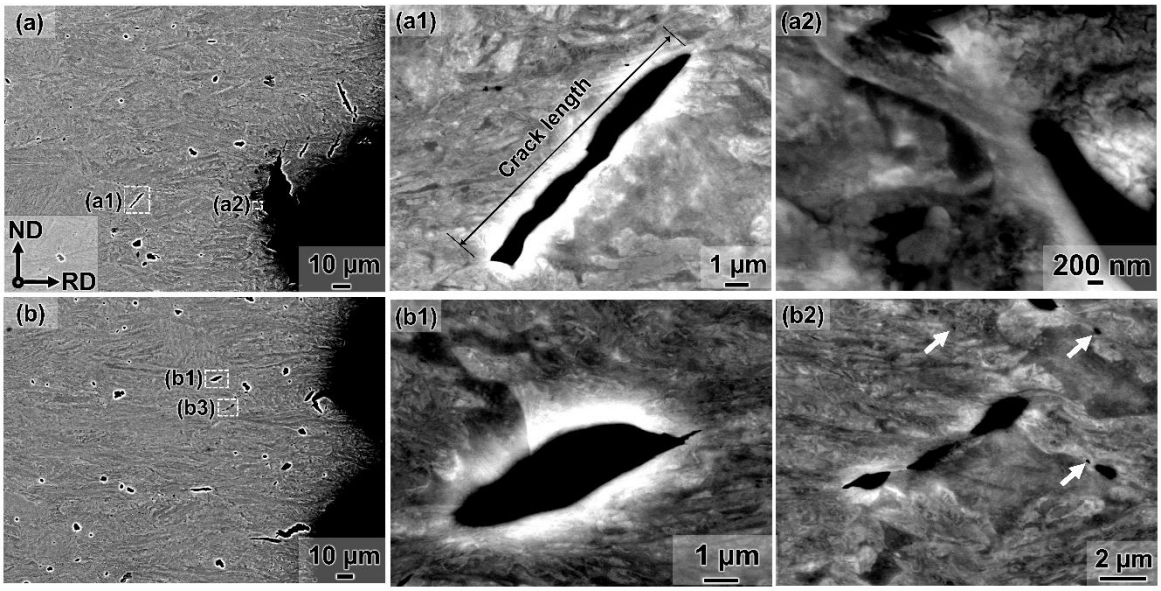

Figure. 5-3. ECC images of hydrogen-uncharged specimens at temperature of (a) -100, and (b) -30 ℃.

Figure. 5-4 shows the transverse cross-sectional image near fracture surface and micro-damages of the hydrogen-uncharged specimens at deformation temperatures of 21 and 100 ℃. The specimen tensile tested at 21 ℃ possessed an obvious necking. A series of voids were observed as marked by the black arrows (Figure. 5-4(a1)). Moreover, the voids were initiated the bainitic ferrite/deformation-induced martensite interface (Figure. 5-4(a2)). The specimen deformed at 100 ℃ presented the crack tip blunting (Figure. 5-4(b1)). The voids coalescence occurred at the bainitic ferrite/deformation-induced martensite interface and within bainitic ferrite, resulting in the micro-damage growth (Figure. 5-4(b2)).

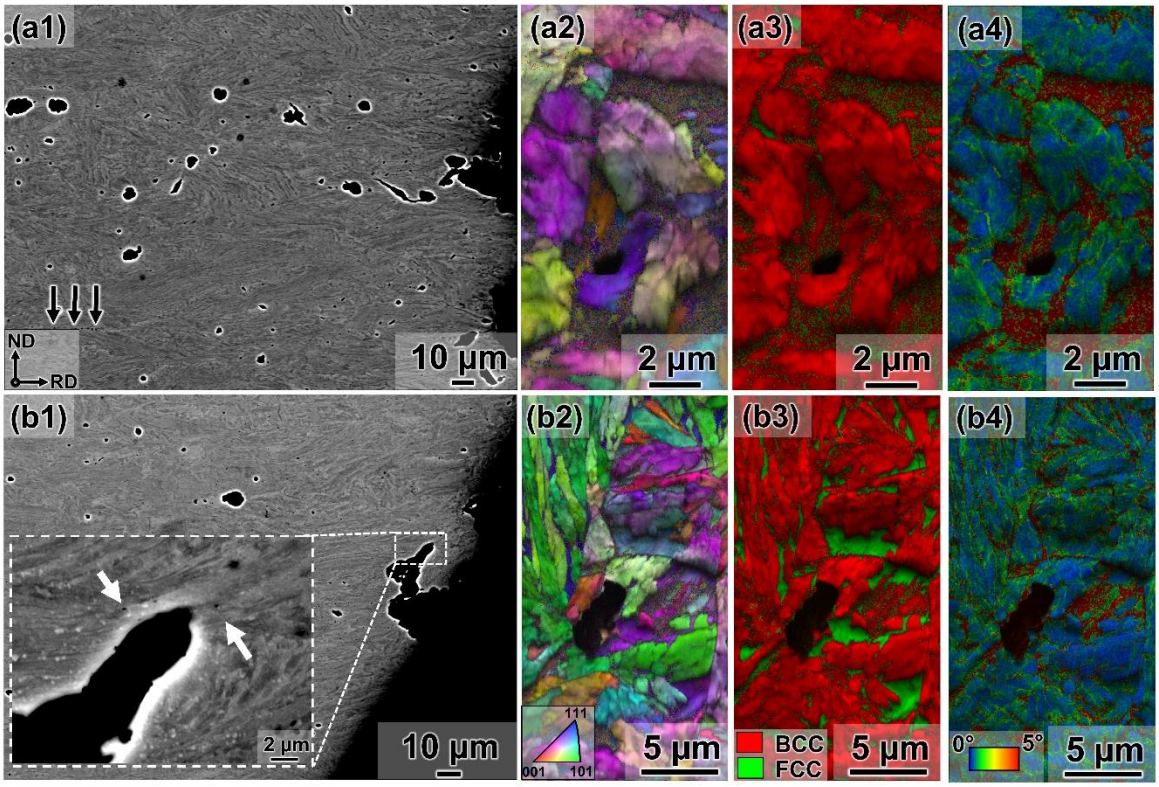

Figure. 5-4 ECC images and EBSD data of hydrogen-uncharged specimens at temperature of (a1-a4) 21, and (b1-b4) 100 ℃. (a1, b1) ECC images, (a2, b2) IPF with IQ, (a3, b3) phase image with IQ, and (a3, b3) KAM with IQ.

Figure. 5-5 shows the transverse cross-sectional surface near fracture region of the hydrogen-charged specimens tensile tested at different deformation temperatures. No obvious necking was observed in the hydrogen-charged specimens tested at -100 and -30 ℃, whereas the specimens tested at 21 and 100 ℃ possessed some necking. Moreover, considerable number of micro-damages were observed at the vicinity of the fracture surface of the hydrogen-charged specimens, as enlarged as white dashed rectangle in Figure. 5-5. The shape of crack in the hydrogen-charged specimens was appeared to be long and sharp compared with those in the hydrogen-uncharged specimens.

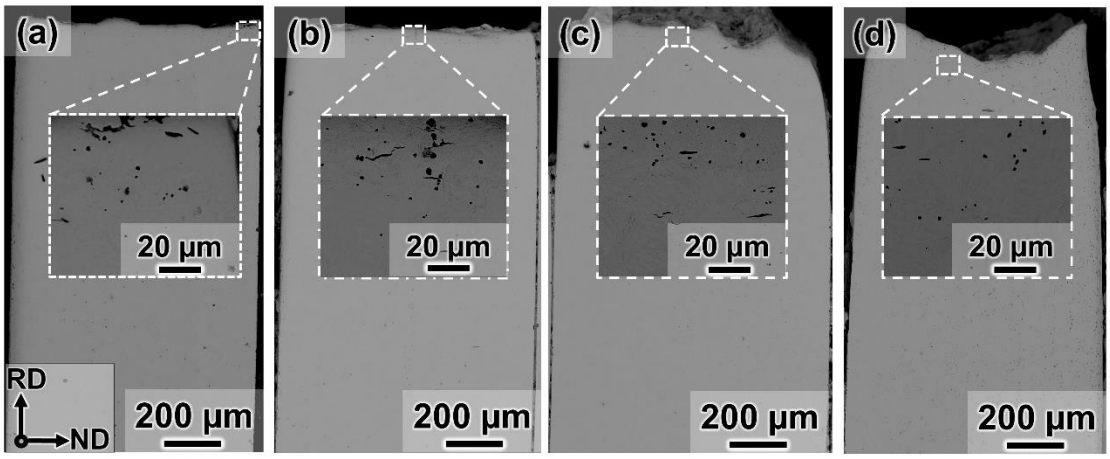

Figure. 5-5. SEM-BSE images of the fractured hydrogen-charged specimens at deformation temperatures of (a) -100, (b) -30, (c) 21, and (d) 100 ℃.

To obtain better understanding and conduct deep analysis of the temperature dependence on micro-damage evolution, number density of micro-damage and average crack length plotted against local strain are shown in Figure. 5-6. Hydrogen charging significantly increased the number density of micro-damage regardless of the deformation temperature. This result indicated that the introduction of hydrogen significantly increased the damage initiation probability. In addition, for all hydrogen-uncharged specimens, the average crack length slightly increased with the local strain, implying that the cracks were gradually evolved with the local strain (Figure. 5-6(c)). In contrast, the average crack length of hydrogen-charged specimens significantly increased with the local strain, especially the average crack length of hydrogen-charged specimens at deformation temperatures of -100 and -30 ℃ rapidly increased at a small strain range and then fracture occurred. Noted that the average crack length of hydrogen-charged specimen at deformation temperature of 100 ℃ did not exhibit a monotonic increase against local strain.

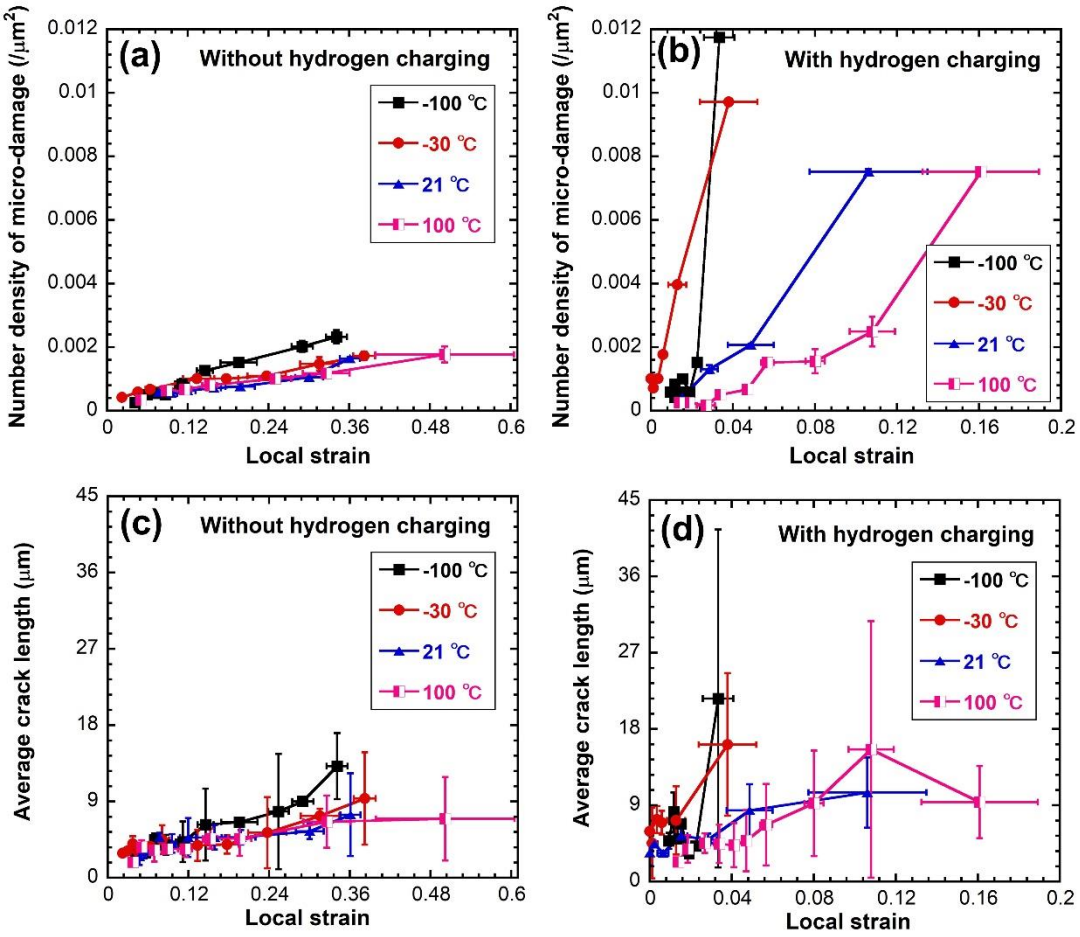

Figure. 5-6 (a, b) Number density of micro-damage and (c, d) average crack length plotted against local strain of the hydrogen-uncharged and hydrogen-charged specimens at different deformation temperatures. (a, c) without and (b, d) with hydrogen charging at various deformation temperatures.

Figure. 5-7 presents ECC images and EBSD maps of the cracks of hydrogen-charged specimen deformed at -100 ℃. The crack growth showed the zigzag path in the grain interior, and crack propagation was arrested at the prior austenite grain boundary as shown in Figure. 5-7(b). Deformation-induced martensite was observed as low IQ value region, which was easily formed the crack branching (Figure. 5-8(c)). In addition, the crack tip blunting occurred, which involved plastic strain evolution with high KAM value. The KAM value was obtained as the average misorientation angle between measurement point and the nearest neighbor points, which corresponds to geometrically necessary dislocation density [7]. And then crack tip blunting stopped crack growth (Figure. 5-8(e)). The crack tip blunting and sharp crack coalesced with each other as indicated the red arrow.

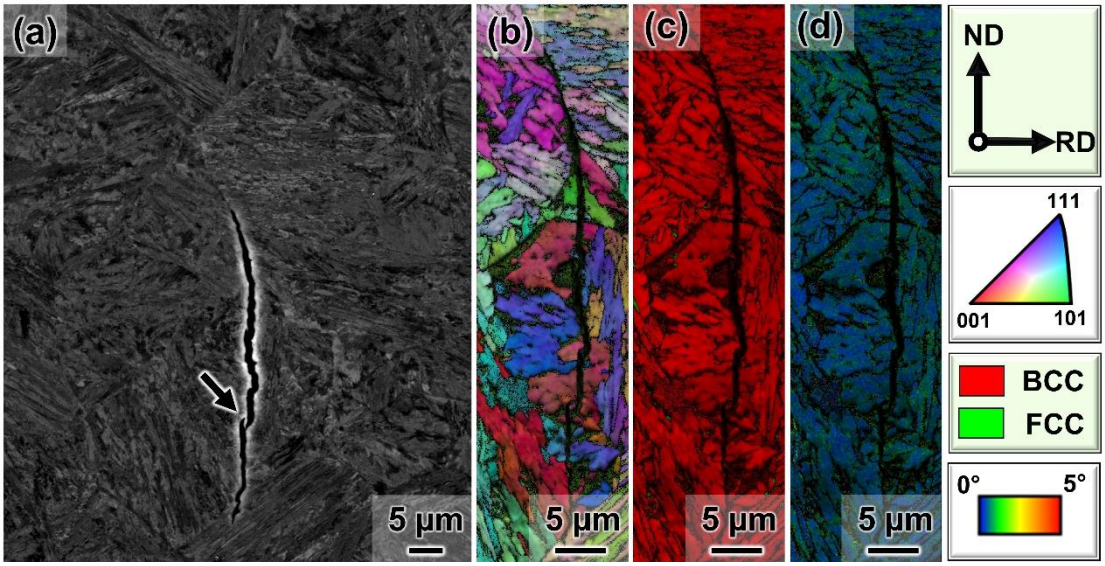

Figure. 5-7 ECC images and corresponding EBSD maps of cracks of hydrogen-charged specimens at deformation temperature of -100 ℃. (a) ECC image of crack, (b) IPF with IQ, (c) Phase with IQ, and (d) KAM with IQ.

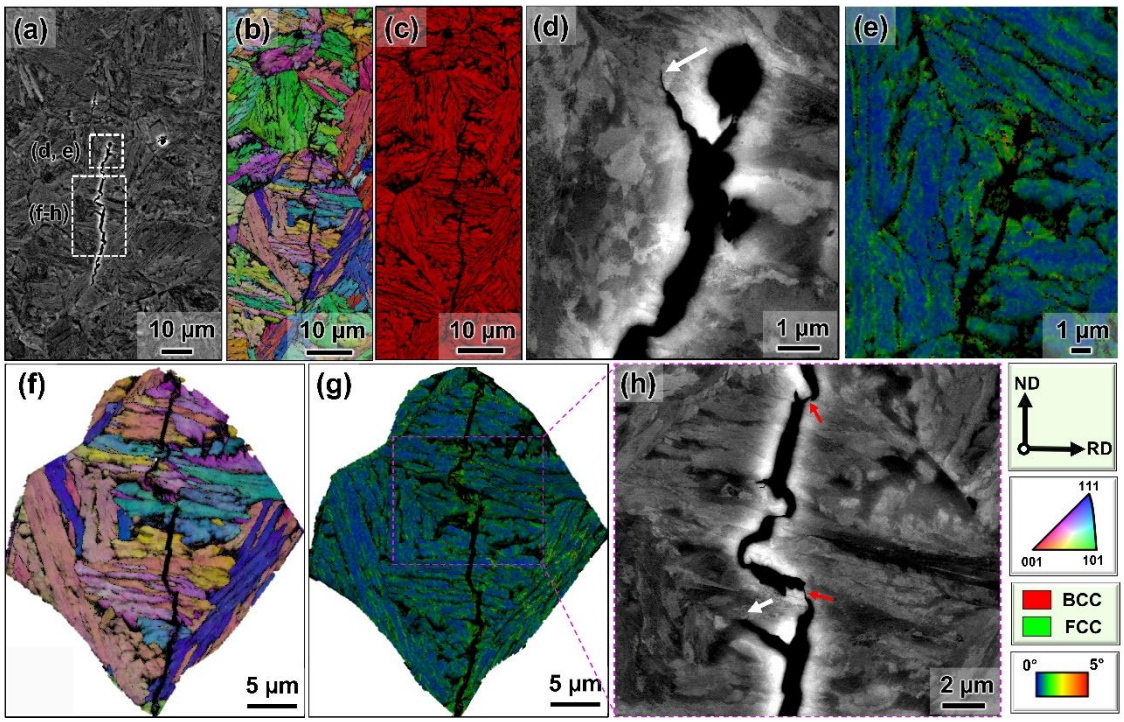

Figure. 5-8 ECC images and corresponding EBSD maps of cracks of hydrogen-charged specimens at deformation temperature of -100 ℃. (a, d, h) ECC images, (b, f) IPF with IQ, (c) phase with IQ, (e, g) KAM with IQ.

Figure. 5-9 shows ECC images and EBSD maps of the cracks of hydrogen-charged specimen deformed at -30 ℃. Some crack initiation sites were located at the prior austenite grain boundary, and both intergranular and transgranular crack propagations

occurred as shown in Figure. 5-9(b-d). In addition, the crack growth occurred along the bainitic ferrite packet/block, and then the crack blunting occurred (Figure. 5-9(f)). At the crack tip, the sharp crack and some voids were observed as indicated by the black arrow in Figure. 5-9(h).

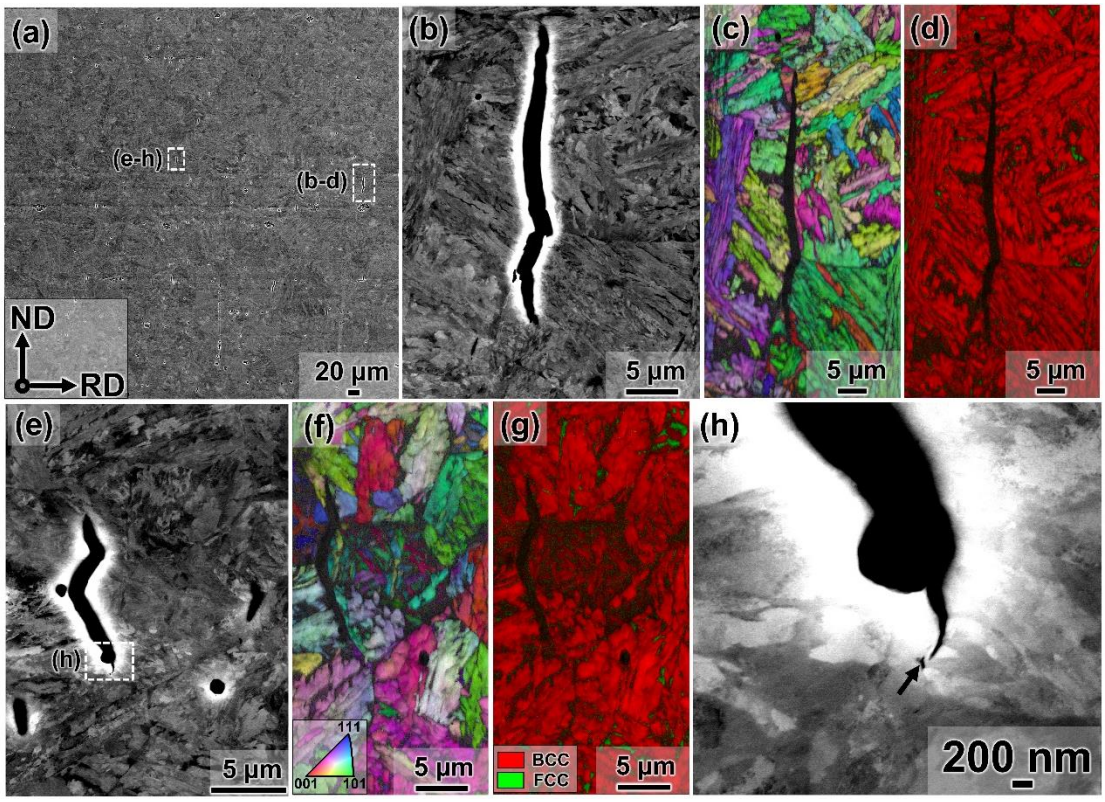

Figure. 5-9 ECC images and corresponding EBSD maps of cracks of hydrogen-charged specimens at deformation temperature of -30 ℃. (a) an overview of ECC image of crack, (b, e, h) magnified ECC images of the marked region in (a), (c, f) IPF with IQ, and (d, g) phase with IQ.

Figure. 5-10 shows ECC images and EBSD maps of the cracks of hydrogen-charged specimen deformed at 21 ℃. The crack initiation and propagation site were the vicinity of prior austenite grain boundary (Figure. 5-10(b-e)), and the crack branching was observed as shown in Figure. 5-10(b). In addition, the crack propagation across the bainitic ferrite packet/block boundaries tended to exhibit a deflection (Figure. 5-10(g)).

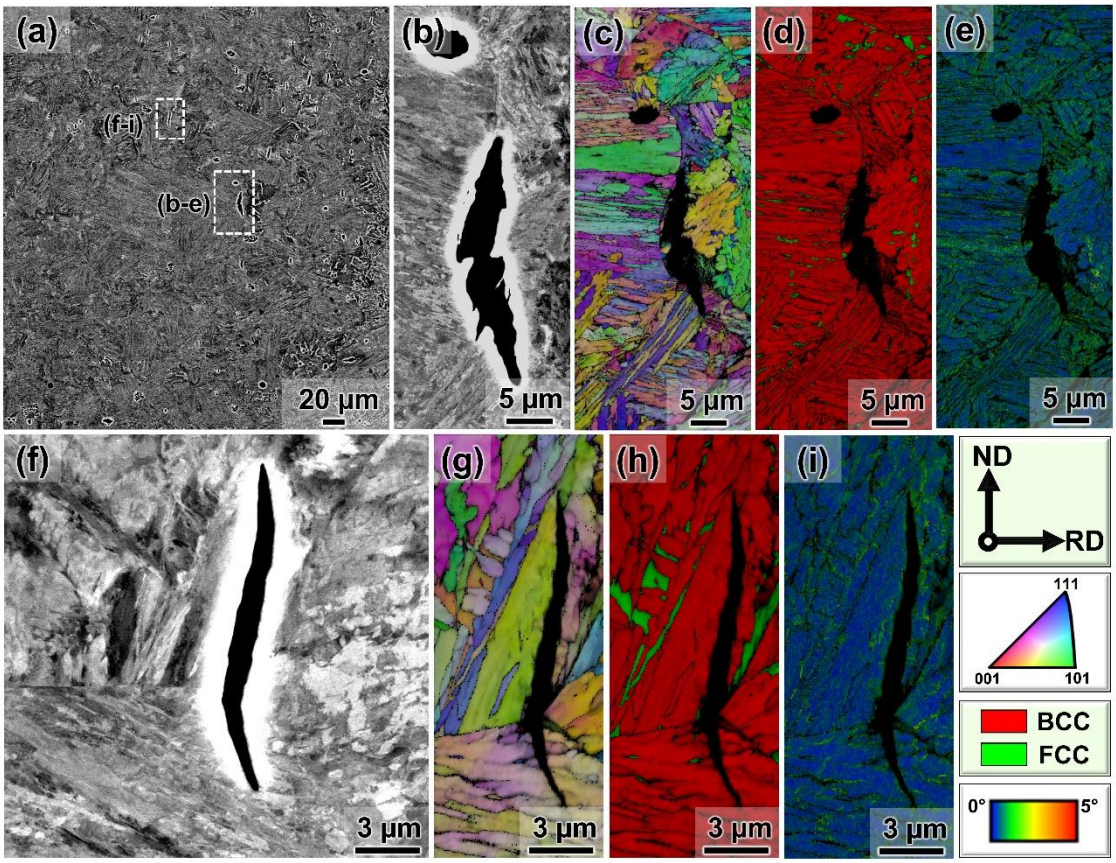

Figure. 5-10 ECC images and corresponding EBSD maps of cracks near the fractured regions of hydrogen-charged specimens at 21 ℃. (a) an overview of ECC image of crack, (b, f) magnified ECC images of the marked region in (a), (c, g) IPF with IQ, (d, h) phase with IQ, and (e, i) KAM with IQ.

Figure. 5-11 shows ECC images and EBSD maps of the cracks of hydrogen-charged specimen deformed at 100 ℃. The transgranular crack growth was observed, and some micro-scale cracks propagated by interconnection of smaller cracks to form stepped crack as shown in Figure. 5-11(b-e). Moreover, the micro-scale cracks formed and coalesced ahead of the blunt crack tip, which showed high KAM value surrounding the cracks (Figure. 5-11(i)), In addition, some voids ahead of the crack were observed as shown in Figure. 5-11(f).

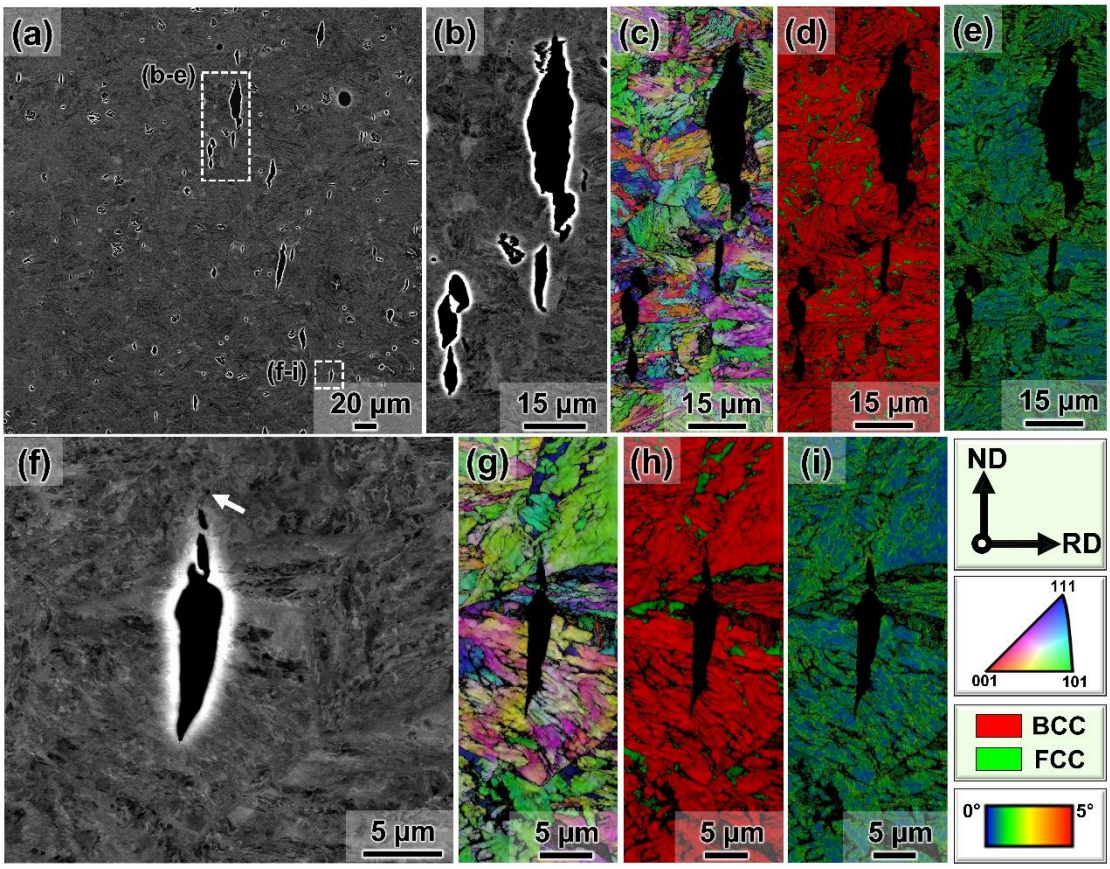

Figure. 5-11 ECC images and corresponding EBSD maps of cracks near the fractured regions of hydrogen-charged specimens at 100 ℃. (a) an overview of ECC image of crack, (b, f) magnified ECC images of the marked region in (a), (c, g) IPF with IQ, (d, h) phase with IQ, and (e, i) KAM with IQ.

5.4 Discussion

5.4.1 Micro-damage initiation mechanism

As mentioned above, the micro-damage initiation was frequently observed at grain boundaries and phase interfaces regardless of whether hydrogen was introduced, similarly to dual phase steel [8, 9] and medium Mn steel [10, 11]. In the hydrogen-uncharged specimen at -100 and -30 ℃, almost retained austenite transformed into deformation-induced martensite, and the microscopic plasticity localization occurred in the previous study [12], which resulted in the obvious strain partitioning among bainitic ferrite and retained austenite / deformation-induced martensite during deformation. In this regard, retained austenite transformed into hard deformation-induced martensite prior to a significant plasticity evolution in bainitic ferrite. Therefore, martensite-related microstructures acted as micro-damage initiation site for the brittle-like fracture. However, some retained austenite remained with increasing the deformation temperature due to the

high stability of retained austenite. Moreover, deformation-induced martensite was ductile for the specimens at 21 and 100 ℃ in the absence of hydrogen, micro-damage tip blunting occurred via plastic deformation of the deformation-induced martensite and the bainitic ferrite despite micro-damage initiation. The micro-damage size (*e*. *g*. average crack length) exhibited no obvious variation at local strain of below 0.2. Therefore, it can be concluded that the micro-damage initiation in the hydrogen-uncharged specimens at 21 and 100 ℃ did not play a critical role in the fracture, which resulted in necking and ductile fracture as the predominant mode.

In contrast, the introduction of hydrogen increased the number density of micro-damage (Figure.8(b)), indicated that hydrogen increased the driving force and probability of micro-damage initiations. The possible factors for the micro-damage initiation of hydrogen-charged specimens are as follows: (1) the decrease of grain boundary strengths in the presence of hydrogen, and (2) the different hydrogen diffusivity and solubility in deformation-induced martensite and retained austenite. With regard to first factor, grain boundaries are preferential sites for hydrogen accumulation and the segregated impurities such as S and P, resulting in the reduction of grain boundaries via the HEDE mechanism [52, 53]. Although it was not directly confirmed that hydrogen decreased the cohesive energy of grain boundaries, the intergranular micro-damage at the prior austenite grain boundaries were formed. Moreover, as described above, the cracks in the hydrogen-charged specimens were sharp compared to those of the hydrogen-uncharged specimens, indicating that hydrogen weakens the strength of microstructural boundaries, *e.g*, packet, block boundaries. Regarding the second factor, the deformation-induced martensite was supersaturated with hydrogen, which originated from the retained austenite with higher hydrogen solubility [13, 14]. Since the hydrogen diffusivity of martensite was higher than that of austenite, the enriched hydrogen in deformation-induced martensite diffused to surrounding retained austenite or bainitic ferrite. In other words, hydrogen was first concentrated in retained austenite, then, deformation-induced martensitic transformation occurred, which caused the micro-damage initiation due to the supersaturated hydrogen concentration. In addition, although hydrogen diffusion was low at cryogenic temperature, the deformation-induced martensitic transformation introduced the stresses in the vicinity of bainitic ferrite and retained austenite or martensite owing to the volume expansion of phase transformation [15], which caused the stress or strain-driven hydrogen accumulation in this region. Hence, the occurrence of micro-damage at the bainitic ferrite/deformation-induced martensite interface can be significantly promoted in the presence of hydrogen. However, some retained austenite remained at the deformation temperatures of 21 and 100 ℃, which reduced the preferential initiation sites of micro-

damage, resulting in decrease the number density of micro-damage (Figure. 5-6(b)). In summary, the micro-damage initiation probability was closely related to the promotion of deformation-induced martensitic transformation.

5.4.2 Micro-damage growth and fracture behavior

In addition to the previous discussion about the micro-damage initiation, the micro-damage growth without and with hydrogen charging should be considered to explain the temperature dependence of the micro-damage and failure behavior. For the hydrogen-uncharged specimen at -100 and -30 ℃, the micro-damage arrestability of bainitic ferrite in the cryogenic temperature was significantly deteriorated, because screw dislocation mobility controlled by thermal activation process is markedly decreased in bainitic ferrite. In other words, the plastic deformability of bainitic ferrite dominated the micro-damage arrestability. When bainitic ferrite arrestability gets low in the cryogenic temperature, the average crack length increased with the local strain (Figure. 5-6(c)). The micro-damage growth occurred via the repetition of nano-crack/void formation at the crack tip and subsequent coalescence (Figure. 5-3). Meanwhile, some sharp cracks developing perpendicular to the tensile direction were observed, because the stress around the crack tip increased with further deformation owing to work hardening and hindered the crack blunting. More specifically, when the local stress at the crack tip reaches the critical stress for the quasi-cleavage cracking, a newly nucleated crack starts to propagate into the bainitic ferrite grain by quasi-cleavage fracture. However, the crack arrestability in baintic ferrite is significant with increasing the deformation temperature of 21 and 100 ℃, and the crack tip blunting decreased local stress, which can reduction of the driving force for further micro-damage growth (Figure. 5-4). The micro-damage arrest occurred as long as the plasticity of bainitic ferrite was sufficient even when the flow stress increased with the decrease in the deformation temperature from 100 to 21℃. The crack tip blunting suppressed the micro-damage growth, which corresponded to the dimples without a fisheye.

The presence of hydrogen not only induced the micro-damage initiations, but also promoted the micro-damage growth. Figure. 5-12 shows the schematic of mode for micro-damage formation in hydrogen-charging condition. For the cryogenic temperature condition, since the diffusion and transportation of hydrogen were extremely difficult at low deformation temperature, it can be inferred that it was difficult for hydrogen to interact with dislocations, to diffuse and to be trapped at other hydrogen trapping sites during deformation. Hence, the hydrogen segregation at the grain boundaries may assist with micro-damage coalescence via hydrogen-enhanced decohesion. Once a crack

initiated, it grew further rather than occurring the crack arrest and crack tip blunting (Figure. 5-6(d)). In addition, the sharp crack tip opens and blunts via locally large plastic deformation (Figure. 5-8), which induced a drastic deformation-induced martensitic transformation. The martensitic transformation at the crack tip triggers further cracking, which also diminishes the crack growth resistance. However, for the hydrogen-charged specimen at 21 ℃, micro-damage growth was attributed to the coupled hydrogen diffusion and the increase in hydrogen concentration ahead of a crack tip due to hydrogen transportation via dislocation movement [16]. Under tensile loading conditions, a stress field with a hydrostatic component is developed in front of a crack tip and thus the enrichment of hydrogen at a critical site ahead of the crack tip is promoted by stress-driven hydrogen diffusion [17, 18]. Moreover, since the diffusion coefficient of hydrogen in martensite is much higher than that in retained austenite, the deformation-induced martensite provides a path for hydrogen transportation during deformation and a large amount of hydrogen diffuses toward the retained austenite/martensite interface. Therefore, hydrogen localization near the crack tip can assist the formation of cracks/voids near the crack tip and associated crack propagation. On the other hand, for the hydrogen-charged specimen at 100 ℃, the hydrogen diffusivity is high enough compared with the velocity dislocation movement, and then, the hydrogen detrapping from dislocations often occurred during deformation, hydrogen diffusion flux along prior austenite grain boundaries by dislocation movement is small [19], resulted in the formation of transgranular crack rather than intergranular crack. Therefore, the hydrogen-charged specimen at 100 ℃ shown relatively high elongation compared with the hydrogen-charged specimen at 21 ℃. In addition, the decrease of the deformation-induced martensite of retained austenite reduced the micro-damage initiation probability, and then further decreased the driving force of micro-damage growth based on the stress accommodation.

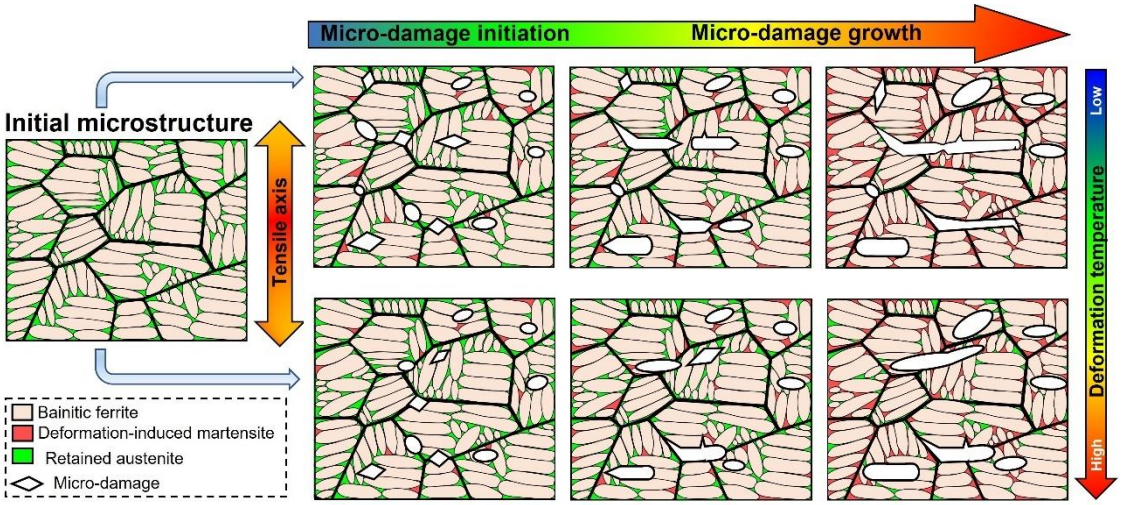

Figure. 5-12 Schematic illustrations of micro-damage initiation and propagation processes under hydrogen charging.

5.5 Summary

Hydrogen-charged and uncharged specimens of TBF steel were carried out at deformation temperature ranging from -100 ℃ to 100 ℃ to investigate the co-effect of hydrogen and deformation temperature on the damage evolution and fracture behavior. The summaries are as follows:

（1） The average crack length of hydrogen-uncharged specimens slightly increased with the local strain, and a decrease in deformation temperature from 100 to -100 ℃ increased the average crack length due to the increase flow stress and deterioration of bainitic ferrite arrestability,

（2） The introduction of hydrogen increased the number density of micro-damage and deteriorated the resistance to the hydrogen-induced cracks initiation and deteriorated micro-damage arrestability, which decreased elongation. The probability of micro-damage initiations was sensitive to deformation temperature, which was closely related to the promotion of deformation-induced martensitic transformation. Hydrogen significantly promoted the crack propagation at lower local strain, which resulted in significant increase the average crack length.

5.6 References

[1]. M. Koyama, H. Springer, S. V. Merzlikin, K. Tsuzaki, E. Akiyama, D. Raabe, Hydrogen embrittlement associated with strain localization in a precipitation-hardened Fe-Mn-Al-C light weight austenitic steel, Int. J. Hydrogen Energy. 39 (2014) 4634–4646.

[2]. M. Koyama, C. C, E. Akiyama, K. Tsuzaki, Hydrogen-assisted decohesion and localized plasticity in dual-phase steel, Acta Mater. 70 (2014) 174–187.

[3]. E. Hornbogex, Martensitic transformation at a propagating crack, Acta Metall. 26 (1977) 147–152.

[4]. G. Lacroix, T. Pardoen, P.J. Jacques, The fracture toughness of TRIP-assisted multiphase steels, Acta Mater. 56 (2008) 3900–3913.

[5]. K. Sugimoto, M. Kobayashi, S. Hashimoto, Ductility and strain-induced transformation in a high-strength transformation-induced plasticity-aided dual-phase steel, Metall. Trans. A. 23 (1992) 3085–3091.

[6]. C. Hao, M. Koyama, E. Akiyama, Quantitative evaluation of hydrogen effects on evolutions of deformation-induced ε-martensite and damage in a high-Mn Steel, Metall. Mater. Trans. A. 51 (2020) 6184–6194.

[7]. R. Kakimoto, M. Koyama, K. Tsuzaki, EBSD- and ECCI-based assessments of inhomogeneous plastic strain evolution coupled with digital image correlation, ISIJ Int. 59 (2019) 2334–2342.

[8]. M. Calcagnotto, Y. Adachi, D. Ponge, D. Raabe, Deformation and fracture mechanisms in fine- and ultrafine-grained ferrite / martensite dual-phase steels and the effect of aging, Acta Mater. 59 (2011) 658–670.

[9]. M. Koyama, C. C. Tasan, E. Akiyama, K. Tsuzaki, D. Raabe, Hydrogen-assisted decohesion and localized plasticity in dual-phase steel, Acta Mater. 70 (2014) 174–187.

[10]. Y. Zhou, M. Koyama, T. Hojo, S. Ajito, E. Akiyama, Transformation-induced microcracks and their arrest with different deformation temperatures in a medium Mn steel, Metall. Mater. Trans. A. 54(2023), 153–166.

[11]. H. Choi, S. Lee, J. Lee, F. Barlat, B. C. D. Cooman, Characterization of fracture in medium Mn steel, Mater. Sci. Eng. A. 687 (2017) 200–210.

[12]. Y. Zhou, T. Hojo, M. Koyama, S, Ajito, E. Akiyama, Synergistic effects of hydrogen and deformation temperature on mechanical properties of TRIP-aided bainitic ferrite steel, Mater. Sci. Eng. A. 819 (2022) 143070.

[13]. R. A. Oriani, P.H. Josephic, Equilibrium aspects of hydrogen-induced cracking of

steels, Acta Metall. 22 (1974) 1065–1074.

[14]. C. D. Beachem, A new model for hydrogen-assisted cracking (hydrogen “embrittlement”), Metall. Trans. 3 (1972) 441–455.

[15]. G. B. Olson, M. Azrin, Transformation behavior of TRIP steels, Metall. Trans. A. 9 (1978) 713–721.

[16]. M. Koyama, E. Akiyama, K. Tsuzaki, D. Raabe, Hydrogen-assisted failure in a twinning-induced plasticity steel studied under in situ hydrogen charging by electron channeling contrast imaging, Acta Mater. 61 (2013) 4607–4618.

[17]. H. K. Birnbaum, P. Sofronis, Hydrogen-enhanced localized plasticity-a mechanism for hydrogen-related fracture, Mater. Sci. Eng. A. 176 (1994) 191–202.

[18]. M. L. Martin, M. Dadfarnia, A. Nagao, S. Wang, P. Sofronis, Enumeration of the hydrogen-enhanced localized plasticity mechanism for hydrogen embrittlement in structural materials, Acta Mater. 165 (2019) 734–750.

[19]. M. Koyama, D. Yamasaki, T. Nagashima, C. C. Tasan, K. Tsuzaki, In situ observations of silver-decoration evolution under hydrogen permeation: Effects of grain boundary misorientation on hydrogen flux in pure iron, Scr. Mater. 129 (2017) 48–51.

Chapter 6: Conclusions

6 Conclusions

The objective of the thesis focuses on the microstructure evolution and hydrogen embrittlement behavior in TBF steels. The austempering time effects on the mechanical properties and fracture behavior were investigated. Additionally, the synergistic effects of deformation temperature and hydrogen on the mechanical properties and the detailed deformation and micro-damage evolution were addressed. The main conclusions are as follows:

(1) The microstructure of the TBF steels consisted of bainitic ferrite/ bainite, retained austenite, and martensite. When the austempering time increased from 0 to 1000 s, the volume fraction of retained austenite increased from 2.1 to around 12%, followed by a decrease to 4.8% at an austempering time of 3600 s, which indicated austempering time optimization for maximizing volume fraction of retained austenite.

(2) The UEl and TEl of TBF steels were remarkably dependent on the austempering time; UEl increased from 0.5% to 19.8% and subsequently decreased to 9.7% whereas TEl increased from 3.6% to 23.5% and subsequently decreased to 11.9%. The TBF steel austempered for 1000 s showed excellent mechanical properties with a YS of 960 MPa, UTS of 1182 MPa, and TEl of 23.5%. The excellent strength-elongation balance of the TBF steel austempered for 1000 s was attributed to the effective deformation induced transformation in a large fraction of the metastable retained austenite, which effectively suppressed crack and void initiation, propagation, and growth.

(3) In the hydrogen-uncharged condition, the martensitic transformation was accelerated with a decrease in the deformation temperature, resulting in a decrease in the YS and an increase in the UTS owing to an increase in the work-hardening rates. The UEl at 21 ℃ was the maximum and decreased with a decrease in the deformation temperature. The decrease in the UEl at low deformation temperature was attributed to the increase in work hardening rates, which accelerated to reach the critical stress for brittle cracking, implying the occurrence of brittle premature fracture before necking.

(4) The UEl decreased, and the brittle-like quasi-cleavage fracture occurred in the hydrogen-charged specimens deformed at low temperatures, although the transformation ratios were high at the low deformation temperature in the hydrogen-charged and hydrogen-uncharged specimens. These might be caused by the occurrence of transformed martensite that comprised supersaturated hydrogen and hydrogen-assisted failure without macroscopic plasticity localization, *i.e.*, necking.

(5) With an increase in the deformation temperature from - 100 to 100 ℃, fractographic features of hydrogen-charged specimens changed from the quasi-cleavage

to quasi-cleavage/ductile mode, which attributed to deformation-induced martensitic transformation occurred and hydrogen played dual roles in accelerating brittle-like cracking.

(6) The average crack length of hydrogen-uncharged specimens slightly increased with the local strain, and a decrease in deformation temperature from 100 to -100 ℃ increased the average crack length due to the increase flow stress and deterioration of bainitic ferrite arrestability, which is accompanied by a change in the fracture mode from ductile fractures to the mixture of brittle-like and ductile features and quasi-cleavage failure.

(7) Hydrogen charging increased the probability of micro-damage initiation and deteriorated micro-damage arrestability, which decreased elongation. Meanwhile, the introduction of hydrogen increased the number density of micro-damage and deteriorated the resistance to the hydrogen-induced cracks initiation and deteriorated micro-damage arrestability, which decreased elongation.

(8) When hydrogen was introduced, the transformation-related brittle cracking was promoted. The cracking path was block boundaries with retained austenite films. Therefore, size reduction of block and retained austenite film, and control of block alignment are key to design hydrogen-resistant TBF steel.

Acknowledgment

As Chinese saying goes, starlight asks not those who trudgen on their ways, and time fails not those who travail nights and days. The doctoral study trip to Tohoku University has brought me too much harvest and happiness, which will always remain in my heart. I would like to thank everyone who I met during my Ph.D. study.

Firstly, I would like to thank my supervisor Akiyama sensei for all his guidance, support, and encouragement. He provided me with good scientific research equipment and a relaxed and free atmosphere, enabling me to devote myself to research and obtain some research achievement during my Ph.D. study. Moreover, I have learned several great qualities from him, and these qualities make me not only a better researcher, but also a better person in the future.

I also want to sincerely thank Hojo sensei, Koyama sensei and Ajito sensei. They patiently taught me how to do scientific research and experiments. This study would not have been possible without their constant guidance. Their mentoring, knowledge, and encouragement have been especially valuable. Particularly, Koyama sensei gives me quite valuable suggestions during the process of my Ph.D. study. He inspired me to pursue original research, and his kind help on both research and communication made me more interested in the research field of hydrogen embrittlement. I benefited greatly from every fruitful discussion and his rich knowledge in material science and solid mechanics.

I would like to express my gratitude to every member of Akiyama lab for being very kind to me. Specifically, I wish to thank Mapp san for helping and supporting me during these years. I also sincerely wish her a happy life in the United States. I am sincerely grateful to the group members, including Shibayama san, Nishimura san, Kobayashi san, Guo san, Wen san, and Zhang san, for making my life enjoyable. I would like to express my appreciation for the fruitful discussions on different topics to Rama san, Kong san, and Chen san. In addition, I am thankful for all the help from my friends.

I would like to thank the thesis committee members such as Watanabe sensei, Matsuyama sensei, for your invaluable time and helpful suggestions on my thesis.

Last but not least, I wish to express my love and the warmest thanks to my family members. In particular, I would like to thank my parents for their support at all stages of my studies. I am also grateful to China Scholarship Council (CSC) for financial support during my doctoral study.

List of abbreviations

AHSSs	advance high-strength steels
AIDE	adsorption-induced dislocation emission
BCC	body-centered cubic
BF	bainitic ferrite
BS	band slope
DP	dual-phase
EBSD	electron backscattered diffraction
ECCI	electron channelling contrast imaging
FCC	face centered cubic
HE	hydrogen embrittlement
HEDE	hydrogen-enhanced decohesion
HELP	hydrogen-enhanced localized plasticity
HESIV	hydrogen-enhanced strain-induced vacancies
IPF	inverse pole figure
IQ	image quality
KAM	kernel average misorientation
M/A	martensite/austenite
MMS	medium Mn steel
ND	normal direction
PLC	Portevin-Le Chatelier
Q&P	quenching and partitioning
RA	retained austenite
RD	rolling direction
SEM	scanning electron microscopy
SSRT	slow strain rate tensile
TBF	TRIP-aided bainitic ferrite
TD	transverse direction
TDS	thermal desorption spectrometry
TEl	total elongation
TRIP	transformation-induced plasticity
TWIP	twinning-induced plasticity
UEl	uniform elongation
UTS	ultimate tensile strength
XRD	X-ray diffraction
YS	yield strength

Publications

1. Yutao Zhou, Tomohiko Hojo, Amane Kitahara, Yusuke Onuki, Shigeo Sato, Motomichi Koyama, and Eiji Akiyama, Austenite stabilization kinetics in early stages of austempering treatment in TRIP-aided steel using in-situ neutron diffraction technique, Materialia 21(2022), 101317 (Peer-reviewed)
2. Yutao Zhou, Tomohiko Hojo, Motomichi Koyama, Saya Ajito, and Eiji Akiyama, Synergistic effects of hydrogen and deformation temperature on mechanical properties of TRIP-aided bainitic ferrite steel, Materials Science and Engineering A 842(2022), 143070 (Peer-reviewed)
3. Yutao Zhou, Tomohiko Hojo, Motomichi Koyama, and Eiji Akiyama, Effect of austempering treatment on the microstructure and mechanical properties of 0.4C–1.5Si-1.5Mn TRIP-aided bainitic ferrite steel, Materials Science and Engineering A 819(2021), 141479 (Peer-reviewed)